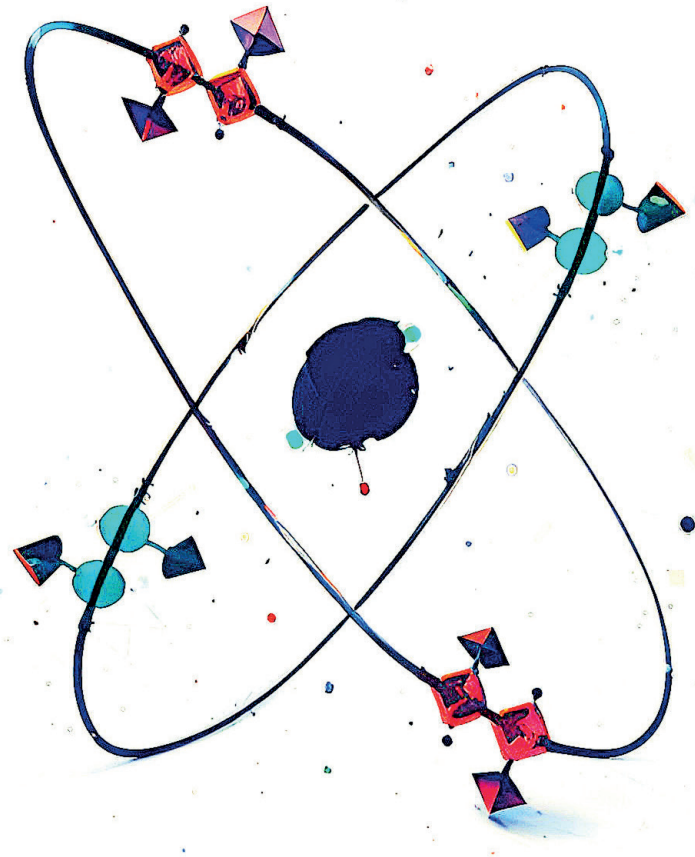George Lowani Zimba

Spectroscopy along the *N = Z* Line between Mass 70 and 84

UNIVERSITY OF JYVÄSKYLÄ

FACULTY OF MATHEMATICS
AND SCIENCE

George Lowani Zimba

Spectroscopy along the $N = Z$ Line between Mass 70 and 84

Editors
Ilari Maasilta
Department of Physics, University of Jyväskylä
Ville Korkiakangas
Open Science Centre, University of Jyväskylä

Cover picture: AI generated picture based on a drawing by George Lowani Zimba.
https://dream.ai/create

ABSTRACT

Zimba, George Lowani
Spectroscopy along the $N = Z$ line between mass 70 and 84

This thesis presents results from fusion-evaporation reaction experiments aimed to study nuclei in the $N = Z$ region. Specifically, new results obtained for the ^{70}Br, ^{70}Kr, ^{78}Y and ^{84}Mo nuclei are presented. The ^{84}Mo experiment identified the excited states up to the 6^+ state, and tentatively up to the 10^+ state. In addition, other suitable reactions to populate the excited states in ^{84}Mo were investigated. Further measurements of higher-lying excited states are required to determine the cause of the absent or delayed backbending in ^{84}Mo.

The recoil-β tagging method was used to study the excited states in the ^{70}Br, and ^{78}Y nuclei. Several new γ-ray transitions were observed from the decays of the excited states in the ^{70}Br nucleus. Moreover, the $T = 1$ band in ^{70}Br was extended up to the $J^\pi = 10^+$ state. Multiple new excited states were also observed in the ^{78}Y nucleus, including a new $J^\pi = 6^+$ state in the $T = 1$ band. The recoil-double-β tagging method was used for the first time to study the decays of the excited states in ^{70}Kr. Two γ rays were observed, which were assigned as the $2^+ \longrightarrow 0^+$ and $4^+ \longrightarrow 2^+$ transitions in ^{70}Kr.

The experimental results on the ^{70}Kr, ^{70}Br, and ^{78}Y nuclei can be used to investigate the charge-symmetry and charge-independence characteristics of the strong nuclear interaction.

Keywords: Isospin, Isospin-symmetry breaking, Proton-neutron pairing, Coulomb energy difference, Mirror energy difference, Triplet energy difference, Recoil-β tagging, Recoil-double-β tagging

TIIVISTELMÄ (ABSTRACT IN FINNISH)

Tämä väitöskirja esittelee fuusiohöyrystysreaktiokokeiden tuloksia, joiden tarkoituksena oli tutkia $N = Z$ alueen ytimiä. Erityisesti esitellään uusia tuloksia, jotka ovat saatu ^{70}Br, ^{70}Kr, ^{78}Y ja ^{84}Mo ytimille. ^{84}Mo ydintä käsittelevässä kokeessa ytimen viritystilat tunnistettiin 6^+ tilaan asti ja alustavasti 10^+ tilaan asti. Lisäksi tutkittiin muita sopivia reaktioita ^{84}Mo ytimen tuottamiseksi. Tässä työssä havaittiin, että vaaditaan yhä korkeampien viritystilojen mittaamista, jotta voidaan selvittää puuttuvan tai viivästyneen taipumispisteen syy ^{84}Mo ytimessä.

Rekyyli-β-merkkausmenetelmää hyödynnettiin ^{70}Br ja ^{78}Y ydinten viritystilarakenteen tutkimuksissa. Useita uusia γ-siirtymiä havaittiin ^{70}Br ytimen viritystilojen hajotessa. Lisäksi ^{70}Br ytimen $T = 1$ tilasarja tunnistettiin 10^+ tilaan asti. Useita uusia viritystiloja tunnistettiin myös ^{78}Y ytimessä, mukaan lukien $T = 1$ tilasarjan 6^+ viritystila. Rekyyli-tupla-β-merkkausmenetelmää käytettiin ensimmäistä kertaa virittyneiden tilojen hajoamisen tutkimiseksi ^{70}Kr ytimessä. Tässä analyysissä havaittiin kaksi γ-siirtymää, jotka liitettiin ^{70}Kr ytimen $2^+ \longrightarrow 0^+$ ja $4^+ \longrightarrow 2^+$ tilojen välisiin siirtymiin.

Saatuja kokeellisia tuloksia ^{70}Kr, ^{70}Br ja ^{78}Y ytimille voidaan hyödyntää vahvan ydinvuorovaikutuksen varaussymmetria ja varausriippumattomuus ominaisuuksien tutkimuksessa.

Author   George Lowani Zimba
                    Department of Physics
                    University of Jyväskylä
                    Jyväskylä, Finland

Supervisor   Dr. Panu Ruotsalainen
                    Department of Physics
                    University of Jyväskylä
                    Jyväskylä, Finland

                    Dr. Juha Uusitalo
                    Department of Physics
                    University of Jyväskylä
                    Jyväskylä, Finland

Reviewers   Dr. Adam Garnsworthy
                    TRIUMF
                    4004 Wesbrook Mall
                    Vancouver, BC V6T 2A3, Canada

                    Dr. Kathrin Wimmer
                    GSI
                    Planckstraße 1
                    Darmstadt, Germany

Opponent   Dr. Andrew Rogers
                    University of Massachusetts Lowell
                    220 Pawtucket St
                    Lowell, MA 01854, USA

PREFACE

This work has been carried out at the Accelerator Laboratory of the Department of Physics, University of Jyväskylä, Finland from 2019 to 2023.

First, I am incredibly grateful to Prof. Paul Greenless for giving me the opportunity to join the Nuclear Spectroscopy group at the University of Jyväskylä. I want to thank my supervisor, Dr. Panu Ruotsalainen. His guidance and support have been a great source of motivation throughout the Ph.D. journey. To my co-supervisor, Dr. Juha Uusitalo, your insights and expertise have been invaluable to me. I will always be grateful.

I want to thank Prof. Rauno Julin for the extremely fruitful and interesting nuclear structure discussions, which sometimes took place in the corridors. To Prof. Bob Wadsworth, I am grateful for the many discussions and for always being available when I needed your input. I would also like to thank Dr. Giacomo De Angelis and Dr. Giovanni De Gregorio for their contribution to this work with the theoretical calculations and many other discussions. Furthermore, I would also like to thank Dr. Nara Singh Bondili for his insight and for taking the time to read the thesis.

I also want to thank the Nuclear Spectroscopy group for welcoming me to the group and for all the excellent support, specifically from Dr. Jan Saren and Dr. Panu Rahkila. To my fantastic officemates, Minna and Lama, it was nice sharing the working space with you, and I'm extremely grateful for all the memories we have created at work and outside of work. Thanks for the many physics discussions and positivity throughout the challenging times.

I want to thank all the friends I have made during this journey. Life would have been sad without all the sports events, the wine, traveling, game night, dinner night, and all the activities you allowed me to participate in (Afra, Arus, Aysegul, Daniel, Deniz, Hussam, Jaakko, Joonas, Juha, Lydia, Marjut, Miguel, Mikko, Mounia, Sanae, and Tasos).

Finally, I want to express my deepest gratitude to my family: Annette (my partner), my sons, sisters, mum, and dad. Their unwavering support, encouragement, and understanding have been instrumental in my success.

Jyväskylä, George Lowani Zimba

ACRONYMS

JYFL-ACCLAB	Accelerator Laboratory, Department of Physics, University of Jyväskylä
DAQ	Data acquisition
MARA	The Mass Analysing Recoil Apparatus
MWPC	Multiwire proportional counter
TUIKE	Position sensitive plastic scintillator for β-particle detection
ToF	Time of flight
M/Q	Mass-to-charge ratio
RBT	Recoil-β tagging method
$\mathbf{R}_{\mathrm{DCO}}$	Directional correlations of oriented states
IAS	Isobaric analog states
INC	Isospin non-conserving
CED	Coulomb energy differences
MED	Mirror energy differences
TED	Triplet energy differences

CONTENTS

ABSTRACT
TIIVISTELMÄ (ABSTRACT IN FINNISH)
PREFACE
ACRONYMS
CONTENTS

1 INTRODUCTION

A nucleus is the center of an atom that has protons (positively charged) and neutrons (neutral). These particles are held together by a fundamental force called the strong nuclear force. The size, shape and stability of an atomic nucleus are determined by the number of protons (Z) and neutrons (N) it contains. There are two boundaries, the neutron and proton drip lines, that mark the limits of the existence for atomic nuclei. The boundaries determine where nuclei become unbound. The proton-drip line is closer to the valley of stability because of the Coulomb repulsion between the protons in the nucleus. The differences between the nuclei located near the proton and neutron drip lines are exhibited as different nuclear physics phenomena.

Atomic nuclei having (nearly) the same number of N and Z have gathered significant interest due to the fascinating physics phenomena that arise from these systems. The $N \approx Z$ nuclei provide the best quantum laboratory to investigate competition of the neutron-proton (np) pairing interaction between the isovector ($T = 1$) and isoscalar ($T = 0$) channels [1], the breaking of isospin symmetry [2], as well as shape coexistence and increasing collectivity [3, 4].

Until very recently, the available experimental nuclear structure data for nuclei with $N \approx Z$ in the mass (A) region of 60 - 90 were relatively scarce. This is due to the fact that these nuclei are located far from the line of stability, resulting in low production cross sections in nuclear reactions and presenting a challenge for the experimental detection sensitivity. However, owing to the recent technical advances in experimental methodologies and the availability of radioactive ion beams, structural data for the heavier $N = Z$ nuclei have started to emerge [5–15]. These data are crucial for scrutinizing and developing various theoretical models. Overall, the emergence of these experimental data will help to improve our understanding of the nuclear structure.

Figure 1.1 illustrates the portion of the nuclear chart relevant to the present work, namely $N = Z - 2$, $N = Z$, and $N = Z + 2$ nuclei with mass $A = 70 - 88$. Nuclei located near the $N = Z$ line are of great interest for multiple reasons. For example, for nuclei around
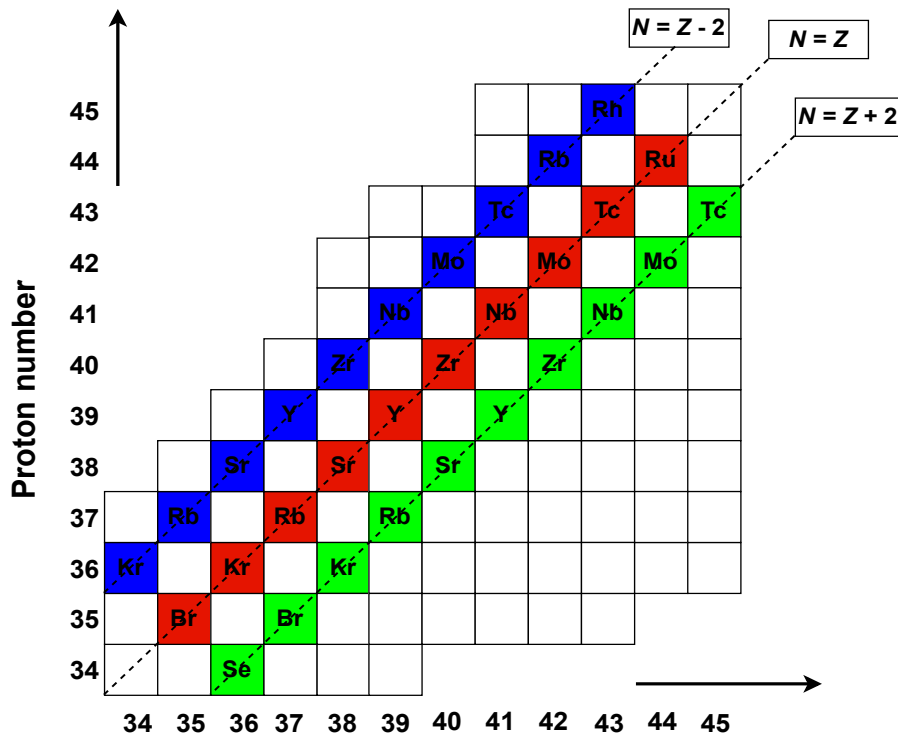
Figure 1.1: Illustration showing $N = Z - 2$, $N = Z$, and $N = Z + 2$ nuclei between mass numbers 70 and 88. **Blue** squares indicate $N = Z - 2$ nuclei. **Red** squares indicate $N = Z$ nuclei and **green** squares indicate $N = Z + 2$ nuclei. This is the region of interest in this thesis.

$A = 70$ and above, the structure of these nuclei is expected to become more complex, with multiple orbitals playing significant roles in determining the nuclear properties. In contrast, for the $N = Z$ nuclei in the mass region of 40 - 50, the $f_{7/2}$ orbital dominates the observed nuclear structure properties. Previous studies have indicated an abrupt structural change when moving towards the $A = 70 - 80$ nuclei in the $N = Z$ region, driven by the increasing influence of the $g_{9/2}$ orbital, resulting in various phenomena such as shape coexistence.

The experimental results presented in this thesis were made possible by recent advancements in scientific instrumentation, radiation detection technology, and novel measurement methodologies. These advancements led to an increase in experimental detection sensitivity, providing new nuclear structure data for the $N \approx Z$ nuclei in the $A = 70 - 84$ mass region. This thesis focuses on the experimental investigation of nuclei located near the $N = Z$ line, with particular theoretical emphasis on exploring the importance of the in np pairing correlations and the breaking of isospin symmetry. These nuclei are significant not only for the nuclear structure, but also for the related fields such as standard model tests [16] and nuclear astrophysics [17]. For example, ^{84}Mo is a waiting point[1] nucleus in the rapid-proton capture process [17, 18].

---

[1]   Waiting points refer to nuclei with low or negative proton capture Q-values, which hinder further proton capture. This phenomenon is more likely to occur at even-Z nuclei due to the lower proton binding energy of odd-Z nuclei.

1.1 Thesis Overview

Chapter 2 introduces the physics of interest relevant for the studied nuclei and discusses the predicted nuclear physics phenomena that are directly relevant to this thesis. Chapter 3 covers the details of the experimental equipment and methodologies used in this thesis and introduces the experiments, which were performed at the Accelerator Laboratory, Department of Physics, University of Jyväskylä, and explains the specifics of the fusion-evaporation reaction mechanisms.

In chapter 4, the results from the ^{28}Si(^{58}Ni,2n)^{84}Mo fusion-evaporation reaction are presented. The first part of this chapter describes the different fusion-evaporation reactions used to study excited states in ^{84}Mo and presents the reaction cross-section estimates obtained from these data. Additionally, this chapter discusses the background subtraction methods used to extract the weak γ-ray transitions originating from the decay of excited states in ^{84}Mo. The final section of the chapter presents and discusses the systematics of nuclei around the $N = Z$ line.

The results from the fusion-evaporation reaction ^{40}Ca(^{32}S,pn/2n), which was used to populate the excited states in ^{70}Br/^{70}Kr, are presented in chapter 5. The recoil-β-tagging (RBT), and recoil double-β (RDBT) techniques were utilized to search for transitions originating from ^{70}Br and ^{70}Kr. In addition, this chapter presents the predictions obtained from shell-model calculations and compares these to the experimental results for ^{70}Br. The chapter also includes a comparison of the experimental Coulomb energy differences to the theoretical values from two different SM calculations for ^{70}Br. In the last section of the chapter, the results for ^{70}Kr obtained by using the recoil-double-β tagging method and a comparison to the other experimental results are presented. Experimental mirror and triplet energy differences for the $A = 70$ triplet are also presented in section 5.5 of chapter 5, which are then compared to the SM calculations from Ref. [19].

In chapter 6, the results from the fusion-evaporation reaction ^{40}Ca(^{40}Ca,pn) aimed at studying the excited states in the ^{78}Y nucleus using the RBT method are presented. This chapter also compares the experimental Coulomb energy differences for the $A = 78$ pair to the theoretical values published previously in Ref. [19]. The last chapter of the thesis, chapter 7 summarizes the presented work and presents future research opportunities.

2 THEORETICAL FRAMEWORK

This chapter presents the physics background of this work from the theoretical point of nuclear structure in the mass region of interest.

2.1 Isospin formalism

The idea of isospin was first introduced by Heisenberg in 1932 [20], and it is built on the premise that the proton and neutron are different projections of the same particle, the nucleon. Both the neutron (n) and proton (p) have an isospin projection quantum number (t_z) equal to $+1/2$, and $-1/2$, respectively [21]. In multi-nucleon systems, the t_z of individual nucleons couple together to form a total isospin projection T_z, given by, $T_z = (N - Z)/2$. The total isospin T of a multi-nucleon state is obtained as a vector sum of the isospins of the individual nucleons. The integer values of the total isospin T of the system can range from $|N - Z|/2$ to $(N + Z)/2$. The indiscriminate handling of protons and neutrons as being the same particle is founded on the approximation that the nuclear strong force is both charge symmetric ($V_{nn} = V_{pp}$) and charge independent ($V_{np} = (V_{nn} + V_{pp})/2$). Therefore, the notion of isospin is established in symmetry after eliminating Coulomb effects from the interactions between the nucleons within the nucleus.

Consider one of the simplest nuclear systems, that of the mass number $A = 2$, which can be comprehended through the illustration presented in Fig. 2.1. For the $A = 2$ system shown in Fig. 2.1, the proton-neutron configuration (the $T_z = 0$ case) can result in either a parallel proton-neutron isoscalar $T = 0$ configuration or an antiparallel proton-neutron isovector $T = 1$ configuration. However, for the $T_z = \pm 1$ projections, the Pauli exclusion principle prohibits the parallel configuration of the like nucleons (proton - proton or neutron - neutron). Thus, the isoscalar $T = 0$ configuration is not possible for the $T_z = \pm 1$ systems, and only $T = 1$ is allowed. In the $A = 2$ isobar, only the $T = 0$, $T_z = 0$ case member is
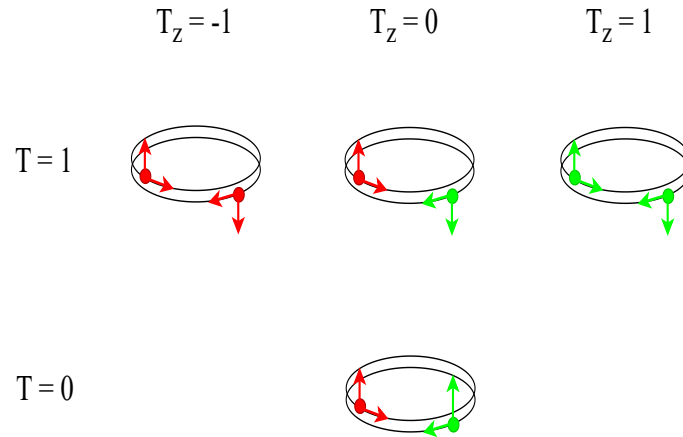
Figure 2.1: Sketch representing the pairing of nucleons. The protons (**red**) and neutrons (**green**) that form the pair occupying time-reversed orbits. Identical nucleons must have antiparallel spins, a configuration that is also allowed for a neutron-proton pair (top). These are termed as isovector pairs. The configuration with parallel spin is only permitted for a neutron-proton pair (bottom). This is called the isoscalar pair.

bound, being the ground state of deuterium, while the $T = 1$ states are all unbound. The three members of an isobar with $T_z = -1$, 0, and +1 are collectively referred to as an isobaric analog triplet and the excited states in these systems as isobaric analog states (IAS).

The analogy described above can be further expanded to include heavier nuclei that are centered around an odd-odd $N = Z$ nucleus. This nucleus can be viewed as comprising nucleon-nucleon pairs on top of an even-even $N = Z$ nucleus. It is expected that the isovector $T = 1$ states will be observed in all members of the isobaric triplet, reflecting excitations relative to the antiparallel nucleon-nucleon pairs. On the other hand, $T = 0$ states are only anticipated to occur within the $T_z = 0$ member. The hypothesis of isospin symmetry of the nuclear force suggests that all $T = 1$ states are degenerate across the isobaric analog triplet after accounting for isospin breaking effects, such as the repulsive Coulomb interaction between protons. It is essential to acknowledge that the $A = 2$ isobaric example is a simplified representation and that the coupling of states with equal T leads to energy level shifts. The use of the $A = 2$ isobaric triplet centered on an odd-odd $T_z = 0$ nucleus (deuterium) is favoured as it provides a straightforward, simple explanation of the isospin concept. The same arguments can apply to $T_z = \pm 1/2$ pairs and isobaric triplets centered around an even-even $T_z = 0$ nucleus.

From the premise of isospin symmetry, experimental studies of the of excited states across an isobaric triplet can shed light on the strong nuclear force. However, it is experimentally challenging in the general case since the ground state of a nucleus tends to have the lowest isospin quantum number. For instance, the ground-state band of a $T_z = 0$ nucleus is anticipated to possess an isoscalar $T = 0$ configuration. Nevertheless, when it comes to nuclei with A $\geq$ 50, the ground-state band of odd-odd $N = Z$ nuclei were found to have an isovector $T = 1$ configuration. Thus, in heavier odd-odd T_z nuclei, the ground state is $T = 1$, while the $T = 0$ states are located about $\sim$1 MeV above the ground state. This leads to the fact that the excited $T = 1$ states become non-yrast and are therefore populated weakly

in fusion evaporation reactions.

Experimental observations have revealed differences between the excitation energies of IAS caused by isospin non-conserving forces. These disparities in excitation energies, known as Coulomb Energy Differences (CED), have provided valuable information about nuclei's microscopic and macroscopic structure [12, 22, 23]. The CEDs are derived from the energy differences of IAS between the $N = Z$ ($T_z = 0$) and $N = Z + 2$ ($T_z = +1$) nuclei. Comparing energies of excited states in $N = Z$ - 2 and $N = Z + 2$ mirror pairs produces Mirror Energy Differences (MED), while the energy differences across IAS in the full isobaric triplet yield Triplet Energy Differences (TED).

2.1.1 Coulomb, Mirror, and Triplet energy differences

The definition of the CED between two analog states with spin J and isospin T is as follows

$$\text{CED}(J) = E(J, T, T_z = 0) - E(J, T, T_z = +1), \tag{2.1}$$

such that $T_z = 0$ represents the isospin projection for the $N = Z$ nuclei, and $T_z = +1$ represents the isospin projection for the $N = Z + 2$ nuclei. Electromagnetic interactions dominate the differences between the energies of the analog excited states. In addition, CEDs are also predicted to be sensitive to small structural changes [12]. When neutron and proton numbers are interchanged, ($T_z = \pm 1$ mirror nuclei) and differences in electromagnetic interactions are normalised/removed and the IAS are expected to be degenerate. However, deviation from degeneracy has been experimentally observed in $T_z = \pm 1$ mirror nuclei, which points to the presence of isospin non-conserving (INC) interaction or to the fact that the nuclear force is not perfectly charge symmetric. This latter is of course known to be the case from nucleon scattering data [24–26]. The MEDs, which represent energy level differences for nuclei with $T_z = \pm 1$, are defined as follows

$$\text{MED}(J) = E(J, T, T_z = -1) - E(J, T, T_z = +1). \tag{2.2}$$

The triplet energy difference (TED) across an isobaric triplet is defined as

$$\text{TED(J)} = E(J, T, T_z = -1) + E(J, T, T_z = +1) - 2 * E(J, T, T_z = 0). \tag{2.3}$$

The TED is calculated based on Eq. 2.3 and reflects the difference between average of the interactions between like-nucleons (pp and nn) and the neutron-proton (np) interaction. The TEDs are sensitive to the impact of electromagnetic effects and other INC interactions. On the other hand, the CED and MED include contributions from monopole Coulomb effects, such as single-particle Coulomb shifts, changes in nuclear shape or radius, and the electromagnetic spin-orbit interaction. Theoretical description of CED, MED, and TED evolution has succeeded within the shell-model (SM) framework for the nuclei in the sd and $f_{7/2}$ shells owing to the small valence spaces and data availability. The SM analysis has highlighted the need for an additional effective INC interaction that is required to reproduce experimentally observed TED (MED, and CED) trends [27, 28]. Available

experimental data on TED for isobaric triplets in the A = 18 - 66 mass region occupying sd, pf, and pfg shells have been compiled in Ref. [28]. Data for the heavier triplets at A = 70 and 74, and 78 are relatively scarce since the proton-rich members ($N = Z$ - 2) of the triplet are very challenging to access experimentally due to the low production cross sections.

2.1.2 Pairing correlations in $N = Z$ nuclei

Nuclei that have an equal number of protons and neutrons, or $N = Z$ nuclei, offer a unique environment to investigate the role of the neutron-proton pairing correlations. This is due to the fact that both the neutrons and protons occupy the same single-particle orbitals, leading to a maximal spatial overlap of their wave functions. This should result in enhanced proton-neutron pairing correlations, both in the isovector $T = 1$ channel and in the isoscalar $T = 0$ channel. In nuclei away from the $N = Z$ region, the nn and/or pp isovector $T = 1$ pairing mode is known to dominate due to the restriction arising from the Pauli exclusion principle. However, for the $N = Z$ nuclei in the medium-mass region, there is limited evidence for a strong $T = 0$, np correlations until in the A = 80 - 90 mass region [1], and even there the evidence has been greatly questioned.

The current thesis does not intend to comprehensively review the theoretical and experimental work on np paring. Instead, it will only cover the theoretical background essential for discussing predictions concerning the strength of the pairing correlations and their experimental evidence, emphasizing the rotational response. It has been suggested that the investigation of the rotational response of nuclei can potentially be used to study the importance of the different np pairing modes. Figure 2.2 demonstrates a plot of angular momentum (I) as a function of rotational frequency ($\hbar\omega$) for a set of $N = Z$ and $N = Z + 2$ nuclei in panels (a) and (b), respectively. As shown in Fig. 2.2 (a), the $N = Z$ nuclei exhibit a smooth behavior compared to their neighboring heavier even-even isotopes, which show sharp backbendings (^{82}Zr, ^{86}Mo, and ^{88}Ru) or upbending (^{78}Sr). This observation suggests that np pairing is more rugged against backbending and the Coriolis anti-pairing force, which starts to break the nucleon-nucleon pairs with an increase in angular momentum. In this picture, like nucleon pairs (nn or pp), having the spins initially antiparallel, align their spins along the rotational axis due to the Coriolis anti-pairing effect, which eventually breaks the pair and leads them to lose the pairing energy. According to the analysis performed in Ref. [29], the np pairs with parallel spins ($T = 0$ pairing mode), are not broken, but continuously created during the rotation. This leads to a scenario where a ground-state band with $T = 1$ pairing is crossed by a band with $T = 0$ pairing at a specific crossing frequency resulting in a smooth rotational evolution.

Shell-model (SM) calculations reported in Ref. [29] demonstrate that the enhancement of the $T = 0$, np interaction at high angular momentum in the $N = Z$ nucleus ^{88}Ru results in a smooth evolution of the moment of inertia. This is illustrated in Fig. 2.3 (a), where a theoretical calculation without the $T = 0$, np pairing interaction shows nearly identical patterns for all ^{88,90,92}Ru in contrast to the smooth behavior observed experimentally in
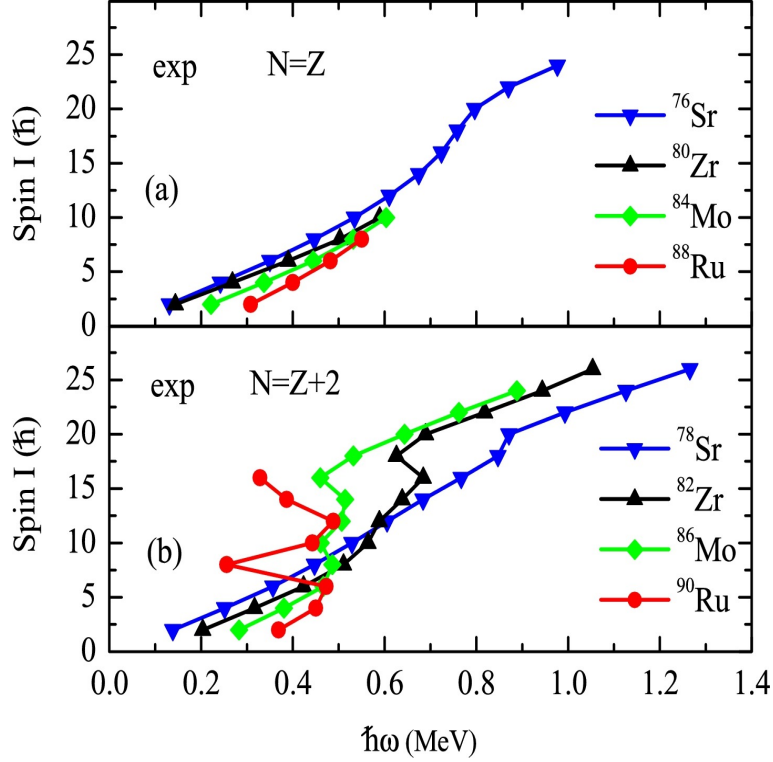
Figure 2.2: Experimental $I - \hbar\omega$ plots for yrast bands of (a) $N = Z$ nuclei ^{76}Sr, ^{80}Zr, ^{84}Mo, and ^{88}Ru, and (b) $N = Z + 2$ nuclei ^{78}Sr, ^{82}Zr, ^{86}Mo, and ^{90}Ru. Reprinted from Ref. [29] with permission from Elsevier.

the case of ^{88}Ru as shown in Fig. 2.2 (a). In addition, it is demonstrated in Fig. 2.3 (b) that the $T = 0$ multipole correlations (V_M) are primarily responsible for the smooth evolution of the yrast band. In contrast, $T = 0$ monopole correlations (V_m) further delay the band crossing frequency. Another theoretical work based on Hartree-Fock-Bogoliubov calculations suggests that the delayed band crossing frequencies in the case of $N = Z$ nuclei indicate the presence of enhanced $T = 0$, np correlations [30]. However, the smooth rotational behavior observed in the $N = Z$ nuclei has also various other theoretical interpretations. Firstly, it has been contested whether the band crossing frequency delays may originate (at least partly) from deformation changes [30]. Some models, such as the ones used in Refs. [31–33] suggest that there is no clear evidence of $T = 0$, np pairing correlations despite not excluding their existence. The theoretical interpretations regarding the importance of the np pairing correlations in the $T = 0$ channel are rather diverse [29, 34]. Furthermore, theoretical models still lack the experimental data for rigorous comparisons, especially in the case of heavier $A > 80$, $N = Z$ nuclei, where only a few of the lowest yrast levels have been observed experimentally. Therefore, it is critical to extend the yrast bands to a higher spin to solve the conundrum related to the importance of the $T = 0$, np pairing mode.
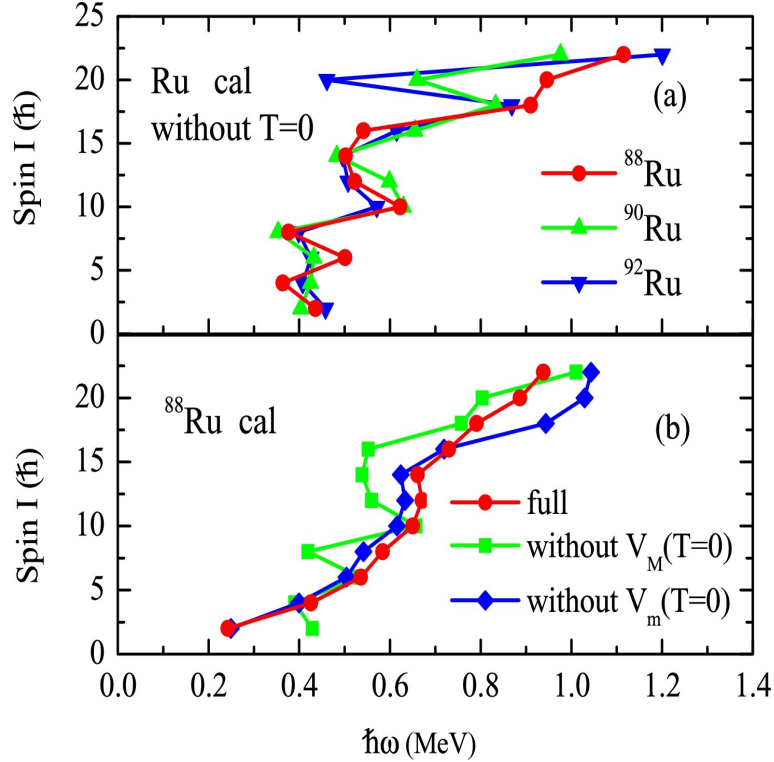
Figure 2.3: Calculated spin (I) against rotational frequency ($\hbar\omega$) plots for yrast bands of (a) ^{88,90,92}Ru without $T = 0$ interaction, (b) ^{88}Ru without $T = 0$ multipole (V_M) or monopole (V_m) interaction. Reprinted from Ref. [29] with permission from Elsevier.

2.2 The shell model

A major advancement in the interpretation of nuclear structure was brought about by the advent of the nuclear shell model (SM), proposed by Haxel, Jensen, and Seuss [35] and Goeppert-Mayer [36]. This development was based on the realization that incorporating a strong spin-orbit interaction resulted in the separation of orbitals that accurately accounted for the observed "magic numbers" of protons and neutrons, as illustrated in Fig. 2.4.

The SM has now developed from describing the nuclear binding energies in the area near closed shells and can now predict and explain nuclear structure phenomena far from such regions. Originally, the SM was only based on an independent-particle model, where nucleons were treated as moving within a mean field, unaffected by their neighbors. Further components, such as the Coulomb interaction and nucleon-nucleon interactions, were incorporated by adding a perturbative residual interaction. As a result, the SM Hamiltonian is defined as, H = $H_0 + H_{res}$. H_0 represents the mean-field Hamiltonian, and H_{res}, which represents the small perturbative residual Hamiltonian. The next step will be to solve the many-body eigenvalues given by

$$H|\Psi_n\rangle = [H_0 + H_{res}]|\Psi_n\rangle = E_n|\Psi_n\rangle, \tag{2.4}$$

where Ψ_n represents a many-nucleon state corresponding to an eigenenergy E_n for a particular state. The quantum many-body problem is solved by using numerical methods, yielding the level energies and wave functions of the states in the nucleus of interest. The
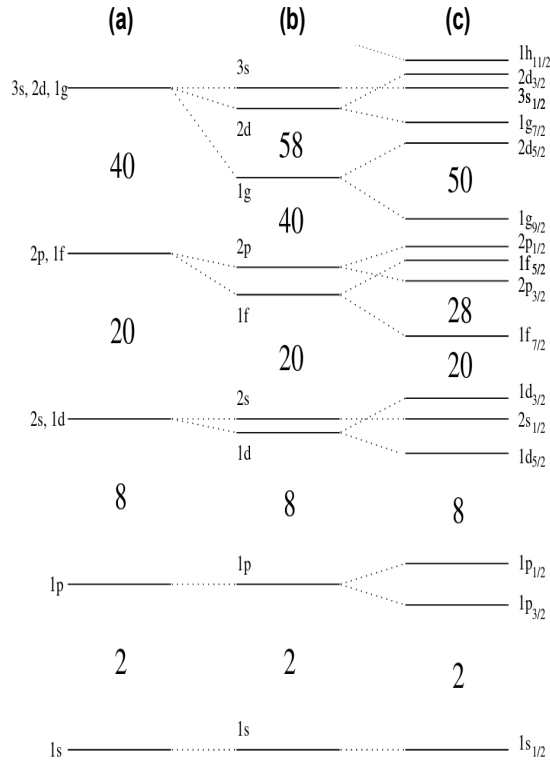
Figure 2.4: An illustration of the nuclear shell structure showing the single-particle energy levels of (a) a harmonic oscillator, (b) Woods-Saxon potential, and (c) Woods-Saxon potential plus spin-orbit interaction. The right side of the diagram shows the splitting of the single-particle orbitals due to the strong spin-orbit coupling force and the emergence of the additional magic numbers 28 and 50.

results are then compared to experimental data, and adjustments or improvements to the parameterization of the Hamiltonian are made if necessary to fit the experimental data.

Due to the many-body nature of the nucleus, calculations that explicitly involve all nucleons become computationally infeasible, even when using the mean-field approximation. To simplify the SM problem, it is often treated as if it consists of valence nucleons orbiting an effectively inert "core." The problem is further simplified by restricting the valence space through truncation, which is usually accomplished by only taking into account a limited number of shell-model orbitals above the inert core.

In the region of interest of the current thesis, an inert, $^{56}_{28}\text{Ni}_{28}$ core is used, with a truncated valence space consisting of the $p_{3/2}$, $f_{5/2}$, $p_{1/2}$, and $g_{9/2}$ orbitals. This simplification of the valence space allows for the diagonalization of the necessary matrix elements. However, a consequence of this simplification is that the residual interaction can no longer be derived from the fundamental interaction data, such as nucleon-nucleon scattering data. As a result, phenomenological effective interactions are used. The range of these effective interactions is generally confined, and they are usually designed for a specific region of the nuclear landscape. However, theoretically investigating CEDs, MEDs, and TEDs using SM calculations can be a challenging task as the experimental energy differences range

from only few keV to about 100 keV. Although the theoretically calculated CED, MED, and TED from SM may have some inaccuracies, the overall trend is usually consistent with the experimental results, which is more critical for understanding the underlying physics. Understanding the various SM terms that contribute to the observed CED, MED, and TED trends is essential. The following SM terms play important roles in the theoretically calculated CED, MED, and TED trends.

To understand the various components of the SM that lead to the observed CED, MED, and TED results, it is necessary to divide the Coulomb interaction (V_C) into two parts, namely monopole (V_{Cm}) and multipole (V_{CM}) components. The monopole part involves single-particle properties and bulk behavior, and the multipole part represents Coulomb effects that result from the angular momentum recoupling of valence protons. The Coulomb term V_{Cm} is further broken down into the radial component V_{cr}, the single-particle correction term ϵ_{ll}, and the electromagnetic spin-orbit term ϵ_{ls}.

2.2.1 Relevant shell model terms to CED, MED, and TED predictions

2.2.1.1 Radial term

The SM takes into account the valence nucleons and an inert core. It is important to note that although the core is inert, it is still charged and exerts a Coulomb force on the valence protons. To accurately calculate using the SM, the Coulomb force contribution from the core must be considered. The radial term V_{Cr} explains how nuclear radius changes along the rotational band. According to the SM approach, nuclear radius changes may not depend on nuclear deformation [23]. The magnitude of the radial term depends on which orbitals are occupied, as they have varying radii. Orbitals that are closer to the charged core have smaller radii, causing protons in those orbitals to feel a stronger Coulomb repulsion, causing the corresponding states to have more Coulomb energy. The monopole Coulomb radial contribution can be calculated using the following formula [2]

$$V_{Cr}(J) = T_z \alpha_r (m_\pi(g.s) + m_\nu(g.s) - m_\pi(J) + m_\nu(J)). \tag{2.5}$$

The occupation numbers for radius-driving orbitals ($p_{3/2}$ for A = 40 - 56 nuclei and $g_{9/2}$ for A = 56 - 80 nuclei) for neutrons and protons are denoted by m_ν and m_π, respectively, while α_r is a constant that is based on empirical data.

2.2.1.2 Single-particle correction term

The single-particle correction ϵ_{ll} term in the SM accounts for the difference between the nucleons' actual single-particle energies and the shell model's average single-particle energy. The ϵ_{ll} term affects the individual nucleons' energies, including neutrons and protons. However, in the monopole part V_{Cm}, the single-particle correction term only affects the proton orbitals because the Coulomb interaction depends on the proton charge.

Therefore, the single-particle correction term has a more significant effect on the proton energies and, consequently, on the Coulomb interaction of the protons. This contribution is described by the following equation [37]

$$\epsilon_{ll} = \frac{-4.5 Z_{cs}^{1.083} [2l(l+1) - N(N+3)]}{A^{1/3}(N + \frac{3}{2})} [\text{keV}], \qquad (2.6)$$

where Z_{cs} is the nearest closed shell of the orbital occupied by the proton. l and N refer to the orbital angular momentum and principal quantum number of the oscillator shell, respectively.

2.2.1.3 Electromagnetic spin-orbit term

The spin-orbit interaction is a well-known phenomenon that accounts for the separation of energy levels into their correct magic numbers. SM computations reveal that, although much weaker than the nuclear spin-orbit force, the electromagnetic spin-orbit interaction can be used to elucidate the experimentally observed energy disparities between IAS [2,19]. The electromagnetic spin-orbit potential, ϵ_{ls} can be generalized to

$$\epsilon_{ls} \simeq (g_s - g_l) \frac{1}{2m_N^2 c^2} \left(\frac{-Ze^2}{R_C^3} \right) < \vec{l} \cdot \vec{s} >, \qquad (2.7)$$

where g_s and g_l are the gyromagnetic factors, m_N is the nucleon's mass. The term $< \vec{l} \cdot \vec{s} >$ is equal to $l/2$ or $-(l+2)/2$ for the cases where $j = l + s$ or $j = l - s$, respectively. The ϵ_{ls} term affects neutron and proton orbitals differently. It can either decrease the energy of the neutron single-particle orbitals while increasing the energy of the proton orbitals or vice versa.

2.2.1.4 Multipole Coulomb term

The Coulomb multipole term (V_{CM}) reflects the energy difference required to reorient nucleon pairs, based on the combined spin and individual isospin projections of the pair. In the case of two protons, realigning the pair results in an alteration in their spatial separation, leading to a change in the Coulomb energy. Conversely, realigning neutron-proton or neutron-neutron pair results in no change in the Coulomb energy. The change in the Coulomb energy is reflected in the excitation energy of the state. In the case of TED, the systematic negative trends observed for the all isobaric triplets known experimentally to date, are primarily caused by the Coulomb multipole term. This is because the neutron-deficient $T_z = -1$, $N = Z - 2$ member of the triplet is having more proton-proton pairs than the other two members.

3 EXPERIMENTAL METHODS

Modern experimental techniques have allowed for the study of exotic nuclei in extreme regions of the nuclear chart, such as areas close to the proton-drip line. The $N = Z$ line is close to the proton-drip line for nuclei with mass numbers greater than 60. This makes experimental studies in this region particularly difficult due to the low production yields of these nuclei. The following chapter describes the experimental methods used to study the structure of ^{84}Mo, ^{78}Y, ^{70}Kr, and ^{70}Br. The first part of the chapter covers the reactions used to produce and populate the nuclei of interest, then the detection and identification techniques of these nuclei are discussed.

3.1 Fusion-evaporation reaction

To study the nuclear structure using γ-ray detector arrays, it is essential to populate the nuclei of interest with sufficient excitation energy corresponding to a desired angular momentum. One of the commonly used methods to study excited nuclear states is called fusion-evaporation reaction. In fusion-evaporation reactions, a projectile nucleus fuses with a target nucleus to create an excited compound nucleus. The projectile's kinetic energy must be high enough to surpass the Coulomb barrier separating the two interacting particles. The energy required to overcome the Coulomb barrier is approximated by

$$V_{tb} = \frac{Z_b Z_t}{A_b^{1/3} + A_t^{1/3}} \;\; [\text{MeV}], \tag{3.1}$$

where Z_b and Z_t, are the atomic numbers of the beam and target nucleus, respectively. A_b and A_t are the mass numbers of the beam and target nucleus, respectively. The compounds created in fusion-evaporation reactions are extremely excited and subsequently undergo particle evaporation (proton, neutron, α and/or combination of any of the three types of particles) before de-excitation via γ-ray emission. Detection of the evaporated particles help in the identification of the reaction product. Detection of the γ rays give information

on the nuclear structure. The excitation energy E^* of the compound system is defined by

$$E^* = E_{cm} + Q, \tag{3.2}$$

where Q is the reaction Q-value, given by energy conservation as the difference in the initial masses (mass of beam (m_b), and mass of target (m_t)) and mass of the compound formed (m_{CN}), multiped by c^2

$$Q = (m_b + m_t - m_{CN})c^2, \tag{3.3}$$

and E_{cm} is the center of mass kinetic energy of the compound nucleus given by

$$E_{cm} = \frac{A_t}{A_t + A_b}E_{lab}, \tag{3.4}$$

with E_{lab} as the kinetic energy in the laboratory frame. The relationship between the total production cross-section σ and the reaction rate R for the evaporation residue of interest can be determined as follows

$$\sigma = \frac{R}{N_t \cdot I_b}, \tag{3.5}$$

where I_b is the beam intensity and N_t is the number of target nuclei per unit area, which is given by

$$N_t = \frac{\rho d}{A}N_A. \tag{3.6}$$

In Eq. 3.6, ρ denotes the density of the target material, d represents the thickness of the target, and A is the mass number of the target. Additionally, N_A refers to Avogadro's number. The combination of Eqs. 3.5 and 3.6 gives the relation

$$\sigma = \frac{RA}{\rho d N_A I_b}. \tag{3.7}$$

The angular momentum of the compound system also depends on the mass of the beam particle, the projectile's kinetic energy and the target mass. The nuclei closest to the proton-drip line are typically produced with extremely low cross-section in comparison to the other channels. In this thesis, four nuclei around the $N = Z$ region were studied using various fusion-evaporation reactions, listed in the Table 3.1.

3.2 Instrumentation

The cross sections for the nuclei of interest in the present study are orders of magnitudes lower than those of the other reaction channels. Moreover, most of the beam passes through the target without interacting or is scattered from the target without nuclear interaction. To identify the recoil of interest, and to perform γ-ray spectrometry, there is a need to separate the nuclei of interest from the contaminant nuclei and the unreacted beam. Development

Table 3.1: List of nuclei of interest for this work, followed by beam, beam energy, target, target thickness, evaporation channel and calculated PACE4 [38] cross-section.

Nuclei	Beam	Beam energy [MeV]	Target	Target thickness [mg/cm^2]	Channel	Cross-section [mb]
^{84}Mo	^{58}Ni	201	^{28}Si			0.43
	^{32}S	107	^{54}Fe	0.5	2n	0.23
	^{40}Ca	124	^{46}Ti			0.14
^{70}Br	^{32}S	92	^{40}Ca	0.6 - 0.8	pn	6.32
		96				4.41
		103				1.86
^{70}Kr	^{32}S	92	^{40}Ca	0.6 - 0.8	2n	0.02
		96				0.03
		103				0.01
^{78}Y	^{40}Ca	120	^{40}Ca	0.6 - 0.8	pn	2.46

in the experimental equipment and techniques has made it possible to study these exotic nuclei. The experimental setup used in the current work included Mass Analyzing Recoil Apparatus (MARA) coupled to the JUROGAM III array, located at the target position. The charged-particle veto detector, JYU-Tube detector (Jyväskylä-York University Tube) was installed around the target. In addition, other detectors at the MARA focal plane were used. The following sections provide a brief overview of these devices.

3.2.1   The JUROGAM III Ge-detector array

Figure 3.1 shows one hemisphere of the JUROGAM III Germanium (Ge)-detector array [39], which was used to detect prompt γ rays around the target position. The JUROGAM III array inherited its characteristics from the Eurogam II array [40], which consisted of two types of Ge detectors, tapered single-crystal Phase1 detectors [41] and Clover detectors [42]. A common problem in the γ-ray spectroscopy is the Compton scattering. The γ rays that scatter out of the Ge-detector crystal leave only a fraction of their initial energy in the Ge crystal and therefore contribute to the background. To suppress the contribution from Compton scattering events in the γ-ray spectrum, each Clover and Phase 1 detector of the JUROGAM III array was accompanied by a heavy-metal collimator and bismuth germanate (BGO) Compton-suppression shield [41, 42]. The Compton-suppression method involves the detection γ rays in coincidence between the BGOs and Ge detectors. The γ-ray events that are in coincidence in the two detectors are considered to result from a scattered γ-ray leaving the Ge-detector crystal and being detected in the shield. At the same time, the heavy-metal collimators prevent the detection of γ rays emitted from the target directly by the BGO shields. The signal in both BGO and Ge detector is then exluded from the data based on the fact that the γ-ray energy detected in the Ge detector is not complete.

The detector modules (Ge detectors + BGO shield + heavy-metal collimators) are mounted in spherical configuration so that the reaction target is in the focus of the array. The JUROGAM III detectors are grouped into four rings at four different angles with respect to the beam axis. Rings one and two consists of five and ten Phase1 detectors, respectively,
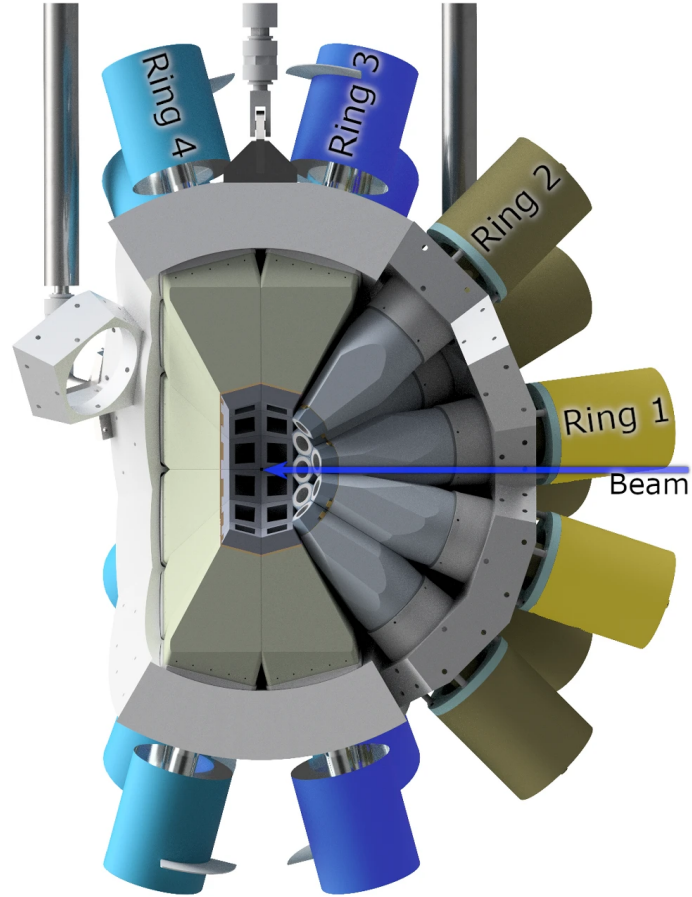
Figure 3.1: The JUROGAM III Ge-detector array drawing showing one hemisphere, supporting frame, and beam direction. Different detector rings have been labelled and marked with different colours. Adapted from Ref. [39].

at $157°$ and $133.6°$ with respect to the beam axis. Rings three and four each contain 12 Clover detectors at $104.5°$ and $75.5°$ with respect to the beam axis. The full JUROGAM III Ge array consists of 39 individual detector modules and 111 individual Ge crystals.

The recoils produced in the fusion-evaporation reactions usually move at 2 - 4% of the speed of light, thus it is necessary to apply Doppler correction to the observed γ-ray energies. The Doppler corrected γ-ray energies are given by

$$E_\gamma = \frac{E_0\sqrt{1 - \beta^2}}{1 - \beta cos\theta},$$

(3.8)

where E_0 is the measured γ-ray energy, β (v/c) is the speed of the recoil with respect to the speed of light, and θ is the γ-ray detection angle with respect to the velocity vector of the recoil.

A combination of radioactive ^{152}Eu and ^{133}Ba sources was used for energy and detection efficiency calibration to cover the energy range of interest. The relative detection efficiency of the JUROGAM III array as a function of the γ-ray energy was extracted, and the following function was fitted to the data points
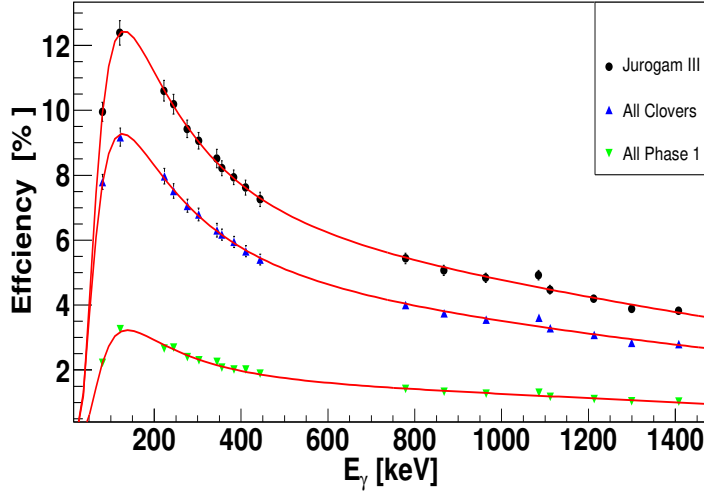
Figure 3.2: γ-ray detection efficiency for all detectors in the array (Jurogam III total), only Clover detectors (All Clovers) and only Phase 1 (All Phase 1) measured using ^{152}Eu and ^{133}Ba calibration sources. Solid curves represent the fits of Eq. 3.9 to the data.

$$\epsilon = exp\left\{ \left((a + bx + cx^2)^{-g} + (d + ey + fy^2)^{-g} \right)^{-\frac{1}{g}} \right\}. \qquad (3.9)$$

The total JUROGAM III array detection efficiency curve (Jurogam III), with JYU-Tube detector, is shown in Fig. 3.2, in addition, the efficiency curves for only Clover detectors (All Clovers) and only Phase 1 (All Phase 1) are also shown. More details on the JUROGAM III array performance and features can be obtained from Ref. [39].

3.2.2 Mass Analysing Recoil Apparatus (MARA)

The Mass Analysing Recoil Apparatus (MARA) is a vacuum-mode mass separator for the studies of fusion-evaporation residues. Its ion-optical configuration is a quadrupole triplet followed by an electrostatic deflector and a magnetic dipole (QQQED), as shown in Fig. 3.3. The MARA electrostatic deflector consists of two titanium plates separated by a distance of 14 cm with a radius of curvature of 400 cm and a height of 40 cm. This gives the anode a curvature of 407 cm and the cathode a curvature of 393 cm, respectively. The anode has a 1.5-cm gap from 10º to 19º along the principal beam axis, allowing most of the unreacted beam to go through without being in contact with the plate. The aperture does not significantly affect the electric field and has a small shims at the edges to maintain the field uniformity. The cathode and anode are independently biased using the F.u.G HCH

series 250-kV power supplies.
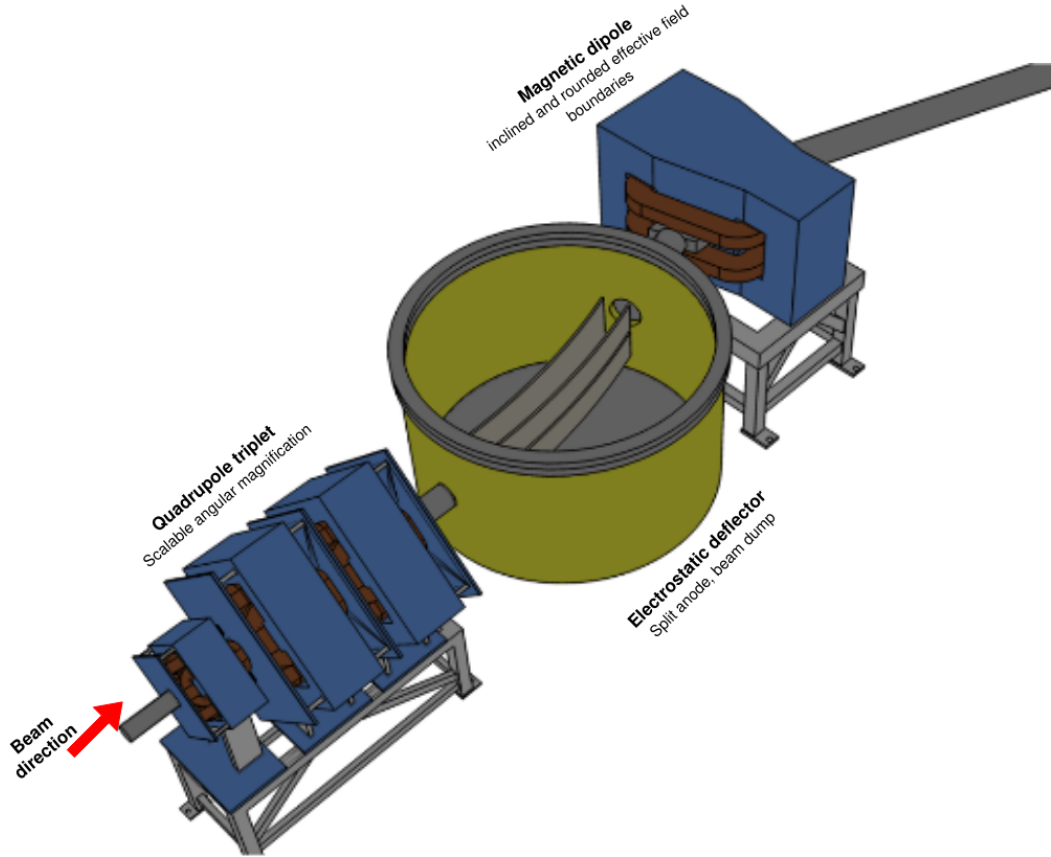
Figure 3.3: An artistic view of the MARA separator showing the ion-optical configuration. MARA consists of quadrupole triplet, the electrostatic deflector, and the magnetic dipole ($Q_M Q_M Q_M D_E D_M$).

The primary purpose of MARA is to separate the nuclei of interest from the other reaction products and beam-like products and transport the recoils of interest to the focal plane based on their mass-to-charge ratio. The separation of ions is achieved by utilizing the properties of motion of a charged particle in the presence of magnetic and electric fields. The Lorentz force describes the motion of a charged particle in the electric and magnetic fields as follows

$$\vec{\mathbf{F}} = q(\vec{\mathbf{E}} + \vec{\mathbf{v}} \times \vec{\mathbf{B}}), \tag{3.10}$$

where $\vec{\mathbf{E}}$ is the electric field, $\vec{\mathbf{B}}$ is the magnetic field, $\vec{\mathbf{v}}$ is the velocity and q is the charge of the particle. The electric field (E) between two parallel plates at a given voltage is given by

$$E = \frac{V}{d}, \tag{3.11}$$

where V is the voltage in [V], and d is the distance between the two plates in [m]. The force exerted on a charged particle by the electric field is the first term of the Lorentz Eq. 3.10

$$\vec{\mathbf{F}} = q\vec{\mathbf{E}}, \tag{3.12}$$

Using the two Eqs. 3.11, and 3.12, a term called "Electric rigidity," is introduced which describes the resistance of the path of an ion in motion under the influence of an electric field. Rigidity represents the radius of curvature of the charged particles. Electric rigidity depends on the kinetic energy and the charge of the ions. Ions with different rigidity will have different momenta and follow trajectories with slightly different path lengths. The electric rigidity χ_E is defined by

$$\chi_E = E\rho = \frac{pv}{q} = \frac{2E_k}{q}, \tag{3.13}$$

where ρ is the bending radius of the electric field, p is the momentum of the charged particle, v, q and E_k are the ions' velocity, charge, and kinetic energy. In addition, the magnetic rigidity depends on the kinetic energy, the charge of the ions and also the mass of the ions (m_o) The magnetic rigidity χ_M is defined by

$$\chi_M = \frac{p}{q} = \frac{\sqrt{2E_k m_o}}{q}. \tag{3.14}$$

The electrostatic deflector separates ions based on their energy and the magnetic dipole separates ions based on the momentum. A brief summary of the MARA details presented here are adapted from [43].

3.2.3 Ancillary instrumentation

3.2.3.1 Charged-particle veto detector (JYU-Tube detector)

The JYU-Tube detector array used in this work consists of 120 detector elements divided into two identical halves. Each detector element consists of 2-mm thick EJ-248 (downstream half) and EJ-200 (upstream half) scintillator tile glued to a 7.85-mm thick light guide coupled to a 6x6-mm^2 Silicon Photomultiplier (SiPM). The light guides are painted with TiO$_2$ paint and the individual elements are covered with aluminized mylar with thickness of 6 μm. The SiPMs are mounted onto a printed circuit boards (PCB) where their signals are read. Scintillators are arranged in 12 panels and two endcaps. Each panel has 2 x 4, 20x20-mm^2 square detectors. The endcaps are made of 12 scintillators, 6 square, and 6 rhombic detectors.

This configuration of the detector is simple, but sufficient to enhance the solid angle coverage. The solid angle covered by the entire JYU-Tube detector is approximately 97%. This value is overestimated since the two halves of the detector cannot be placed in contact due to the target holding mechanism being in between the tube halves, see Fig. 3.4. Table 3.2 provides a summary of the detector's detection efficiency for different fusion-evaporation reaction channels. The presented one proton detection and veto efficiencies shown were obtained from the ^{28}Si(^{58}Ni,xαypzn)^2 reaction by comparing the intensities of

---

2   x, y and z are the number of evaporated particles for the α, proton, and neutron, respectively. These numbers range from zero to the highest possible allowed number of evaporated particles.
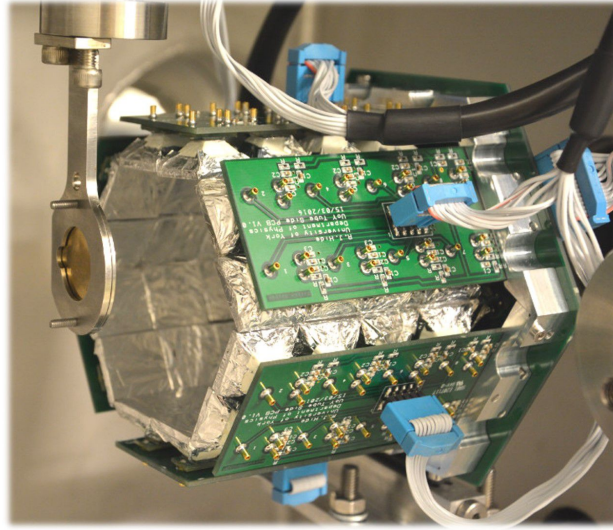
Figure 3.4: The downstream half of the charged-particle detector JYU-Tube installed at the target position of MARA.

γ-ray peaks originating from specific evaporation channels from spectra created with and without the conditions that charged particles were detected in the JYU-Tube detector.

Table 3.2: Measured total veto efficiency, one charged-particle detection efficiency and false veto probability of the JYU-Tube detector in the ^{28}Si(^{58}Ni,xαypzn) reaction.

	Veto efficiency [%]	**1p efficiency [%]**	**False Veto [%]**
pn, ^{84}Nb (295 keV)	73(2)	71(2)	2(1)
2p, ^{84}Zr (540 keV)	93(2)	74(2)	4(1)
2p, ^{84}Zr (720 keV)	93(2)	73(2)	10(3)
α2p, ^{80}Sr (385 keV)	96(2)	65(2)	1(1)

The extracted total veto efficiencies for the evaporation channels, pn, 2p, α2p are 73%, 93%, and 96%, respectively. The efficiency values can be affected by the presence of overlapping γ-ray lines in various nuclei, leading to slightly different efficiency values for different γ-ray lines, as shown in Table 3.2. This phenomenon has been observed for the 2p channel, where the efficiencies are slightly different. For more detailed description and performance of the JYU-Tube detector, see Ref. [44].

3.2.3.2 Focal plane detectors

Multiwire proportional counter

The Multiwire proportional counter (MWPC) is a gas detector used to track the passage of ions from the separator. MWPC consists of two wire planes (anodes) and a plane of aluminized mylar foil between (cathode). Delay lines separate the individual wires. The MWPC is filled with isobutane gas and closed on both sides by thin Mylar windows to separate the gas from the vacuum of MARA. The cathode at the ionization path collects the charge generated as an ion passes through the gas volume allowing for a fast signal to

be obtained for triggering. The position of the recoils passage through the detector is given by a time-to-amplitude converter (TAC) using the time difference of the signals collected from the both ends of anodes, which are read through the delay lines.
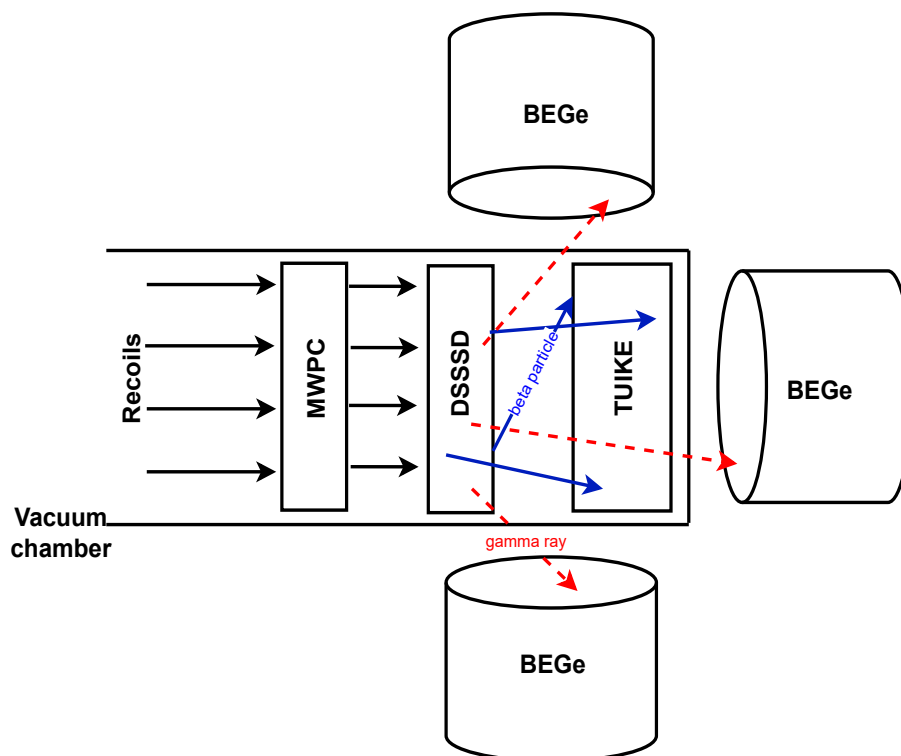
Figure 3.5: The diagram illustrates the detector arrangement in the MARA focal plane setup. One Clover detector is omitted for visual purposes. The detector dimensions are not in scale.

Double-sided silicon strip detector

Double-sided silicon strip detectors (DSSSD) have become increasingly widespread over the past decades as manufacturing techniques and reliability have improved. Silicon strip detectors use a high-quality layer of silicon dioxide (SiO_2) grown on the silicon to separate the finely segmented electrodes that are created by doping the silicon [45, 46]. The DSSSDs used in these experiments were BB20 type [47] with an active area of 128.61 mm x 48.21 mm with 192 vertical strips and 72 horizontal strips. In the present work, 300-[3] and 700-μm [4] thick detectors were used. The large number of active independent pixels of the detector enables to measure the position and energy of the implantation events, including high multiplicity event detection. The DSSSD is mounted in the vacuum chamber downstream from the MWPC at the MARA focal plane. Its placement at the focal plane is schematically shown in Fig. 3.5. The DSSSD was tuned and used for recoil detection and detection of their subsequent decays. To calibrate the DSSSDs, a mixed triple-α source containing ^{239}Pu, ^{241}Am, and ^{244}Cm was used. The decay detection efficiency of the DSSSD is around 50% due to the shallow implantation depth of the recoils. To enhance

---

[3]   used in the fusion-evaporation reaction ^{28}Si(^{58}Ni,xαypzn), ^{54}Fe(^{32}S,xαypzn), ^{40}Si(^{46}Ti,xαypzn) and ^{40}Ca(^{40}Ca,xαypzn).

[4]   used in the fusion-evaporation reaction ^{40}Ca(^{32}S,xαypzn).

the energy resolution, the DSSSDs are cooled down to -25 °C. An essential advantage of DSSSD is that it can measure the energy and both the x and y position for several particles that strike the detector simultaneously.

Position sensitive plastic scintillator for β-particle detection (TUIKE)

TUIKE, developed at the Department of Physics, University of Jyväskylä [48], shown in Fig. 3.6, is a position sensitive plastic scintillator detector used for measuring full energy of the β particles. The detector properties required for TUIKE were that the detector was wide and thick enough for efficient high-energy β particle detection, but relatively compact to fit at the MARA focal plane without significantly affecting the efficiency of the Ge detectors around the focal plane. TUIKE is placed in the vacuum chamber at 17 mm downstream from the DSSSD, as shown in Fig. 3.5. The active area of the TUIKE detector covers the whole area of the DSSSD. The dimensions of the scintillator are 140 x 80 x 30 mm^3 (width, height, and depth). The thickness of the TUIKE detector was selected to be enough to stop β particles with energies up to 5 - 6 MeV. Using the continuous slowing down approximation (CSDA), β particles of 7, 8, and 9 MeV will lose approximately 79, 70, and 63 % of their energy in TUIKE, respectively. It is important to mention that in most cases, the β particles do not hit the surface of TUIKE perpendicularly. As a result, the effective thickness of the detector seen by the β particles is greater than its total 30 mm active thickness.
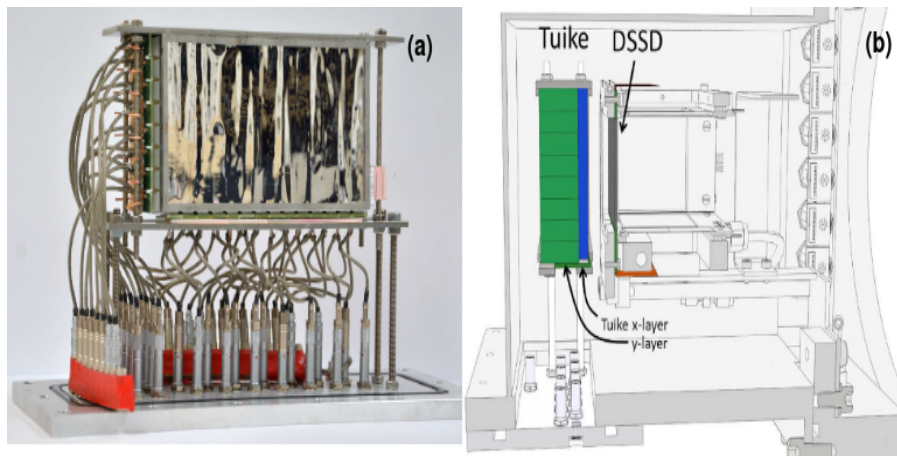
Figure 3.6: (a) Photograph of the scintillator detector, TUIKE, and (b) description of a drawing of the focal plane chamber with TUIKE and DSSSD detectors, where the green and blue colors correspond to the y and x layers of TUIKE, respectively. In the picture (b), recoil products come in from the right side of the image. The drawing is adapted from Ref. [48].

The TUIKE detector comprises two separate layers of scintillator material, shaped into rectangular bars, that are positioned orthogonally so that the first layer gives the x-coordinate, with single-bar dimensions of $10 \times 80 \times 6$ mm^3. The second layer provides the y-coordinate, with single-bar dimensions of 140 x 10 x 24 mm^3. Individual TUIKE bars have a frustum-shaped light guide on one end connected to the Silicon Photomultipliers (SiPM) manu-factured by SensL. Each SiPM in the TUIKE detector has a PCB with a filtering circuit for the bias voltage. The scintillator material used in TUIKE is the Eljen technology's

EJ-248 [49], and the light guides are made of polymethyl methacrylate (PMMA). To collect light effectively, each bar in the detector is covered with approximately 60-μm thick enhanced specular reflector (ESR) film made by 3M, and the light guides are painted with Eljen's EJ-510 TiO$_2$ paint. See Fig. 3.6 for a photograph of the entire scintillator detector adapted from [48]. For a more detailed description and performance of TUIKE, see Ref. [48].

Focal plane Germanium (Ge) detectors

Ge detectors at the MARA focal plane are generally used to detect the delayed γ rays (also X rays), hence identifying isomeric states, which decay via emission of γ ray transitions. The vacuum chamber at the MARA focal plane is surrounded by three Broad-Energy Germanium (BEGe) and one Clover detector. For more detailed description and performance of BEGe, see Refs. [50,51]. The BEGe detectors were calibrated using known γ-ray energies from ^{152}Eu and ^{133}Ba sources.

3.3 The Total Data Readout System

The triggerless Total Data Readout data acquisition system (TDR) [52] handles the electronic signals from each detector channel. The TDR system has no hardware trigger, therefore, data from each channel is recorded independently. The TDR system has a 100 MHz clock that provides timestamps for the data with 10 ns precision and synchronization pulses to all digitizer cards. Merging and collecting software then arranges the data in a single time-ordered stream. Due to the high counting rates of the "prompt" detectors, i.e, the JUROGAM III array and JYU-Tube, that collect a vast amount of data associated with reaction products which do not make it through the MARA separator to the focal plane, a pre-filter software is used. This is to prevent writing of this un-usable data to disk, and, hence, reduces the data volume. TDR allows the user to replay the data with the possibility of freely adjusting the software triggering conditions, event length and recoil-decay correlation search times and using various analysis tools in the analysis software.
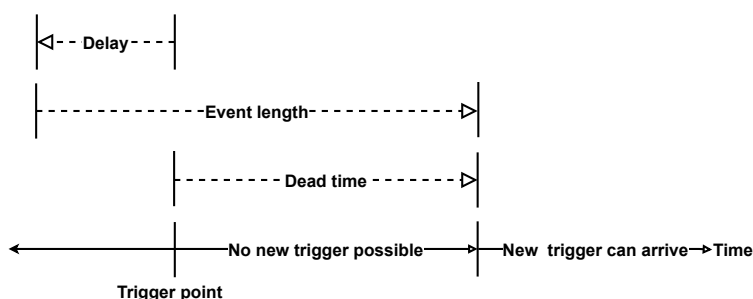
Figure 3.7: Illustration showing the triggering point, event length, delay and dead time.

In this work, the software trigger for an event was any signal from the y-side channels of the DSSSD. A signal above the threshold in the DSSSD, therefore, opened a time window

that defines an event. This event contains the possible information from the "prompt" detectors, but also from the focal plane detectors within the set event length. The total event length is typically 10 μs with -2 μs time window covering the preceding hits in JUROGAM III and JYU-Tube and +8 μs time window to cover, e.g., the isomeric γ rays detected at the MARA focal plane Ge detectors. A software dead time of 8 μs is also typically applied to prevent a new event being started, while the current event is being formed. Figure 3.7 shows the event formation parameters - event length, delay and dead time. In the current work, the events are further classified into "recoil events" and "decay events". The recoil events contain JUROGAM III, JYU-Tube, MWPC, and the focal plane Ge-detector information in addition to the relevant DSSSD information (recoil position and kinematic energy). The decay events contain TUIKE and focal plane Ge-detector data in addition to the DSSSD information (position and full or partial decay energy for α/proton and β particles, respectively).
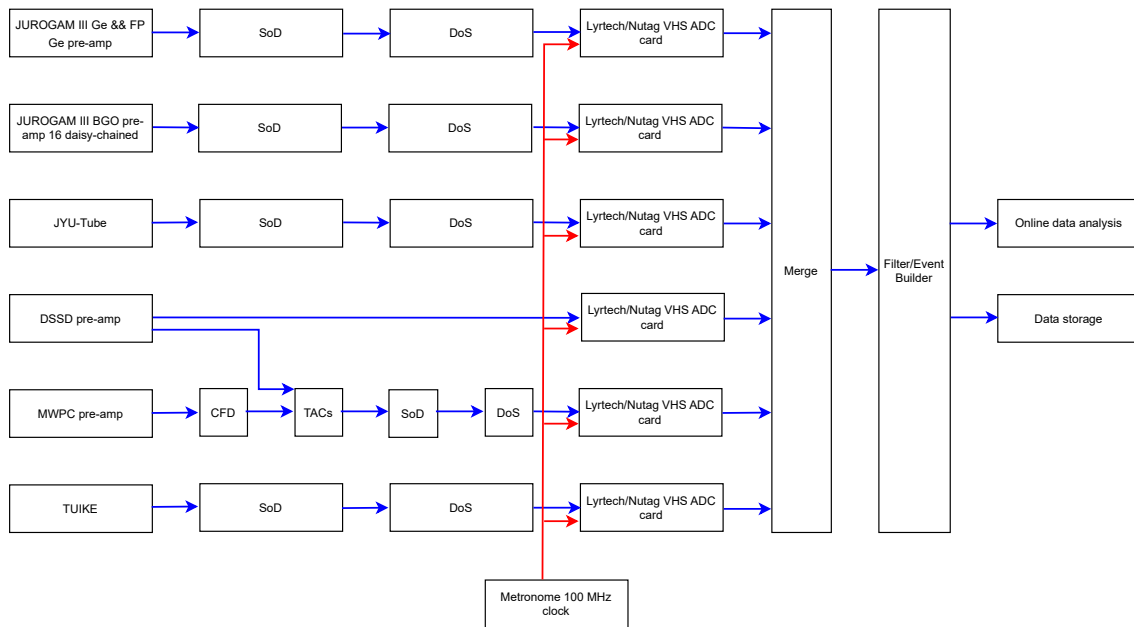
Figure 3.8: A block diagram of the electronics of the TDR system, showing the digital and analog signal pathways for the different detectors.

The signal paths in the TDR data-acquisition system are schematically shown in Fig. 3.8. To transport the signals from the measurement cave to the data acquisition (DAQ) room without degrading signal quality, the signals from the MWPC, Ge-detectors, BGOs, TUIKE detector, and JYU-Tube detector are converted to differential signals using 16-channel single-ended-to-differential (SoD) converter cards. This is made possible with the use of twisted-pair ribbon cabling. The signals are then converted back to single-ended using differential-to-single-ended (DoS) converter cards before being fed into the 14-bit Lyrtech/Nutaq VHS-ADC cards. To analyze the digitized detector signals and evaluate the energy, a Moving-Window Deconvolution (MWD) [53] algorithm is used. This algorithm is programmed into the field-programmable gate array (FPGA) circuit of the VHS-ADC cards. More details on the signal processing can be obtained from Ref. [54] and references therein. The timing signal from the DSSSD is sent to the Time-to-Amplitude Converter

(TAC) as the start input signal. The timing signal from MWPC provides a stop input signal to the previously mentioned TAC. The time difference between the DSSSD and the MWPC provides the time-of-flight (ToF) information for the recoils.

The offline data analysis (and online visualization) was performed using the GRAIN software package [55]. GRAIN allows a large variety of user-based techniques to be used in sorting and visualising data using a JAVA-based sort code. GRAIN enables the user to extract information on the radiation events in several ways, using one- or two-dimensional histograms and n-tuples [56, 57]. In this thesis, GRAIN was used to sort and analyze the data. In addition, ROOT software [58] was also used to visualize the data, chi-square minimization, and perform efficiency calibration of JUROGAM III.

3.4   Recoil identification

Accurate recoil event identification is important for the γ-ray spectroscopy of exotic nuclei. Although the majority of the beam-like particles are stopped in the MARA separator beam dump, some of them are transferred to the focal plane and implanted into DSSSD. To determine proper prompt γ-ray-recoil correlation, the primary and scattered beam components must be discriminated from the recoils. The MARA separator's focal plane detector setup offers an opportunity to distinguish nuclei of interest from the primary and scattered beam components utilizing the ToF information obtained from the MWPC and DSSSD detectors and energy information obtained from DSSSD. Based on the combination of the ToF and the obtained implantation energy deposited in the DSSSD by the recoils, E_{DSSSD}, the fusion recoils can be separated from the scattered beam components.

Figure 3.9 shows a two-dimensional matrix for ToF [a.u] as a function of the recoil energy measured in the DSSSD, E_{DSSSD} [keV]. Two distinct areas stand out in the graph, the scattered beam particles' ridge (indicated as the **red** region) extends from the long flight times down to shorter flight times covering the whole energy range of the matrix. The recoils of interest lie below the scattered beam ridge (indicated as the **black** region). Therefore, a two-dimensional E_{DSSSD}-ToF gate can be set to select the good fusion recoils for further analysis of the γ-ray data. The events not passing the recoil condition shown in Fig. 3.9 were not considered as good recoil events and were discarded from the further analysis. However, the good recoil events can not always be completely separated from the low-energy tail of the scattered beam. Therefore, a more stringent conditions on the energy and ToF can be applied for them to identify as recoil events clearly.

Recoils of interest might have both a well defined narrow time difference peak corresponding to the JUROGAM III time - DSSSD time and recoil energy from the DSSSD, E_{DSSSD}. This time difference corresponds to the difference between the formation of the recoil at the target (γ-ray emission) and the recoil detection at the MARA focal plane. A matrix showing the DSSSD time - JUROGAM III time versus E_{DSSSD} is shown in Fig. 3.10 (a). In addition, a matrix showing DSSSD time - JUROGAM III time difference as a function
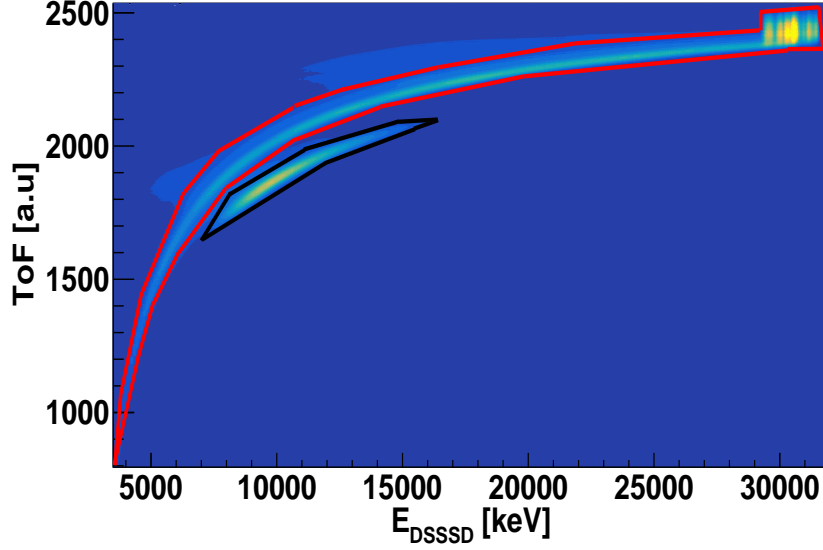
Figure 3.9: Fusion-evaporation residue identification matrix in the ^{28}Si(^{58}Ni,xαypzn) reaction using the E$_{\text{DSSSD}}$ - ToF method. The energy of the recoil in the DSSSD is measured from the x side of the detector. The **black** region indicate the group of events regarded as recoils and the **red** region indicates the scattered beam or beam like particles.The y-axis is the time-of-flight (ToF) measured between the gas counter and DSSSD (see section 3.3 for details).

of ToF, shown in Fig. 3.10 (b), can be used in combination with the matrix above for recoil selection.

The prompt γ rays can be associated with the good recoil events if the gates marked with **black** in Figs. 3.9 and 3.10 are passed. Further, recoil-decay correlations can be performed by setting additional conditions on the subsequent DSSSD decay events (see section 3.7). The decay events, such as conversion electrons, α and β decays are selected by appropriate gating conditions on time and energy and require anti-coincidence with the MWPC.

3.5 γ decay

An excited atomic nucleus may de-excite via emitting γ rays, with varying decay probabilities that are determined by the properties of the initial and final states. By taking into account the principles of energy and momentum conservation, the energy difference between the initial and final state is given by

$$\Delta E = E_\gamma + E_R, \tag{3.15}$$

where E_γ is the energy of the γ ray emitted. The kinetic energy of the recoiling nucleus (E_R) after de-excitation given by

$$E_R = \frac{E_\gamma^2}{2Mc^2}, \tag{3.16}$$
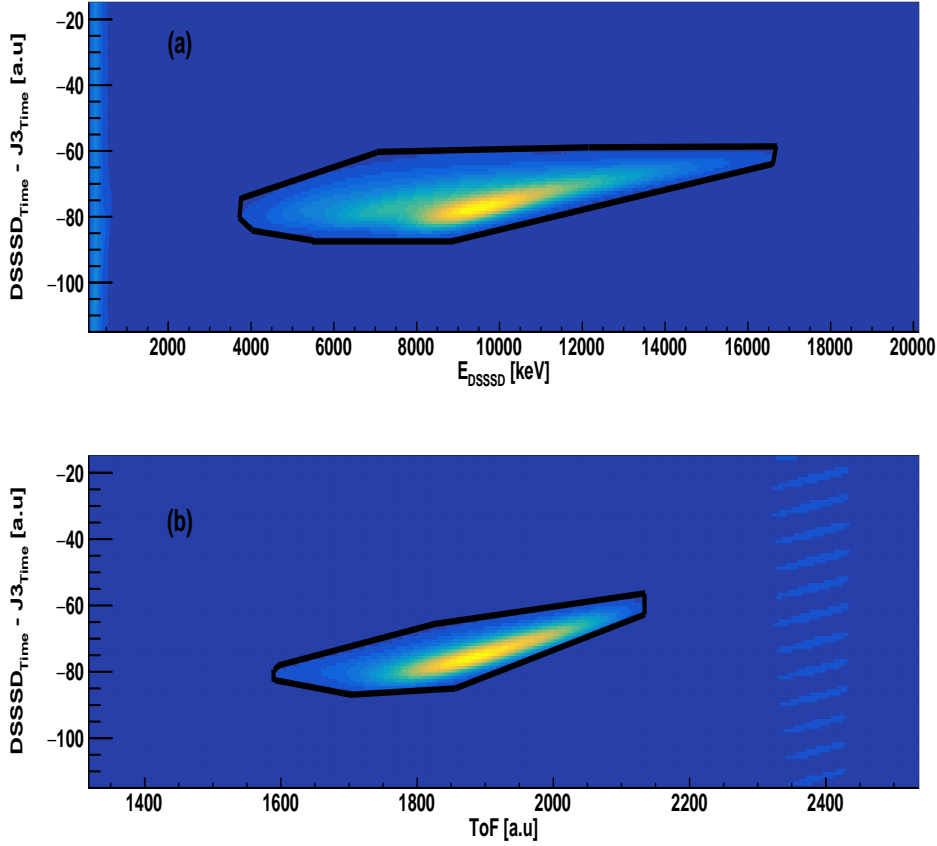
Figure 3.10: Fusion-evaporation residue identification matrix in the ^{28}Si(^{58}Ni,xαypzn) reaction (a) recoil energy in the DSSSD against DSSSD time - JUROGAM III time (DSSSD$_{time}$ - J3$_{time}$), (b) time-of-flight (ToF) against DSSSD time - JUROGAM III time (DSSSD$_{time}$ - J3$_{time}$).

where M is the mass of the nucleus. The contribution from Eq. 3.16 is negligible and, in practice, it does not need to be considered. The observed γ rays are detected at discrete energies and provide information about the structure of the nucleus. In addition, the angular distribution of γ rays and lifetime measurements can provide further, more detailed information about the nuclear structure.

For a γ decay event between an initial state, I_i^π and a final state I_f^π, the spin (I) and parity (π) are conserved. The photon carries away angular momentum of magnitude given by a quantum number L, called the multipolarity, which can have an integer value greater than zero. Multipolarity is defined as

$$|I_i - I_f| \leq L \leq |I_i + I_f|. \tag{3.17}$$

The $\Delta\pi$ of the γ-ray transition is determined by its character, either magnetic multipole (Ml) or electric multipole (El), given by

$$\pi_\gamma(Ml) = (-1)^{l-1}, \tag{3.18}$$

$$\pi_\gamma(El) = (-1)^l. \tag{3.19}$$

If a change in π exists between I_i^π and I_f^π, the γ-ray transitions can have a combination of odd electric and even magnetic multipoles. Occasionally, the γ rays can have a pure multipolarity, such as a $2^+ \longrightarrow 0^+$ transition, which has a pure $E2$ character. However, in most cases, the γ-ray transitions have mixed characters. The lowest allowed multipolarity typically dominates because the decay probabilities decrease quickly with increasing values of L. However, the decay probability of an electric radiation is approximately 10^2 times larger than than that of a magnetic radiation of the same multipolarity [59]. The γ-ray transition selection rules are summarized in the Table 3.3 below. Transitions are not allowed with $L = 0$ via a single γ-ray transition.

Table 3.3: The γ-ray selection rules and multipolarities.

L	Multipolarity	Transition type	Parity change
1	Dipole	Electric dipole ($E1$)	Yes
		Magnetic dipole ($M1$)	No
2	Quadrupole	Electric quadrupole($E2$)	No
		Magnetic quadrupole ($M2$)	Yes
3	Octupole	Electric octupole ($E3$)	Yes
		Magnetic octupole ($M3$)	No
L	2^L - pole	Electric 2^L - pole	No for even L
			Yes for odd L
		Magnetic 2^L - pole	Yes for even L
			No for odd L

3.5.1 Angular distributions

The emission angle of a γ ray relative to the nuclear spin orientation follows a characteristic probability distribution depending on the multipolarity (L). Therefore, measuring the angular distribution of γ rays provides information of the multipolarity of a given transitions. However, due to the insufficient statistics in the γ-ray spectroscopy experiments close to the proton-drip line, conclusive angular distribution information is exceedingly difficult to obtain. In fusion-evaporation reactions involving heavy ions, the angular momentum vectors of the products that result from the fusion and subsequent evaporation processes tend to become polarized and distributed closely to the plane that is perpendicular to the direction of the beam. The angular distribution [59] can be obtained from

$$W(\theta) = \alpha_0 + \alpha_2 cos^2\theta + \alpha_4 cos^4\theta + ... + \alpha_{2L} cos^{2L}\theta, \qquad (3.20)$$

where θ is the angle between the direction in which the γ rays were emitted and the beam axis, and α_n are the attenuation coefficients of the spin alignment, which are listed in Table IIa and IIb in Ref. [60]. The JUROGAM III array has detectors distributed in four rings relative to the beam direction. This enabled the study of how the intensity of a particular γ-ray transition was distributed over the different rings. When the statistics are low, like in the experiments presented in this thesis, an approximate method is used to obtain an angular distribution. The method used here is called the directional correlations of oriented

states (R_{DCO}) [59]. The emission of γ rays from excited nuclei depend on the orientation of the nucleus and the multipole matrix element of the initial and final states. Therefore, γ rays with different multipolarity will have different R_{DCO} values. The R_{DCO} values were obtained from three different γ-γ matrices ($(133.6° + 157.6°)$ vs (all angles), $(104.5°)$ vs (all angles), and $(75.5°)$ vs (all angles)). The same energy gate was set on the "all angles" -axis in each matrix, and the resulting three coincidence spectra represent the intensity of a γ-ray under investigation at different detection angles. The extracted γ-ray intensity was then corrected with the detection efficiency of the rings in question. The R_{DCO} values were extracted from

$$R_{DCO} = \frac{I_\gamma(133.6° + 157.6°)}{I_\gamma(104.5°)}, \quad R_{DCO} = \frac{I_\gamma(133.6° + 157.6°)}{I_\gamma(75.5°)}. \tag{3.21}$$

The two R_{DCO} values for each γ-ray transition were combined to provide the final R_{DCO} by weighted average. The methods described above were used to analyze transitions of known multipolarities originating from nuclei populated via other stronger reaction channels in the fusion-evaporation reaction, $^{40}Ca(^{32}S, x\alpha ypzn)$ and $^{40}Ca(^{40}Ca, x\alpha ypzn)$. The results showed that, on average R_{DCO} of 1.20(3) was obtained for $\Delta I = 2$, ($E2$) and 0.80(3) for $\Delta I = 1$ ($M1$ and $E1$) γ-ray transitions. It is important to mention that the values of the R_{DCO} ratio are highly influenced by the detection angles and experimental conditions. In addition, R_{DCO} ratios cannot be to used distinguish between either pure $\Delta I = 0$ dipole and stretched $E2$ transitions or stretched dipole and unstretched/mixed $E2$ transitions.

3.6 β decay

β decay describes three nuclear decay processes in which nuclei transmute towards the valley of stability without changing the mass number, A. The process of transmutation happens when a single nucleon (either a proton or neutron) is transformed into a nucleon of the other type or when a proton in the nucleus captures an atomic electron. The conservation of charge and lepton number requires the involvement of different particles in the β-decay processes. When a neutron is converted into a proton, an electron and an electron antineutrino ($\overline{\nu}_e$) are emitted, referred to as β^--decay, described as

$$n \longrightarrow p + e^- + \overline{\nu}_e. \tag{3.22}$$

Whereas the decay process

$$p \longrightarrow n + e^+ + \nu_e, \tag{3.23}$$

is referred to as β^+-decay. A positron and electron neutrino, ν_e are emitted in this process. In addition, the electron capture process is defined by

$$p + e^- \longrightarrow n + \nu_e. \tag{3.24}$$

When the continuous energy distribution of β particles was discovered, it was concerning because the other forms of radiation, such as γ and α, were observed to have discrete energies [61]. This phenomenon is caused by a pair of leptons that are emitted during the decay process and share the available energy. Thus, the energy of the emitted β^-/β^+ particle ranges from zero up to the total accessible amount of energy or to the "end-point" energy, given by the decay Q-value for example for β^+ decay

$$Q_{\beta^+} = [M_P - M_D - 2m_e]c^2. \tag{3.25}$$

Equation 3.25 involves the electron mass denoted by m_e and the atomic masses of the parent and daughter nuclei, represented by M_P and M_D, respectively. Within the scope of this thesis, the expression 'β-decay' pertains specifically to the process of β^+-decay.

3.6.1 β-decay selection rules

The conservation law of angular momentum determines how spin I and parity change when a nucleus undergoes a β-decay process. Consider the angular momentum of the initial state denoted J_i and the angular momentum of the final state denoted J_f. The angular momentum difference between the initial state and the final state must be equal to the total angular momentum of the lepton pair involved in the decay process. If the lepton pair, each with intrinsic half-integer spin, couples with anti-parallel spins, the following relation must hold

$$\mathbf{J_i} = \mathbf{J_f} + \mathbf{L}, \tag{3.26}$$

where L is the orbital angular momentum carried by the lepton pair. Eq. 3.26 describes the 'Fermi' transition. On the other hand, when the lepton pair couple with parallel spins, also known as 'Gamow-Teller' transition, the associated orbital angular momentum of the pair is indicated by L,

$$\mathbf{J_i} = \mathbf{J_f} + \mathbf{L} + \mathbf{1}. \tag{3.27}$$

Super-allowed β-decay transitions are a type of β-decay where the matrix element between the initial and final nuclear states is nearly equal to one. This is due to the wavefunctions of the initial and final states being very similar, allowing for a high probability of decay. For an allowed β-decay event, the lepton pair carries zero orbital angular momentum with no parity change (the parity associated with L is given by $(-1)^L$). The forbidden β decays are however, less likely to occur than the allowed β decays. Therefore, the most considerable β-decay rates are for the processes with $L = 0$. The decay processes with $L = 1$, $L = 2$, and $L = 3$ are possible, but with rapidly decreasing probabilities or increasing β-decay half-lives. β decays where the lepton pair carry orbital angular momenta $L = 1, 2, 3...$ are referred to as first, second, and third forbidden transitions. Table 3.4 shows the different types of β transitions, L, and parity change for the Fermi and Gamow-Teller transitions.

Table 3.4: Selection rules for various β-decay types. Parentheses indicate those which are not possible if either the initial or the final state spin is zero. The "yes" or "no" in the parity change column indicates whether the parity changes from the initial to the final state after the β-decay.

Transition type	L	Fermi		Gamow-Teller	
		ΔI	$\Delta \pi$	ΔI	$\Delta \pi$
Allowed	0	0	No	(0),1	No
First-forbidden	1	(0),1	Yes	0,1,2	Yes
Second-forbidden	2	(1),2	No	2,3	No
Third-forbidden	3	(2),3	Yes	3,4	Yes
Fourth-forbidden	4	(3),4	No	4,5	No

3.7 Recoil-β tagging and recoil-double-β tagging

The use of a recoil separator allows a recoil-decay correlation technique to be employed. A specific fusion-evaporation reaction product can be identified at the focal plane of a recoil separator based on its radioactive decay characteristics. This method allows to link for example the prompt γ rays to the source of the radiation, to the recoil. Generally this technique is known as the recoil-decay tagging (RDT) method. The correlations between implantation events and subsequent decays at the focal plane are performed by requiring temporal and spatial correlation conditions. In the case of heavy nuclei, recoil-decay tagging has been carried out by employing the characteristic α-decay properties, i.e., the decay half-life and discrete α-decay energy [62–64]. The β-decaying nuclei are more complicated in the sense of the decay correlations because of the continuous Fermi–Kurie distribution of electron (positron) energies. The β-decaying nuclei are generally also long lived in contrast to the half-lives of α and proton decaying nuclei located near the proton-drip line. This further complicates the successful correlation of a β-decay event with its corresponding implantation event. However, a specific type of decay process called the Fermi super-allowed β decay has characteristics that make it highly suitable for recoil-decay tagging. This β decay process has been discussed in detail in a previous work by Wilkinson *et al.*, [65]. In such cases the nuclei have relatively short half-lives (≤ 100 ms) with correspondingly high β-endpoint energies of up to 10 MeV. The use of β-decay as a tag to examine the structure of excited states, titled recoil-β tagging (RBT) [66], was developed about a decade ago at the University of Jyväskylä in collaboration with the University of York. This method has been successfully applied to study the structures of super-allowed β-decaying nuclei around the $N = Z$ region [7–10,12,66]. In this work, the (high-energy) β particles were identified by detecting coincidences between the DSSSD and the TUIKE detectors. As the DSSSDs are usually thin, i.e., between 300 - 700-μm thick, the β particles pass through the silicon and lose only a fraction of their energy (ΔE) as they interact with the detector material. For the experiments presented in this thesis, 300- and 700-μm thick DSSSDs were used. The energy loss of 10-MeV β particles in the 700-μm thick DSSSD is approximately 250 keV (approximately 125 keV in a 300-μm thick DSSSD), and the energy loss of the emitted β particles in the DSSSD is roughly constant due to their high kinetic energy. After passing through the DSSSD, the high-energy β particles deposit remainder of their energy in the TUIKE detector (E). To obtain
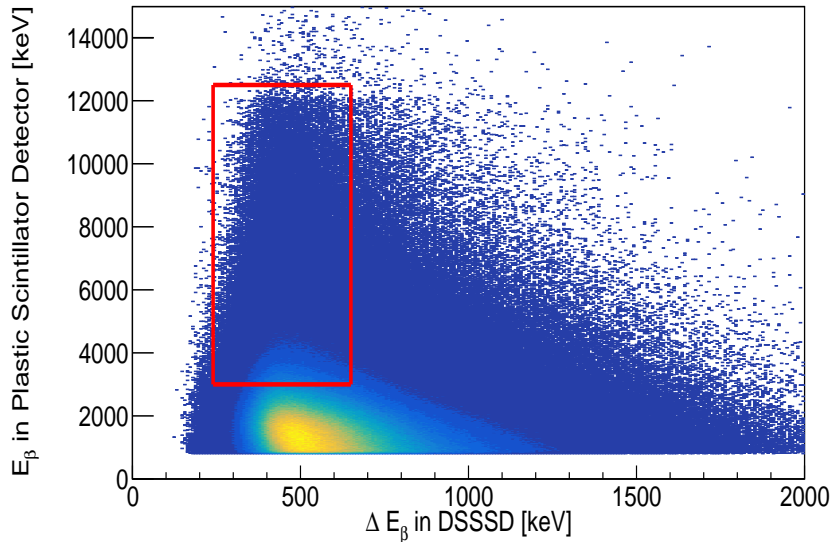
Figure 3.11: ΔE_β - E_β identification matrix for high-energy β particles. The energy-loss informa-tion (ΔE_β) is obtained from the DSSSD (the ΔE_β is the sum of the energy from the x and y strips of the DSSSD) and the full energy information (E_β) from the TUIKE detector. A two-dimensional energy gate shown in **red** can be applied to select the β particles to be correlated with the recoils within the desired correlation time. The low-energy threshold can be varied to achieve better statistics or cleanliness of the tagged prompt γ-ray spectra. The data is from a 700-μm thick DSSSD used in the fusion-evaporation reaction ^{40}Ca(^{32}S,xαypzn).

a visual representation of the observed distribution of β particles, a practical approach is to create a ΔE - E matrix, as demonstrated in Fig. 3.11. To select the β particles that are correlated with the recoils, a two-dimensional energy gate is set around the desired region of the distribution. The gate limits for ΔE_β are typically kept constant (since the energy loss is constant), while the lower limit for E_β can be varied to optimize the analysis for either maximum statistics or improved cleanliness of the tagged γ spectra. This provides a practical method for analyzing the data and identifying the desired correlations between the β particles and the recoils.

It is essential to have the correct correlations between the recoil implants and their sub-sequent β decays in order to keep the contamination, resulting from the false/random correlations, in the tagged γ-ray spectrum at a minimum level. Such correlations use also the decay search time (the time interval between the implantation of recoils and their subsequent β decays) to identify the recoils that produce the fast and high-energy β decay events. Spatial correlation between the position of the recoil and the β-decay is non-trivial due to the extended interaction range of β-particles in the silicon detector. The best estimate is to use a "single pixel" correlation search strategy, where the decay event is detected in the same DSSSD pixel as the preceding implant. Therefore, each β decay is 'paired' with the most recent recoil event that has occurred in the same pixel.

In order to take into an account the possibility of the β particle escaping to a neighbouring pixel, the so called "nearest neighbour star" -tagging strategy can also be used (see Fig. 3.12 (b)). Here, the recoil-decay correlations are searched also from the four nearest pixels
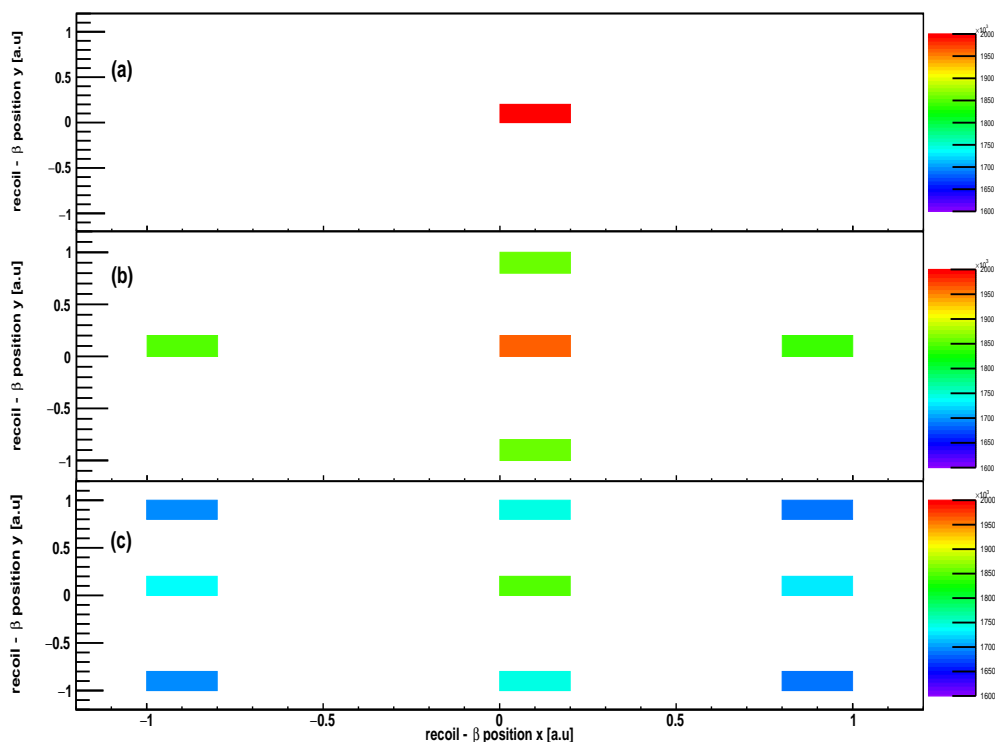
Figure 3.12: The position difference in the DSSSD between a recoil implant and a β-decay event in a) single pixel, b) nearest star and c) square correlation strategies.

in addition to the pixel the recoil was implanted to. The five pixels form a star shape, hence the name of "nearest neighbour star". In addition, it is possible to search for the correlations from the eight nearest pixels and the pixel in which the recoil implant event occurred, thus creating a square shape, as shown in Fig. 3.12 (c). Figure 3.13 (a) shows the number of events for the tagged 403-keV γ ray from ^{70}Br for different recoil-β tagging strategies as a function of the lower E_β limit. Including the four most immediate neighbor pixels increases the number of correlated events by a factor of 2, with the additional four neighboring pixels increasing the number of the correlated events by a factor of 3 for E_β greater than 1.5 MeV. At a relatively high β energy threshold, the number of correlated events for the nuclei of interest is nearly the same between 4 and 8 neighbouring pixels, but approximately 50 % (at β-energy threshold of 4 MeV) more in comparison to the single pixel strategy as shown in Fig. 3.13 (a). Figure 3.13 (b) shows the ratio of the 403-keV γ ray from ^{70}Br over 442-keV γ ray from a long-lived contaminant ^{69}As as function of the β-energy threshold compared among different recoil-β tagging strategies. With a low-energy β gate, the ratio of the contaminant to the nuclei of interest for the single pixel strategy is better than in the other two methods. However, the cleanest of the spectrum comes at a cost, as the statistics reduce in comparison to the other two methods.

The recoil implantation rate in the DSSSD in the reactions used in this work leads to an average 'per-pixel' implantation rate of 1.36 per second, considering that approximately 80 % of the available 13824 pixels are being hit by the recoils (the recoil implantation rate was around 15 kHz). This translates to an average of 0.74-s time difference between the consecutive recoil hits, which is about 3 - 10 times longer than the typical search time used
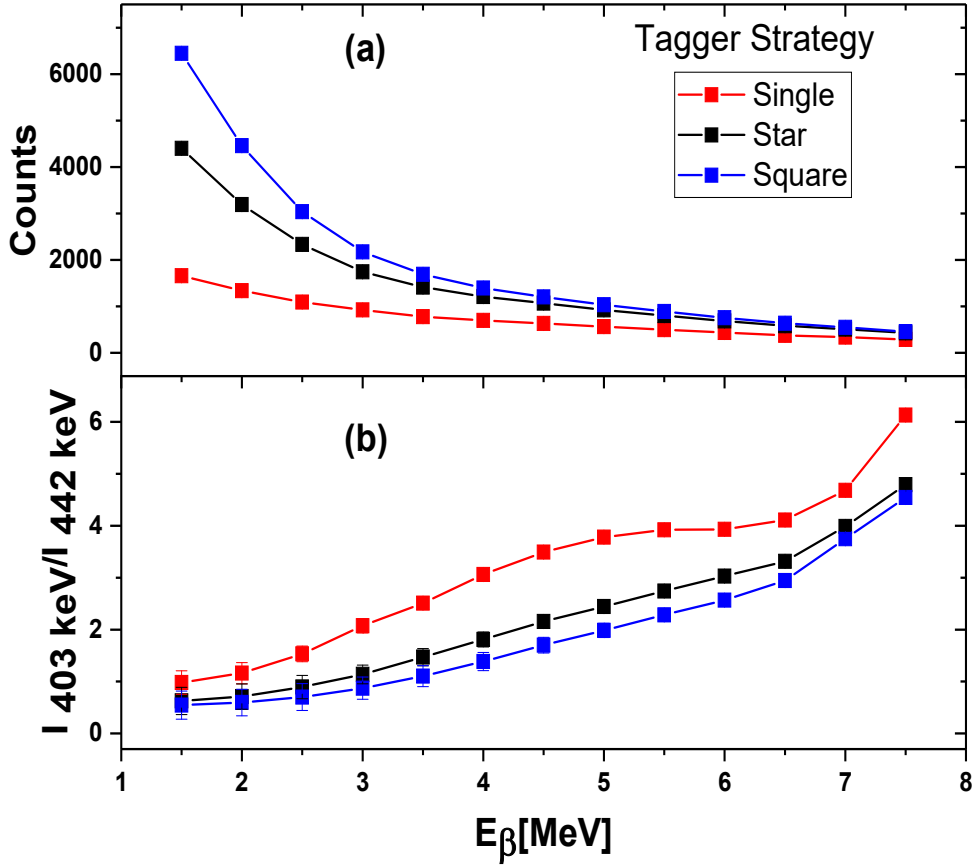
Figure 3.13: (a) Number of correlated events for the 403-keV γ ray from ^{70}Br for different tagging strategies as a function of β-energy threshold and (b) ratio of the number of events for the 403-keV γ ray from ^{70}Br over 442-keV γ ray from a long-lived contaminant ^{69}As as function of the β-energy threshold compared among different recoil-β tagging strategies. The x-axis, E_β shows the lower β-energy threshold.

for a fast β emitter. However, there is still a non-zero probability of a random implant event occurring in the middle of a genuine recoil-β pair. Therefore, increasing the spatial correlation area in the star or square tagging strategies increases the probability of random correlations as demonstrated in Fig. 3.13 (b). In addition, the total amount of recoils is very high when compared to the yield of nucleus of interest. Therefore the possibility of false recoil-β correlation is a constant nuisance in the RBT method.

In certain cases, the β-decay properties of the both parent and daughter nuclei are suitable for the recoil-β correlation method to be employed. The method of tagging prompt γ rays with two subsequent fast β decays following the recoil implantation is called the recoil-double-β tagging (RDBT). The RDBT method was successfully applied for the first time in the $A = 62$ triplet study [67]. It should be noted that the spectroscopic studies of the $N = Z$ nuclei become increasingly difficult with increasing mass number as the $N = Z$ line gets closer to the proton-drip line and the reaction cross sections, especially for the $T_z = -1$ nuclei reduce. Figure 3.14 shows the β-decay chain of ^{70}Kr ($T_{1/2} = 30$ ms, $Q_{EC} \approx 10$ MeV [68]) decaying to ^{70}Br ($T_{1/2} = 79$ ms, $Q_{EC} \approx 10$ MeV [68]), which further decays to ^{70}Se ($T_{1/2} = 40$ min, $Q_{EC} \approx 2.4$ MeV [68]). For this kind of a β-decay

chain (two fast β decays with high endpoint energies), it is possible to apply the RDBT method to tag the γ rays originating from the exotic ^{70}Kr nucleus.
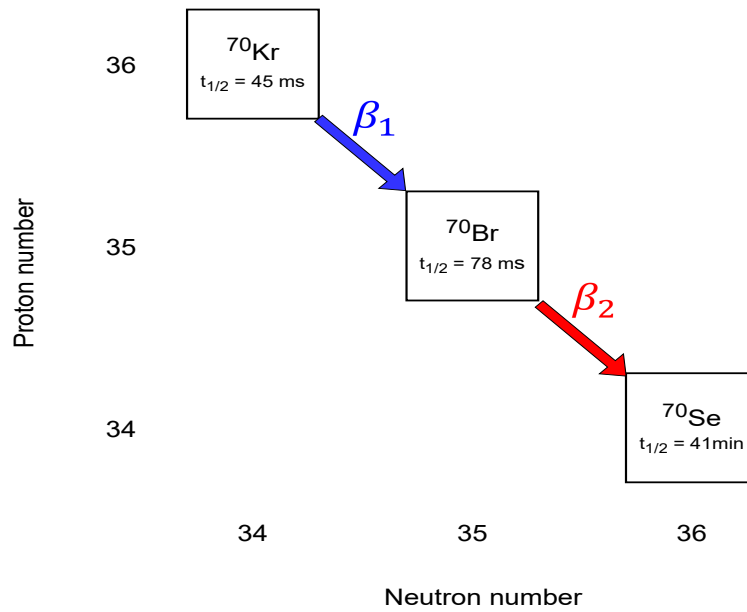
Figure 3.14: The β-decay chain from ^{70}Kr to ^{70}Se illustrating two fast consecutive β decays. These type of β-decay chains allow the use of recoil double-β tagging method to tag prompt γ rays originating from the exotic $T_z = $ -1 nuclei such as ^{70}Kr [68].

Finally, one must consider the β decay lifetimes. While using the RBT or RDBT technique, shorter decay time correlations are advantageous as one can maximize the likelihood that a recoil-β correlation chain is the result of the recoil of interest rather than a false correlation due to a contaminant reaction products. For nuclei with relatively long β-decay half-lives, such as ^{84}Mo ($t_{1/2} = 2.3$ seconds), longer correlation times are necessary to maximize statistics, which potentially results in higher false correlations and makes the RBT method impractical. Figure 3.15 summarises the experimental equipment and methods used in the current thesis. Top of the figure illustrates the different steps of the fusion evaporation reaction with a rough time scale. The fusion evaporation steps up to t$\sim$$10^{-9}$ s takes place within the JUROGAM III target chamber.

Figure 3.15: The experimental setup used in the present study showing the JUROGAM III array, and MARA separator.

4 SPECTROSCOPY OF MOLYBDENUM 84

This chapter presents the experiment aimed for confirming the $J^\pi > 6^+$ states in the even-even ^{84}Mo. The first section describes the used fusion-evaporation reactions to study ^{84}Mo and the reaction cross-section determination of the 2n channel in the ^{28}Si(^{58}Ni,xαypzn) reaction. Section 4.2 presents the used background subtraction methods and finally the results from these experiments. Section 4.3 describes the nuclear physics of interest for the even-even $N = Z$ nuclei in the $A = 60$-88 mass region. The even-even $N = Z$ nuclei below ^{100}Sn are expected to exhibit complex structural properties, such as shape evolution and the isovector and controversial isotensor neutron-proton pairing correlations.

4.1 Reaction cross-section measurements

Despite the experimental efforts made over the years, progress in the experimental investigation of heavy ($A > 60$), $N = Z$ nuclei especially at high angular momentum has been challenging. This is because of the low production yields of these nuclei in fusion-evaporation reactions, which is the best method to probe the nuclear structure in the high spin regime. Nuclei in this region have also been produced by the projectile fragmentation of intermediate to high-energy heavy-ion beams, but the population of excited states is more selective and precision γ-ray spectroscopy is difficult due to the high velocities of the products.

For the fusion-evaporation reactions, it is of highest importance to explore the cross-section maximum in terms of the beam energy for a given beam-target combination to maximize the yield for the nucleus of interest. The choice on the beam-target combination depends strongly on the available accelerator, the mass separation capabilities, and reaction channel selection possibilities. Therefore, an optimization of these parameters (beam, beam energy, and target) is needed to produce these nuclei with the highest possible yield. Some aid in the process can be achieved from different reaction simulation codes, some of them being

analytical based[5], others being of the Monte-Carlo type[6]. Commonly used cross-section calculators are PACE4 [38], CASCADE [69], HIVAP [70], POTFUS + ABLA called CNABLA [71, 72], and POTFUS + GEMINI++ [72]. In the current work, only the PACE4 code was used, Ref. [73] provides a detailed comparison of calculated fusion-evaporation reaction cross sections from the five different codes mentioned above and compares these to the available experimental data.

Figure 4.1: Cross-section [mb] as a function of excitation energy [MeV] for the fusion-evaporation reactions (a) ^{28}Si(^{58}Ni,xαypzn), (b) ^{54}Fe(^{32}S,αypzn), and (c) ^{46}Ti(^{40}Ca,xαypzn). E_3^* is the excitation energy at the entrance of the target, E_2^* is the excitation energy at the center of the target, and E_1^* is the excitation energy at the back of the target at beam energies of (a) 201 MeV, (b) 107 MeV and (c) 124 MeV. E_{CB}^* is the excitation energy at the Coulomb barrier of the three different reactions.

Figure 4.1 shows the cross sections obtained from PACE4 for three different reactions aimed for production of ^{84}Mo. However, whether the compound nuclei are formed at the target's entrance, back, or center is unclear. To address this issue, Fig. 4.1 shows also the PACE4 calculated cross sections at the entrance (E_3^*), center (E_2^*), and back (E_1^*) of the

---

5   Analytical based code include CASCADE and HIVAP.
6   Monte-Carlo based code include PACE4, CNABLA, and POTFUS+GEMINI++.

target. The **green** line in Fig. 4.1 represents the excitation energy at the Coulomb barrier (E^*_{CB}). In Figs. 4.1 (a) and (b), the cross-section decreases slowly at higher energies but exhibit a sharp decline at lower energies due to the Coulomb repulsion. However, in the ^{40}Ca + ^{46}Ti reaction, shown in Fig. 4.1 (c), the closeness of the Coulomb barrier to the used beam energy is causing a clear drop in the expected yields for the two-particle evaporation channels. Conversely, for the ^{32}S + ^{54}Fe reaction shown in Fig. 4.1 (b), slightly reducing the used beam energy would have slightly improved the yield for the 2n channel. Finally, Fig. 4.1 (a) indicates that the beam energy used in the ^{58}Ni + ^{28}Si reaction was optimal.

Previous in-beam γ-ray spectroscopy experiments on ^{84}Mo were performed using the fusion-evaporation reaction ,^{28}Si(^{58}Ni,2n)^{84}Mo [74–76]. In addition to this reaction, two other reactions were investigated in the present work, as listed in the Table 3.1., to study the production rate of ^{84}Mo. As discussed above, the reaction cross sections can be predicted by using, e.g., the PACE4 calculations, but the obtained values are known to be off especially for the two-neutron (2n) evaporation channels [73]. The second factor affecting the observed production rate for a given nucleus between the different possible reactions is the MARA transmission efficiency, which is highly reaction dependent. This means, that there are two unknown variables, the reaction cross-section and the separator transmission efficiency, which have an effect on the experimental yield.

In this work, the direct experimental determination of the absolute MARA transmission efficiency was not possible. However, an estimate for the MARA transmission efficiency for a given reaction can be obtained from an ion optical simulation. Using this information it is possible to try to benchmark the theoretical cross-section predictions obtained from PACE4 (alternatively, the simulated transmission efficiencies can be benchmarked against the calculated cross sections). For this purpose, the production of ^{84}Zr, two proton (2p) evaporation channel was investigated in the three different reactions owing to its relatively high cross section. It was assumed that the intensity of the 540-keV, $2^+ \longrightarrow 0^+$ γ-ray transition reflects the total production yield of ^{84}Zr. The relative cross sections for ^{84}Zr in the different reactions may be derived using Eq. 3.7 after correcting for γ-ray detection efficiency, JYU-Tube detector efficiency, and the variation in the transmission efficiency of the MARA recoil separator. It is worth noting that the value of the transition efficiency of the separator used in the cross-section estimates was for the so-called reference particle ($\sim$30%, $\sim$12%, and $\sim$20% for the ^{58}Ni, ^{32}S, and ^{40}Ca beams [77], respectively) which in this case was ^{84}Mo. The ion designated as the reference particle moves through the separator along the optical axis. The separator's configuration is adjusted so that the reference particle has zero spatial and chromatic coordinates. Table 4.1 shows the semi-experimentally determined cross sections for the 2p channel from the different fusion-evaporation reactions and compares these to the PACE4 predictions.

Table 4.1: Experimental and PACE4 cross sections for the 2p channel in the investigated reactions.

Nuclei	Experimental calculated cross-section [mb]			PACE4 Calculated cross-section [mb]		
	^{28}Si(^{58}Ni,2p)	^{54}Fe(^{32}S,2p)	^{46}Ti(^{40}Ca,2p)	^{28}Si(^{58}Ni,2p)	^{54}Fe(^{32}S,2p)	^{46}Ti(^{40}Ca,2p)
^{84}Zr	3.0	4.0	0.5	23.6	9.0	2.2

It is worth noting that the cross-section values for the 2p channel in Table 4.1 using Eq. 3.7

were determined using data collected from experiments where MARA was set to pass $A =$ 84 recoils through the separator mass slits. The values calculated using Eq. 3.7 suggest that PACE4 overestimates the cross sections. It is relevant to note that Ref. [73] reached the same conclusion. The PACE4 calculated cross-section values for the 2n and 2p channels in the ^{58}Ni + ^{28}Si reaction at 201 MeV are 0.583 mb and 23.6 mb, respectively. Thus the 2n channel is expected to be 2.5% of the 2p channel, giving a value of 0.074 mb for the 2n channel when compared to the semi-experimental cross-section of the 2p channel (using Eq. 3.7). In a previous study, it was found that the cross-section of ^{84}Mo in the ^{28}Si(^{58}Ni,2n) reaction was 0.007 mb, whereas the cross-section for the 2p channel was measured to be 35 mb [74]. Comparing the cross-section values from Ref. [74], PACE4 calculated values, and from this work, the values from Ref. [74] overestimated the cross-section for the 2p channel and underestimated the 2n channel. The search for the γ-ray transitions from the decay of excited states in ^{84}Mo will only use data from the ^{58}Ni + ^{28}Si reaction.

4.2 Results

The recoil gated prompt γ-ray spectra observed at the target position using the JUROGAM III Ge-array corresponding to the fusion-evaporation reactions (a) ^{46}Ti(^{40}Ca,xαypzn) at 124 MeV, (b) ^{54}Fe(^{32}S,αypzn) at 107 MeV, and (c) ^{28}Si(^{58}Ni,xαypzn) at 201 MeV are shown in Fig. 4.2. The main challenge of performing γ-γ coincidence analysis in the case of the even-even ^{84}Mo is caused by the low cross-section as discussed in the section 4.1. Therefore, a background subtraction procedure was developed to remove γ rays associated with charged-particle evaporation channels from the γ-γ matrix before searching for any coincident γ rays in ^{84}Mo.

The MARA separator has the ability to physically separate ions based on their mass-to-charge ratio $[M/Q]$. The dispersion at the focal plane for the MARA separator is 8 mm/($\Delta M/Q$), implying that a 1% change in the M/Q values will result in an 8 mm spatial separation. Ref. [43] demonstrates and discusses how MARA's electric and magnetic fields are optimized for transmitting a reference particle with defined energy, E_k, mass M_{ref}, and charge state Q_{ref} through the separator to the focal plane. The M/Q value of a recoiling particle at the focal plane is determined by

$$\frac{M}{Q} = \frac{M_{ref}}{Q_{ref}}(1 + \delta_m). \tag{4.1}$$

The relative difference in M/Q compared to the reference particle, denoted as δ_m, is calculated from the MWPC x position coordinates. Figure 4.3 shows the mass-to-charge distribution for the ^{28}Si(^{58}Ni,xαypzn) reaction with the reference charge state equal to 24.5e. Half-integer reference charge states are typically used to have the full charge states being symmetrically distributed around the focal point allowing the use of mass slits. The **red** lines represent the M/Q limits for the mass number 84, which were used to suppress
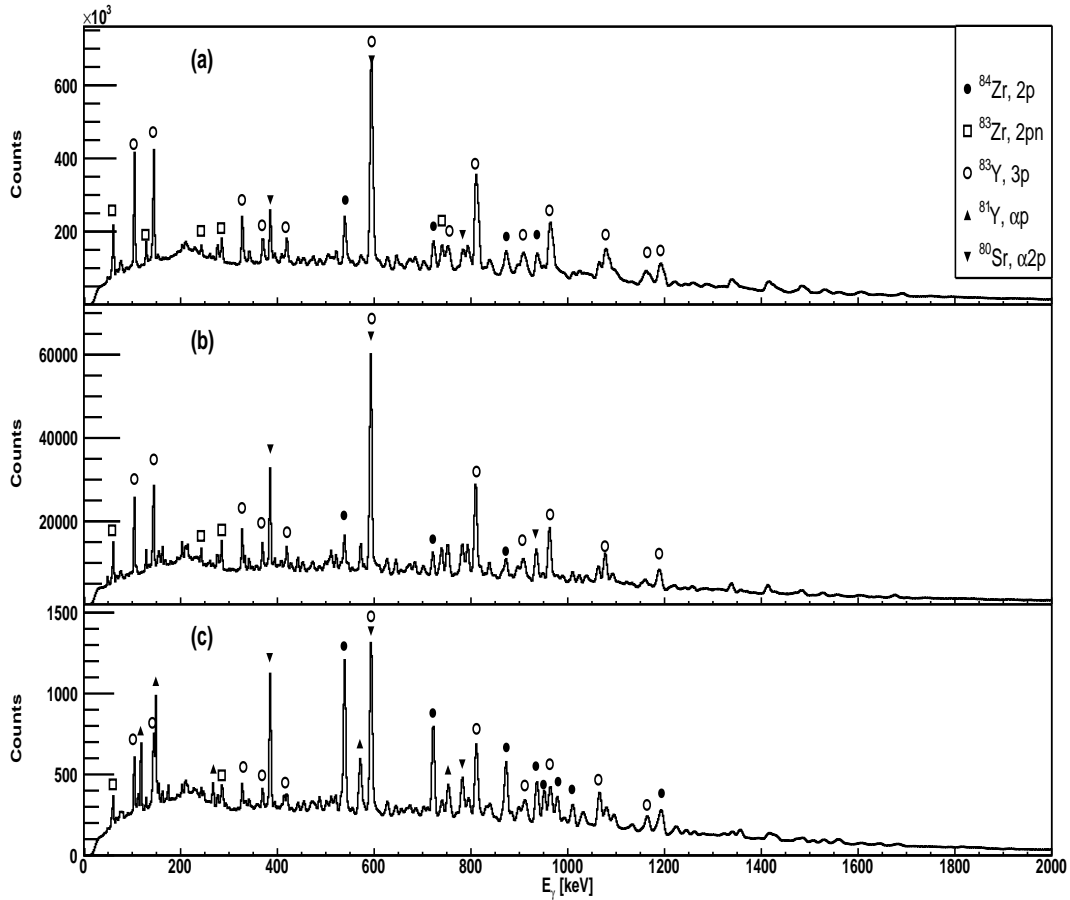
Figure 4.2: Recoil gated prompt singles γ-ray events detected by the JUROGAM III Ge-array from the fusion-evaporation reaction (a) ^{46}Ti(^{40}Ca,xαypzn) with a beam energy of 124 MeV, (b) ^{54}Fe(^{32}S,αypzn) with a beam energy of 107 MeV, and (c) ^{28}Si(^{58}Ni,xαypzn) with a beam energy of 201 MeV.

the other channels in the recoil-gated γ singles spectrum or in γ-γ matrix.

In this mass region 3 - 4 charge states can be collected at the MARA focal plane, depending on the mass and the reaction symmetry employed. To enhance the channel selection, MARA is equipped with adjustable metal sheets, slits, which can be moved into or out of the ion-optical path of the ions to act as physical barriers. In addition, the selected reference particle charge state will significantly influence the charge states collected at the MARA focal plane. Table 4.2 shows the calculated M/Q for different masses and charges. If the selected reference particle charge state was 21.5e for the ^{28}Si(^{58}Ni,2n)^{84}Mo reaction, mass 80 would directly overlap with mass 84. Hence, it essential to select the reference charge state so that the M/Q ratios for the nucleus of interest are well separated from those of the strong contaminating channels. However, any M/Q overlap is difficult to avoid as demonstrated in the Table 4.2. The reference particle charge state used for the ^{54}Fe(^{32}S,2n)^{84}Mo reaction was 16.5e, and therefore the two charge states collected at the focal plane were 16e and 17e as shown in Table 4.2. Table 4.2 shows that using 16.5e as the reference particle charge state, mass 79 overlaps with the mass of interest, $A = 84$. However, mass 79 is not observed in Fig. 4.2 (a) because of the low production cross-section. By contrast, ^{83}Y is strongly seen in the Fig. 4.2 (a) as the tails of the
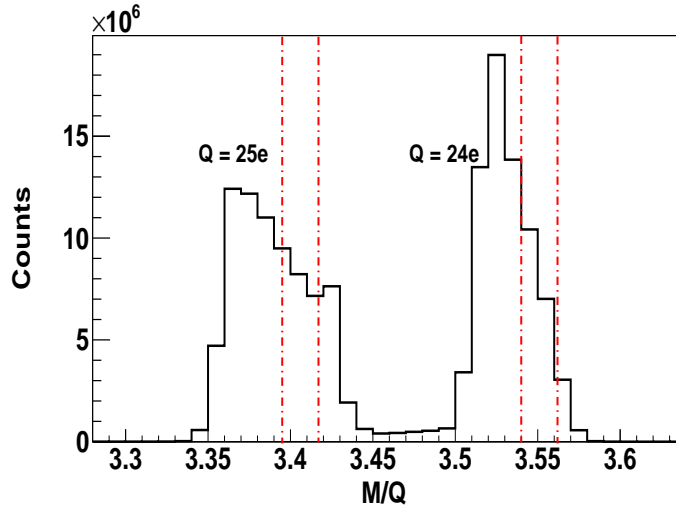
Figure 4.3: The mass-to-charge distributions reconstructed from the MARA focal plane detector information. The dashed **red** lines are the M/Q limits for $A = 84$, obtained from having a γ gate set on the 540-keV γ ray from ^{84}Zr.

(often orders of magnitude stronger) neighboring mass distributions (A-1) overlap with the mass of interest due to aberrations[7]. The reference particle charge state used for the ^{28}Si(^{58}Ni,2n)^{84}Mo reaction was 24.5e, and the two charge states collected at the focal plane were 24e and 25e. The masses 80 and 81 have relatively close M/Q ratios to those of the mass 84 in this reaction. In addition, mass 83 is again expected to leak through and contribute to the observed γ-ray spectra as shown in Fig. 4.2 (c).

In addition, the MWPC at the MARA focal plane offers additional suppression capabilities of contaminant channels produced in the reaction. Figure 4.4 shows the positions of various masses at the focal plane. A combination of the M/Q limits and two-dimensional gate on the phase space image constructed from information from the MWPC and DSSSD data provides a good mass selection for the current work. Additional details on the phase space recreation from the MARA focal plane can be found in Ref. [43] and references therein. The ability to detect the evaporated charged particles at the target position using the JYU-Tube detector can further be used to reduce contamination from charged-particle fusion-evaporation channels and enhanced the relative contribution of the 2n channel. However, the JYU-Tube detector efficiency is not 100%, as shown in Table 3.2.

The investigation of the transitions from ^{84}Mo is based on the well-known $2^+ \longrightarrow 0^+$ 444-keV γ ray [74–76]. However, it is essential to review this γ-ray energy for the possible source of contaminants. From previous studies using the fusion-evaporation reaction ^{28}Si(^{58}Ni,xαypzn) [74–76], two γ rays with energies of 445.1 and 444.4 keV from ^{82}Y and ^{83}Y could contaminate the γ gate set on the 444-keV γ ray. However, an examination of the recoil-gated prompt singles γ rays shown in Fig. 4.2 (a), shows that ^{82}Y is weakly populated in this reaction. Hence, the transitions from ^{82}Y are not a source of significant

---

7   *Aberrations*: The image blurring at the focal plane and the resulting degradation of the real mass resolving power in an ion-optical system are caused by the higher order matrix elements, which are referred to as aberrations.

Table 4.2: Calculated M/Q for different masses (M) and charge states (Q). The reference charge Q_{ref} used in the fusion-evaporation reaction ^{54}Fe(^{32}S,αypzn), ^{46}Ti(^{40}Ca,xαypzn), and ^{28}Si(^{58}Ni,xαypzn) were **16.5**, **18.5**, and **24.5**, respectively. The M/Q values in colour show potentially overlapping mass-to-charge ratios. The accepted overlap limit is ≤ 0.02 which translates to position difference of approximately 4-5mm between charge states.

M/Q	79	80	81	82	83	84
15	**5.27**	5.33	5.40	5.47	5.53	5.60
16	**4.94**	5.00	5.06	5.13	5.19	**5.25**
17	**4.65**	4.71	4.76	4.82	4.88	**4.94**
18	4.39	**4.44**	4.50	4.56	4.61	**4.67**
19	4.16	4.21	4.26	4.32	4.37	**4.42**
20	3.95	**4.00**	4.05	4.10	4.15	4.20
21	3.76	3.81	3.86	3.90	3.95	**4.00**
22	3.59	3.64	3.68	3.73	3.77	3.82
23	3.43	**3.48**	**3.52**	3.57	3.61	3.65
24	3.29	3.33	**3.38**	3.42	3.46	**3.50**
25	3.16	3.20	3.24	3.28	3.32	**3.36**
26	3.04	3.08	3.12	3.15	3.19	3.23
27	2.93	2.96	3.00	3.04	3.07	3.11
28	2.82	2.86	2.89	2.93	2.96	3.00

contamination in the present analysis. Conversely, ^{83}Y, which is very strongly populated in this reaction in comparison to ^{84}Mo, and has a γ ray with an energy of 444.4 keV, which is in coincidence with several γ rays in the energy domain of 500 – 900 keV, where the second yrast transition in ^{84}Mo is expected to be located.

Figure 4.5 (a) shows the projection of the recoil and M/Q-MWPC gated γ-γ matrix measured by the JUROGAM III from the ^{28}Si(^{58}Ni,xαypzn) reaction. Figure 4.5 (b) shows the identical histogram as Fig. 4.5 (a) but with zero charged particles detected in the JYU-Tube detector. It is observed that the M/Q-MWPC gate plus the charged-particle suppression using the JYU-Tube detector is insufficient to remove contributions from the charge-particle channels completely from the data. For this reason, an accurate subtraction of the charged-particle channels is of decisive importance. Therefore, a method was developed for the charged-particle channel subtraction in the recoil and M/Q-MWPC gated matrices.

The first step in producing a recoil and M/Q-MWPC gated γ-γ matrix with a relatively small number of γ events from charged-particle channels is to create two background matrices with different JYU-Tube detector conditions. The first background matrix, called Background 1, contains γ-γ events outside the recoil-γ time gate with zero charged particles detected in JYU-Tube. The second background matrix, called Background 2, contains γ-γ events outside the recoil-γ time gate with more than zero charged particles detected in JYU-Tube. In addition, two γ-γ matrices with γ events within the recoil-γ time gate and with two different JYU-Tube detector conditions, (i) recoil and M/Q-MWPC gated γ-γ matrix with JYU-Tube fold condition zero (called matrix tf0), (ii) recoil and
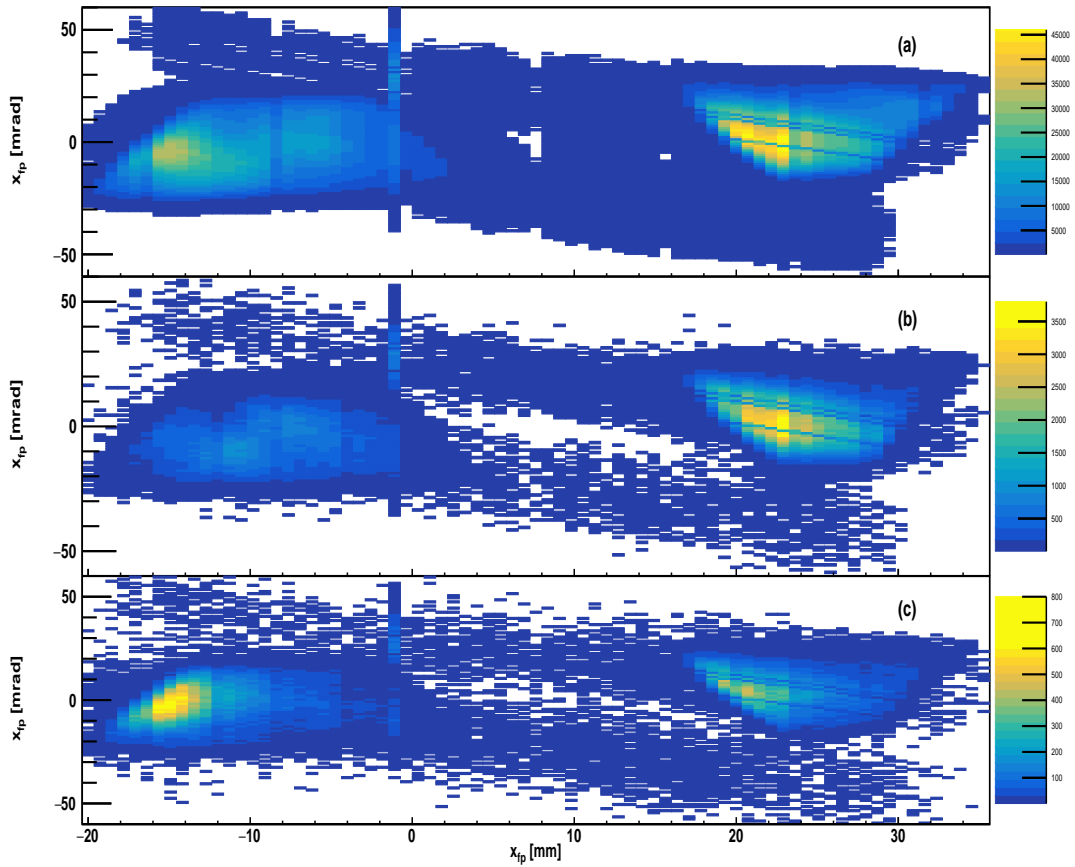
Figure 4.4: (a) Phase space distribution showing the collected masses at the MARA focal plane (b) mass 84 phase space distribution at the MARA focal plane made by gating on the 540-keV γ ray from ^{84}Zr and (c) mass 80 phase space distribution at the MARA focal plane made by gating on the 386 keV γ rays from ^{80}Sr.

M/Q-MWPC gated γ-γ matrix with JYU-Tube fold greater than zero (called matrix Gt0). The γ-γ matrices with JYU-Tube fold zero are in anticoincidence with charged-particle evaporation channels. The contribution from the charged-particle channels in these γ-γ matrices is reduced while the relative contribution of the 2n channel is enhanced. The matrices with the JYU-Tube detector condition greater than zero are naturally dominated by γ rays associated with the charged-particle channels.

The subsequent step is to subtract the γ-γ matrices from γ rays associated with the charged-particle channels (matrix tf0 - background 1 and matrix Gt0 - background 2), and call the resultant matrices background subtracted recoil and M/Q-MWPC gated γ-γ matrix JYU-Tube detector condition zero (background subtracted matrix tf0), and background subtracted recoil and M/Q-MWPC gated γ-γ matrix JYU-Tube detector condition greater than zero (background subtracted matrix Gt0). Figure 4.5 (c) shows the projection of the background subtracted matrix tf0. It is worth noting that the γ rays from the charged-particle channels still dominate this matrix.

The next step is to subtract the background subtracted matrix Gt0 from the background subtracted matrix tf0. The background subtracted matrix Gt0 was normalized with reference
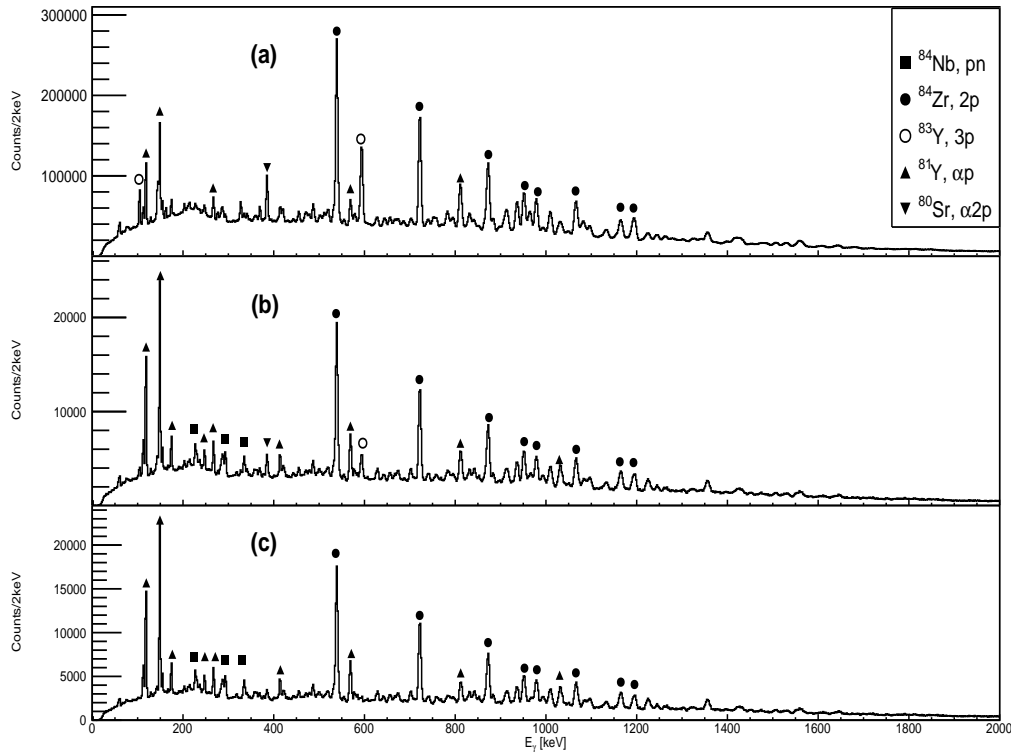
Figure 4.5: (a) Projection of the recoil and M/Q-MWPC gated γ-γ spectrum measured by the JUROGAM III Ge-array from the ^{28}Si(^{58}Ni,xαypzn) reaction, (b) same as (a) but with zero charged particles detected in the JYU-Tube detector, and (c) same as (b) but with prompt γ events outside the recoil-γ time gate subtracted as the background.

to the intensity of the 540-keV γ ray in the background subtracted matrix tf0. Then the normalised "background subtracted matrix Gt0" was subtracted from the "background subtracted tf0" -matrix. The resultant γ-γ matrix is relatively reduced of the charged-particle channel contributions. However, it is still shows γ rays associated with the charged-particle channels, as shown in Fig. 4.6 (b) in comparison to the original matrix shown in the Fig. 4.6 (a).

A γ gate set on the 444-keV γ ray ($2^+ \longrightarrow 0^+$) in ^{84}Mo using the recoil and M/Q-MWPC gated γ-γ matrix, with the projection shown in Fig. 4.6 (b), indicates that the charged-particle channels still dominate this matrix, as shown in Fig. 4.7 (a). However, the previously observed coincidences in ^{84}Mo are also observed in this gate, namely the γ rays at 673 keV ($4^+ \longrightarrow 2^+$ transition in ^{84}Mo) and 889 keV ($6^+ \longrightarrow 4^+$ transition in ^{84}Mo). It is challenging to confirm the coincidences with the γ-ray transitions at the energies of 1063 (the candidate $8^+ \longrightarrow 6^+$ transition in ^{84}Mo) and 1207 keV (the candidate $10^+ \longrightarrow 8^+$ transition in ^{84}Mo) from the gated spectrum with the γ gate set at 444 keV. Therefore, further background subtraction step was taken to reduce the charged-particle channel contribution in Fig. 4.7 (b).

Consider the 444-keV γ ray from ^{84}Mo in the charged-particle subtracted recoil and M/Q-MWPC gated γ-γ matrix with th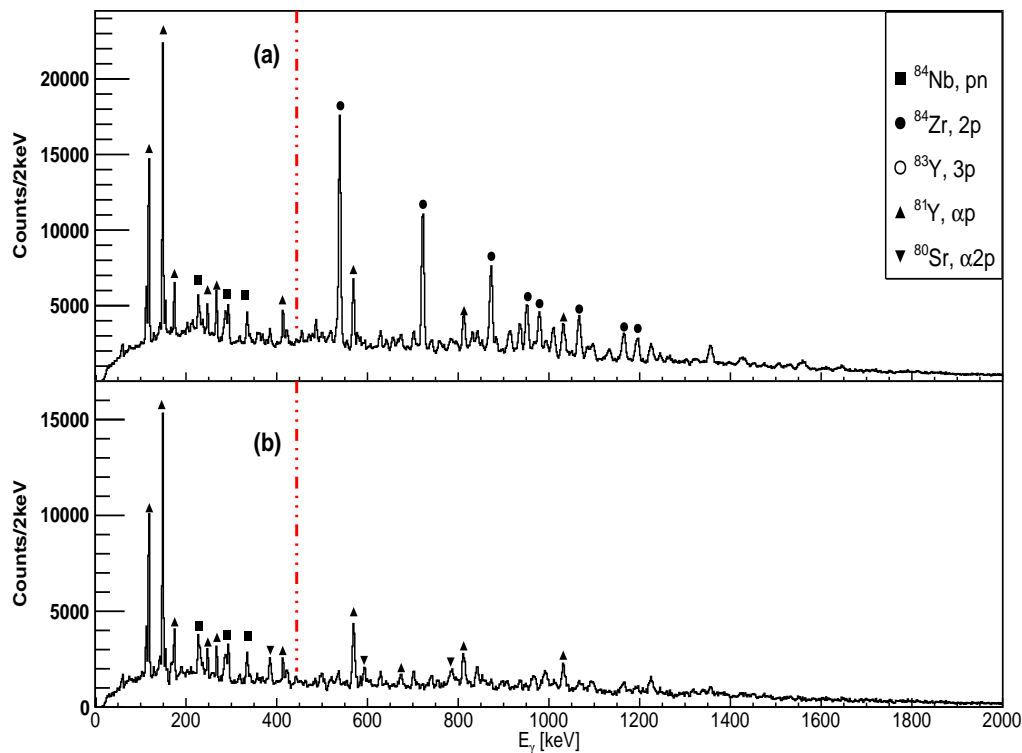e JYU-Tube detector fold condition zero (The matrix is created by subtracting the background subtracted matrix Gt0 from the background subtracted matrix tf0 as stated above). The spectrum generated by gating on this γ-ray in

Figure 4.6: Projection of the recoil and M/Q-MWPC gated γ-γ matrix measured by the JUROGAM III Ge-array from ^{28}Si(^{58}Ni,xαypzn) (a) with prompt γ events outside the recoil-γ time gate subtracted as the background, (b) the same as (a) but with normalized charged-particle γ-γ matrix subtracted as background. The **red** dashed lines show the position of the 444-keV γ ray ($2^+ \longrightarrow 0^+$) in ^{84}Mo.
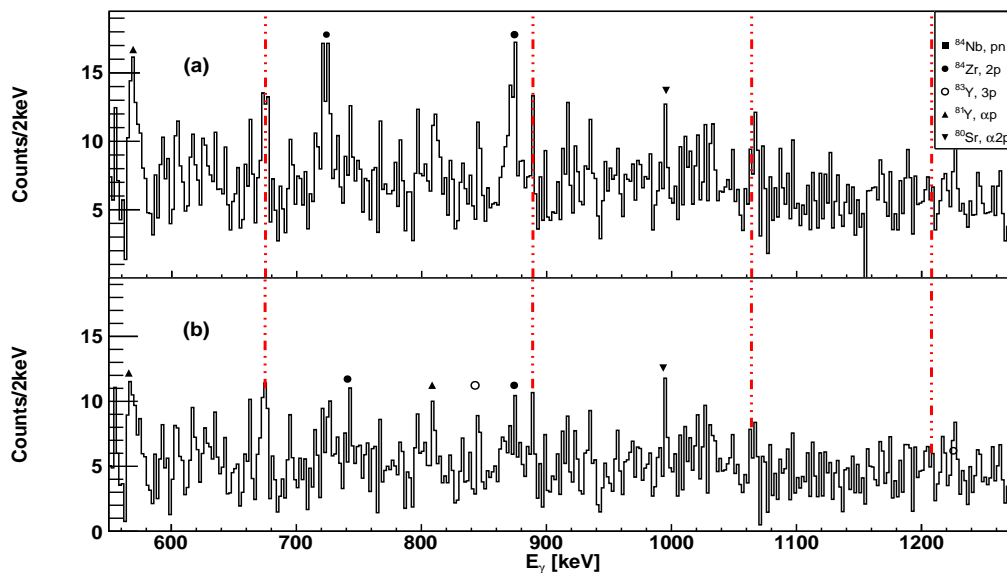
Figure 4.7: Gated γ-ray spectra showing candidate γ-ray transitions of the yrast band in ^{84}Mo (indicated with the **red** dashed lines). The gate is set on the 444-keV, $2^+ \longrightarrow 0^+$ transition in ^{84}Mo (a) on the background-subtracted recoil and M/Q-MWPC gated γ-γ matrix with a veto on the charged particles, and (b) on a charged-particle subtracted recoil and M/Q-MWPC gated γ-γ matrix with a veto on the charged particles.
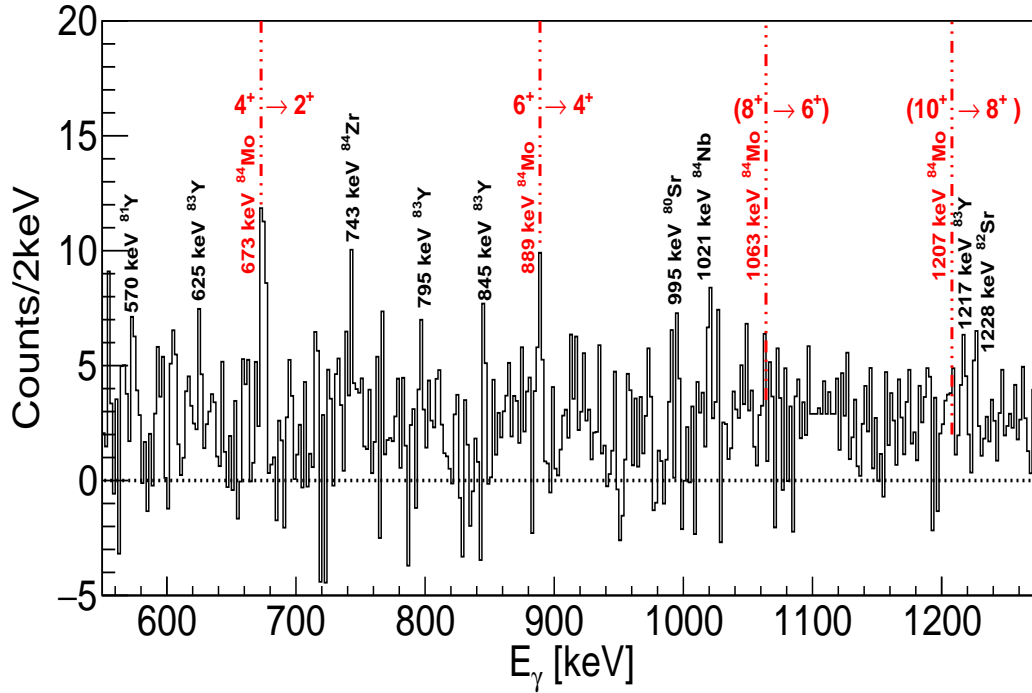
Figure 4.8: Gated γ-ray spectrum showing the candidate γ-ray transitions of the yrast band in ^{84}Mo. The details of the final background subtraction step to generate this coincidence spectrum are given in the text. The remaining contaminant γ rays are labelled in black, while the candidate transitions in ^{84}Mo are indicated with the **red** dashed lines.

this matrix is composed of a superposition of the γ-ray events corresponding to both the 2n channel and the charged-particle channels, as shown in Fig. 4.7 (b). However, a similar γ gate set on the 444-keV γ ray in the background subtracted matrix Gt0 should not have any contribution from the 2n channel but an almost equal superposition of the charged-particle channels. The spectra generated by gating on the 444-keV γ ray in the charged-particle subtracted γ-γ matrix with the JYU-Tube detector fold condition zero and in the charged-particle γ-γ matrix are denoted "444-keV gated ^{84}Mo," and "444-keV gated background", respectively. The "444-keV gated background" was then "fitted" against the "444-keV gated ^{84}Mo" spectrum by using a ROOT-based chi-squared minimization procedure. In this procedure, essentially an optimized weight is searched for the background spectrum before subtraction by comparing the shapes of the two spectra. The result of this last subtraction step is shown in Fig. 4.8. It clearly enhances the coincidences seen at 673 and 889 keV.

The work presented in Ref. [75] identified a transition at 674 keV in coincidence with the 444-keV transition after utilizing background subtraction methods based on the detected evaporated charged particles. The 674-keV γ-ray transition was then assigned as the $4^+ \longrightarrow 2^+$ transition in ^{84}Mo. Subsequent work, performed by the same group and presented in Ref. [76], yielded convincing evidence for a coincident 444-674-889-keV γ ray cascade. The natural conclusion was to assign the 889-keV γ ray as the $6^+ \longrightarrow 4^+$ transition in ^{84}Mo. In Ref. [76] some coincidence spectra showed also hints of γ-ray lines at 1063 and 1207 keV, the latter appearing highly tentative. Nevertheless, these γ rays were assigned

as the $8^+ \longrightarrow 6^+$ and $10^+ \longrightarrow 8^+$ transitions in ^{84}Mo. The results presented in Fig. 4.8 confirm the previously made assignments on the $4^+ \longrightarrow 2^+$ and $6^+ \longrightarrow 4^+$ transitions in ^{84}Mo as the γ rays at 673 and 889 keV are clearly seen in coincidence, above background, with the 444-keV transition. There appears to be some events at 1063 and 1207 keV in Fig. 4.8, but these lines are not clearly standing out from the background. Hence, if these transitions actually belong to the yrast cascade in ^{84}Mo this cannot be confirmed in the present analysis more (or less) firmly than was made in Ref. [76]. Even after the various background subtraction steps, there appears to be residual contamination from the charged-particle channels, which hinders the unambigious identification of the yrast band in ^{84}Mo beyond the 6^+ state. Moreover, having and additional gate set on the 674-keV transition is limited by the fact that this transition also belongs to the structure of strongly populated ^{81}Y.
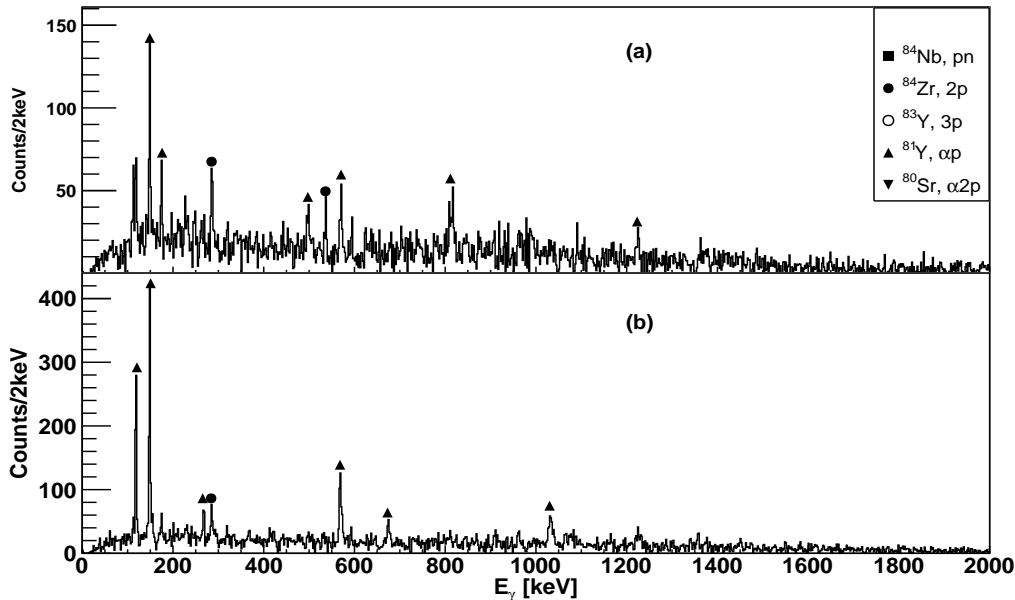
Figure 4.9: Spectra showing transitions from charged-particle channels in the recoil and M/Q-MWPC gated γ-γ matrix with a veto on the charged particles. (a) Gate on 673 keV from αp channel ^{81}Y. (b) Gate on 812 keV transition from αp channel ^{81}Y showing the coincidence with 673 keV and other charge-particle channels.

Despite the fact that the JYU-Tube detector does not have a 100% veto efficiency and no other channel selection capabilities were available, the spectrum shown in Fig. 4.8 also contain indications of the transitions beyond the $J^\pi = 6^+$ state. These are the 1063-keV line, which is the $8^+ \longrightarrow 6^+$ candidate, and the 1207-keV line being a candidate for the $10^+ \longrightarrow 8^+$ transition in ^{84}Mo identified in Ref. [76]. These assignments need further confirmation in a future experiment. It is also observed that the spectrum shown in Fig. 4.8 is still contaminated with transitions from the band structures of ^{84}Zr, ^{84}Nb, ^{83}Y, and ^{80}Sr. A critical limiting factor in the procedure described above and confirming the transitions at 1063 and 1207 keV is the inability to have a γ gate set on the γ ray with an energy of 673 keV due to the strongly populated αp channel ^{81}Y. Figure 4.9 (a) shows transitions from a γ gate set on the 673-keV γ ray. The observed coincident transitions are 965 keV,

$21/2^- \longrightarrow 17/2^-$, 812 keV, $17/2^- \longrightarrow 13/2^-$, 500 keV, $9/2^- \longrightarrow 5/2^-$. A γ gate on the 812-keV γ ray shown in Fig. 4.9 (b), shows the coincidence with 674 keV.

4.3 Discussion

The results presented above confirm the assignment of states in ^{84}Mo up to $J^\pi = 6^+$ and tentatively assign the γ rays with energies of 1063 and 1207 keV depopulating the 8^+ and 10^+ states in the yrast band, respectively. Figure 4.10 shows the yrast bands for the even-even $N = Z$ nuclei from the mass number 60 to 88.
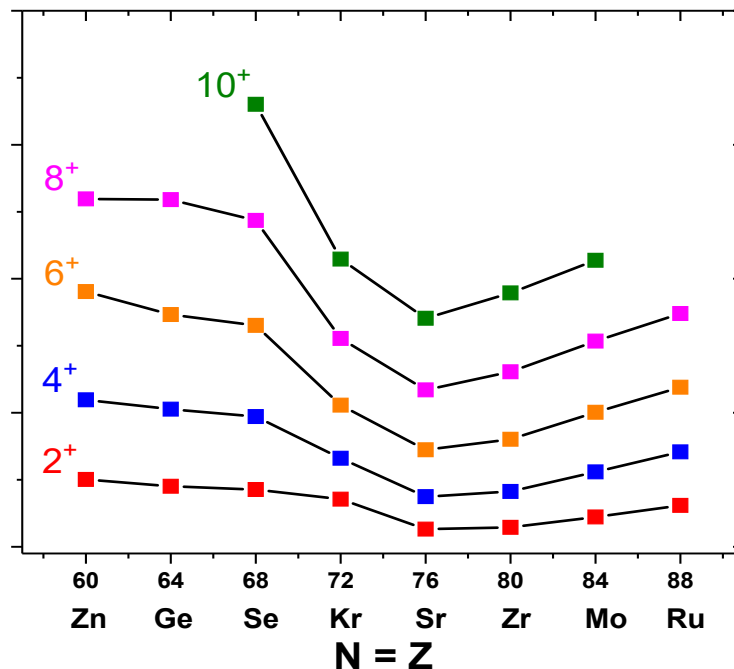
Figure 4.10:   The evolution of the yrast states in the even-even $N = Z$ nuclei from $^{60}_{30}$Zn$_{30}$ to $^{88}_{44}$Ru$_{44}$. The data is obtained from the Evaluated Nuclear Structure Data File (ENSDF) [68].

In order to explain the systematics of Fig. 4.10, it is essential to introduce the term closed-shell nuclei. The closed shell nuclei are classified into three types; doubly closed shell nuclei with equal numbers of protons and neutrons, doubly closed shell nuclei with $N > Z$, and singly closed shell nuclei. A unique characteristic of the double-closed shell nuclei with $N = Z$ is that they exhibit shape coexistence. For example, shape coexistence has been observed in ^{16}O [78]. The simple explanation is that deformation occurs in the even-even $N = Z$ nuclei because the spatial overlap of the proton and neutron configurations is maximal and it is especially the proton-neutron correlations that are generating the deformation. Figure 4.10 shows the even-even $N = Z$ nuclei between two closed shells, 28 and 50, which raises the question of the effect of partially filled and fully filled shells on the excited states.

Systematics of the excited states shown in Fig. 4.10 shows a substantial increase in collectivity towards the heavier nuclei and a decrease after $^{80}_{40}$Zr towards $^{88}_{44}$Ru. At $N = Z$ = 38, Sr, the $f_{5/2}$ sub-shell is filled, and this nucleus is more collective than $^{80}_{40}$Zr and $^{88}_{44}$Ru nuclei. ^{72}Kr has two proton and two neutron holes relative to the $f_{5/2}$ sub-shell. Therefore, it is possible to excite the ^{72}Kr nuclei by breaking a pair of nucleons and creating particle-hole pairs in the $f_{5/2}$ orbit. However, this is not the case for ^{76}Sr since the $f_{5/2}$ orbit is closed, and to excite the nucleus, a pair of nucleons are broken and raised to the next sub-shell, which takes energy. For the case of ^{84}Mo, the last four nucleons are coupled in the $g_{9/2}$ sub-shell, and to excite ^{84}Mo a pair of nucleons can be broken in the $g_{9/2}$ orbital or raise the nucleons to the $d_{5/2}$ orbital creating a particle-hole configuration, which would require more energy. This is a simple illustration used to explain excited states in nuclei. In reality, the excited states shown in Fig. 4.10 are a result of a complex collective motion of multiple nucleons in different orbitals. The most common collective modes of motion in nuclei are rotational and vibrational, which correspond to different types of patterns of excited states observed in experiments.
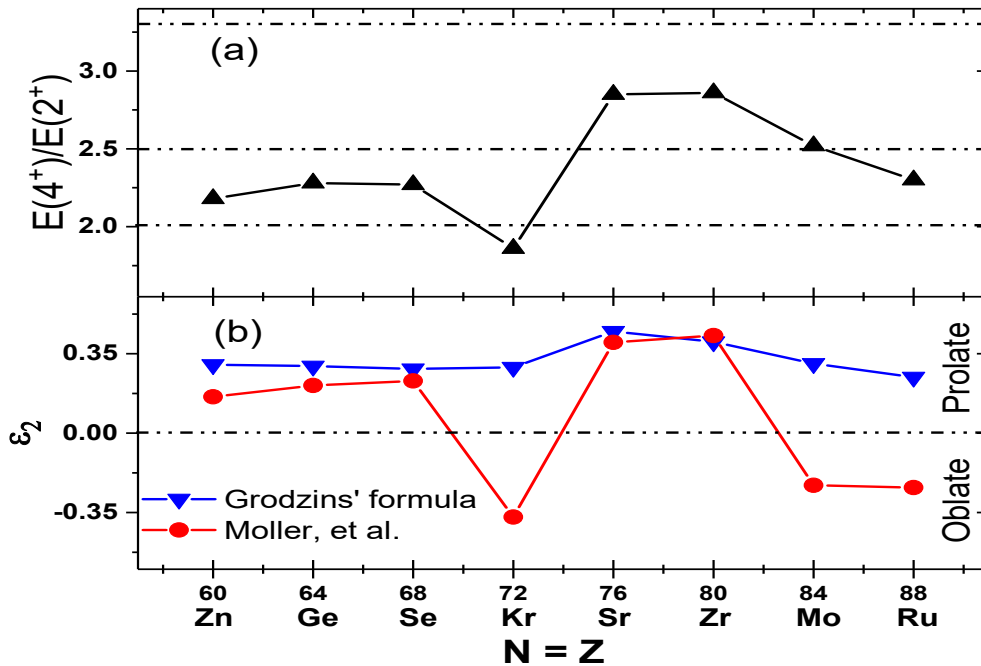
Figure 4.11: (a) Energy ratio of the 4^+ and 2^+ states for the even-even $N = Z$ nuclei from $^{60}_{30}$Zn$_{30}$ to $^{88}_{44}$Ru$_{44}$. The horizontal dashed lines represent limits expected for pure vibrational (2.00), γ-soft (2.50), and rotational (3.33) behavior [79]. (b) Values of ϵ_2, the quadrupole deformation, derived from Grodzins' formula [80, 81] for the even-even $N = Z$ nuclei and predictions by Möller, *et al.*, for the same quantity [82].

The systematics of the low-lying excited states in the $N = Z$ nuclei can be further investigated and compared. One convenient way to do this is to look at the behavior of the $E(4^+)$ and $E(2^+)$ energies and specifically their ratios. The $E(4)^+$ and $E(2^+)$ ratio with values of 2.00, 2.50, and 3.33 are expected for pure vibrational, γ-soft, and rotational behavior, respectively [79]. The $E(4)^+/E(2^+)$ values for ^{84}Mo and ^{72}Kr are 2.52 and 1.86, respectively. These values indicate a γ-soft behavior for the ^{84}Mo nucleus

and vibrational behavior for the ^{72}Kr nucleus, where the shape coexistence is predicted to exist [83]. The shape coexistence situation greatly perturbs the $E(4)^+/E(2^+)$ ratio and it has been clearly shown by Wimmer *et al.*, [5] that ^{72}Kr is not a vibrational nucleus, as suggested by the $E(4)^+/E(2^+)$ ratio, but is really a situation of shape coexistence between a well deformed prolate and an oblate structures. The $E(4)^+/E(2^+)$ ratios for ^{76}Sr and ^{80}Zr indicate rotational behavior, which suggests these systems to be deformed. The energy of the 2^+ state alone may be used to get information on the collectivity of the nucleus based on the empirical relation of Grodzins [80, 81]

$$\epsilon_2 = \left(\frac{1288}{A^{7/3}E(2^+)} \right)^{1/2}. \tag{4.2}$$

The Grodzins' theory is based on the assumption that the γ-ray transition probabilities from the first excited 2^+ states in the even-even nuclei exhibit a rather uniform behaviour. Therefore, the $E(2^+)$ values may be used to estimate the quadrupole deformation (ϵ_2) of a nucleus in its 2^+ state. The Grodzins' procedure was also used in Refs. [74, 84, 85] and led to the conclusion that while the ^{76}Sr, and ^{80}Zr are rather strongly deformed ($\epsilon_2 = 0.40$), ^{84}Mo should have a smaller deformation ($\epsilon_2 = 0.30$ [74]). From Fig. 4.11 (b), the same interpretation maybe reached. Fig. 4.11 (b) (**blue** line) indicates that the ^{72}Kr nucleus is less deformed than the other $N = Z$ nuclei shown in this region. If the Grodzin's theory would be applied to the unperturbed level energies calculated in Ref. [5], then ϵ_2 would be close to 0.38 indicating similar deformation as for ^{76}Sr, and ^{80}Zr. Lastly, the Grodzins relationship does not state the nature of the deformation, i.e., if the deformation is prolate or oblate.

Figure 4.11 (b) (**red** line) shows the calculated ground state quadrupole deformation (ϵ_2) in the Nilsson perturbed-spheroid parameterization computations by Möller *et al.*, [82]. Möller *et al.*, predict oblate deformation for ^{72}Kr, ^{84}Mo, and ^{88}Ru nuclei, and prolate deformation for ^{60}Zn, ^{64}Ge, ^{68}Se, ^{76}Sr, and ^{80}Zr. The calculated ϵ_2 values by Möller *et al.*, predict an prolate-oblate-prolate shape transition at ^{68}Se, ^{72}Kr and ^{76}Sr nuclei, and another shape transition from prolate to oblate at ^{80}Zr and ^{84}Mo. The lifetime measurements performed on the 4^+ and 2^+ states in ^{72}Kr, reported in Ref. [3] demonstrate oblate-prolate shape transition at low spin in ^{72}Kr. This observation demonstrates the rapidly evolving nuclear shapes in this region. The theoretical investigation within the EXCITED VAMPIR approximation with complex mean fields in Ref. [83] predicts a prolate deformation for the $N = Z$ ^{84}Mo which does not agree with the suggestion by Möller *et al.* Theoretical calculations by Fu and Johnson [86] suggest that ^{84}Mo has an oblate deformed ground state, while Ref. [87] predicts a spherical ground state with an oblate second minimum. The different theoretical predictions are based on different ingredients in the models used, which result in different calculated shapes.

Möller *et al.*, predictions suggest well-deformed shapes for ^{72}Kr, ^{76}Sr, ^{80}Zr, ^{84}Mo, and ^{88}Ru [82]. This is especially true for ^{76}Sr, and ^{80}Zr. The $E(4)^+/E(2^+)$ ratios, however, for these nuclei do not quite reach the values typical for rigid rotors (3.33). Similarly, the ϵ_2 value for ^{84}Mo predicted by Möller *et al.*, is in contrast with the $E(4)^+/E(2^+)$

62

ratio shown in Fig. 4.11 (a). This might be indicative of the presence of mixing of states. Mixing a 0^+ ground state and an excited 0^+ state with a different shape, pushes down the 0^+ ground state and therefore increases the $2^+ \longrightarrow 0^+$ γ-ray transition energy. This in turn reduces the $E(4)^+/E(2^+)$ ratio like is the case, e.g., for ^{72}Kr. In any case, as can be learned from this discussion, ^{84}Mo appears to be a deformed system. Experimentally Coulomb excitation measurement and/or a lifetime measurement of the excited 2^+ state in ^{84}Mo would be needed to quantify the degree of deformation.

Experimental data suggests strong isovector neutron-proton pairing, while the role of the isoscalar $T = 0$ pairing condensate has been a subject of many discussions [31]. The spectroscopy on ^{84}Mo performed in the present work aimed to identify potential experimental signature of the $T = 0$ pairing mode by analyzing the rotational response with increasing angular momentum in comparison to the $N = Z + 2$ and $N = Z + 4$ Mo nuclei. Regular sequences of states with increasing angular momentum is indicative of collective rotations. However, the Coriolis antipairing force, which is directly proportional to the increase in rotational frequency, can break a pair of nucleons increasing the moment of inertia and decreasing the rotational frequency [88]. This is visible as a "backbending" for example in the moment of inertia vs. rotational frequency graphs (see Fig. 4.12).
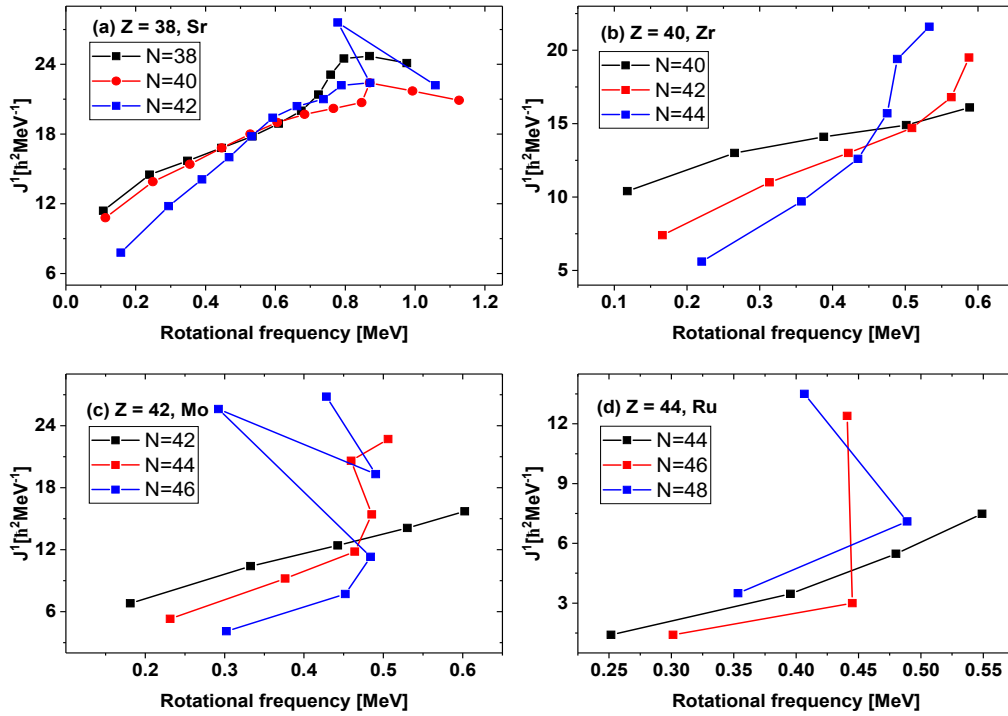
Figure 4.12: Comparison of experimental moment of inertia against the rotational frequency for the $N = Z$, $N = Z + 2$ and $N = Z + 4$ nuclei. The experimental data are from Ref. [68], except for $Z = N = 42$, which is from the present work.

Figure 4.12 compares the kinematic moments of inertia of the ground state bands of the

selected $N = Z$ nuclei with those of the heavier isotopes with $N = Z + 2$ and $N = Z + 4$. For example, Fig. 4.12 (c) shows smooth behavior for ^{84}Mo up to the highest observed rotational frequency of 0.6 MeV. This is in contrast in comparison to the two heavier molybdenum isotopes for which the backbending occurs close to each other already around 0.45 MeV as shown in Fig. 4.12 (c). The projected shell model calculation for ^{84}Mo predicts backbending to occur at a critical frequency of about 0.8 MeV [76]. The goal of the present experiment was to examine this region. The delay in backbending observed in ^{84}Mo is consistent with observations in the other $N = Z$ nuclei, such as ^{80}Zr and ^{88}Ru. In the case of even-even $N = Z$ ^{76}Sr, where the ground-state band has been observed to higher spins, a smooth backbending is observed. The delayed backbending in ^{88}Ru (and also in the other $N = Z$ nuclei) has been suggested to result from $T = 0$ neutron-proton pairs being more robust against the Coriolis antipairing force [29]. Furthermore, SM calculations by Kaneko and Zhang suggest that the enhanced proton-neutron pairing in $N = Z$ nuclei may be evidence for the delayed crossing frequency by adding an isoscalar component to the like-particle isovector pair field [89]. However, other experimental and theoretical works have raised questions about the role of the isoscalar $T = 0$ pairing in the $N = Z$ nuclei [31, 90]. For example, the observed backbending in ^{76}Sr could be reproduced without the addition of the $T = 0$ pairing in the theoretical calculations performed in Ref. [31]. Moreover, Frauendorf and Sheikh state that the observed delayed backbending in the $N = Z$ nuclei may be attributed to increased deformation [91].
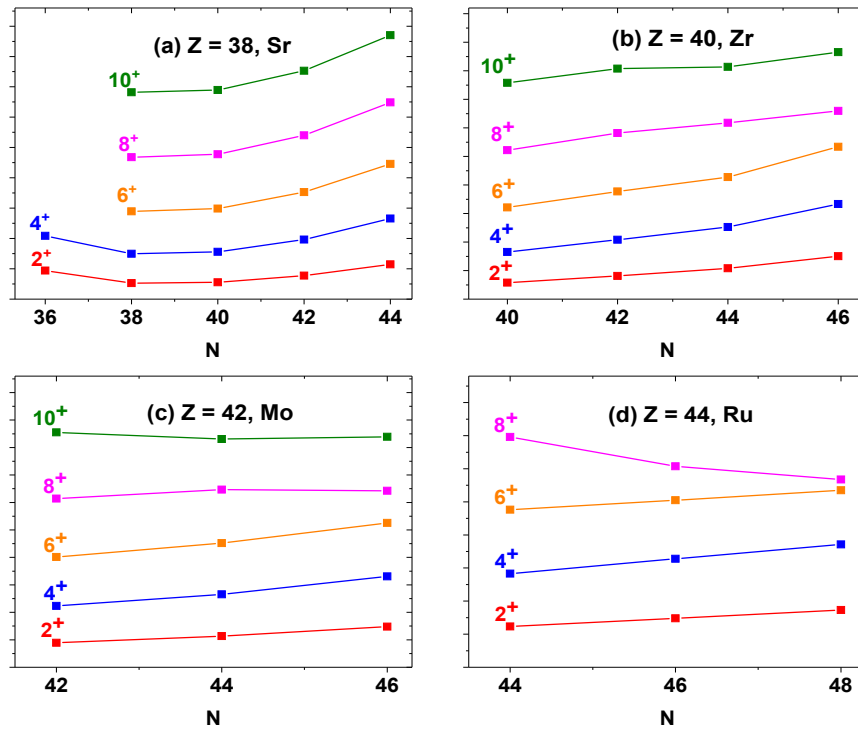
Figure 4.13: Systematics showing the evolution of excited states in selected $Z = 38$ Sr, $Z = 40$ Zr, $Z = 42$ Mo, and $Z = 44$ Ru isotopes. The experimental data are from Ref. [68], except for $Z = N = 42$, which is from the present work.

Figure 4.13 shows the evolution of excited states for selected isotopes with $Z = 38$ Sr, $Z = 40$ Zr, $Z = 42$ Mo, and $Z = 44$ Ru. Notably, the energy levels of 8^+ and 10^+ states in ^{84}Mo (shown Fig. 4.13 (c)) are tentatively assigned. Figure 4.13 suggests that deformation decreases with an increase in the number of neutrons between mass numbers 76 and 88. Systematics for the Sr isotopes, shown in Fig. 4.13 (a) indicate that ^{76}Sr has a similar level of deformation compared to ^{78}Sr and ^{80}Sr isotopes. Furthermore, Figs. 4.13 (b), (c), and (d) suggest that ^{80}Zr, ^{84}Mo, and ^{88}Ru are more deformed than the $N = Z + 2$ and $N = Z + 4$ isotopes. The backbending phenomenon observed in the curves of Fig. 4.13 can also be explained by the aligned band crossing the ground-state band. Deformation is expected to play a role in determining the point of crossing of these bands. The increased deformation in $N = Z$ nuclei may significantly influence the frequency at which backbending takes place. However, this interpretation does not exclude the effect of the $T = 0$ proton-neutron pairing correlations.

5 RECOIL-β TAGGING OF $A = 70$ NUCLEI

This chapter will present results from the fusion-evaporation reaction ^{40}Ca(^{32}S,pn/2n)^{70}Br/^{70}Kr at beam energies of 92, 96, and 103 MeV. The experiment was performed at JYFL-ACCLAB where the K-130 cyclotron delivered a ^{32}S beam, impinged on a ^{nat}Ca target rolled to a thickness of 0.6 - 0.8 mg/cm^2, with an average beam intensity of 5 pnA. Prompt γ rays were detected at the target position by the JUROGAM III γ-ray spectrometer. The vacuum-mode mass separator MARA was used to separate fusion-evaporation recoils from the primary beam and other unwanted reaction products. In addition, the JYU-Tube detector was used at the target position to detect the fusion-evaporation charged particles. Furthermore, ancillary detectors were placed at the MARA focal plane for recoil implantation and subsequent decay detection. The β-decay properties of ^{70}Br and ^{70}Kr allowed for the utilization of the recoil-β tagging (RBT) and recoil double-β (RDBT) techniques described in section 3.7. In addition, where possible, the experimental results will be compared to shell-model calculations using a $f_{5/2}, p_{1/2}, g_{9/2}$ model space with a ^{56}Ni core.

5.1 Previous experimental results of $N = Z$ nucleus ^{70}Br

The first in-beam γ-ray measurement of transitions originating from ^{70}Br was performed at the Max-Plack-Institut fur Kernphysik Heidelberg using a beam of ^{16}O, accelerated to 95 MeV which was incident on an enriched ^{58}Ni target of 5-mg.cm^{-2} thickness [92]. This in-beam γ-ray experiment was performed using a setup that consisted of one EUROBALL CLUSTER detector and three unshielded single crystal HPGe detectors. The excited ^{70}Br nucleus was produced through heavy-ion fusion-evaporation reactions in a p3n channel. To identify ^{70}Br both γ rays and evaporated particles were detected simultaneously. The evaporated charged particles from the reaction were detected using the Rossendorf silicon ball (RoSiB). The target was surrounded by aluminum foils to prevent scattered ^{16}O beam from striking the silicon detectors. The pulse-shape discrimination technique was used to

distinguish between protons and α particles [93]. In addition, the EUROBALL neutron wall was used to detect neutrons [94].

The second and third in-beam γ-ray spectroscopy experiments on ^{70}Br were carried out at Laboratori Nazionali di Legnaro (LNL), Italy and at Institut de Recherche et d'Expertise Scientifique (IRES), France, using the GASP and EUROBALL Ge arrays, respectively [95]. The second experiment to study the structure of ^{70}Br (produced via pn evaporation channel) employed a ^{32}S beam at 90 MeV from the Tandem XTU, which was used to bombard an isotopically enriched ^{40}Ca target with a thickness of 1 mg.cm^{-2} on a 14-mg.cm^{-2} thick gold backing. To improve the selectivity for the pn channel, the ISIS Si-ball and liquid scintillator detectors were mounted at the target position inside the Ge-array. The third experiment was performed using the EUROBALL array with 15 clusters and 26 clover composite Compton-suppressed Ge detectors coupled to the 4π charged-particle detection device EUCLIDES [96] and to the Neutron Wall detector [94]. The ^{70}Br nucleus was populated with the same reaction as mentioned above, and with beam energies of 90 and 95 MeV, provided by the VIVITRON accelerator of IRES.

The fourth and fifth attempts to study the excited states in ^{70}Br used two different reactions [97]. The fourth experiment [97] used the fusion evaporation reaction ^{40}Ca(^{32}S,pn)^{70}Br at beam energies of 80, 85, 90, and 100 MeV provided by the 88 Inch Cyclotron at Berkeley. The target consisted of 400-μg.cm^{-2} thick target foil of ^{40}Ca with a 120-μg.cm^{-2} thick layer of gold on the front and a 15-mg.cm^{-2} thick molybdenum backing. The Gammasphere array and low-energy photon spectrometer planar detectors were utilized to detect γ rays. Additionally, thirty downstream Gammasphere detector modules were replaced with liquid scintillator neutron detectors in order to detect neutrons for reaction channel selection. The fifth experiment to study the excited states in ^{70}Br used the fusion-evaporation reaction ^{40}Ca(^{36}Ar,αpn) with a beam energy of 145 MeV [97]. The target thickness was 400 μg.cm^2 with a 100-μgcm^2 thick gold layers on the front and back. In this experiment, Gammasphere was coupled to Microball for coincident γ-ray and charged-particle detection.

Figure 5 in Ref. [92] shows the low-spin structure of ^{70}Br observed from the fusion-evaporation reaction ^{58}Ni(^{16}O,p3n). The proposed level scheme for ^{70}Br presented in Ref. [92] is significantly different from those shown in Refs. [95] and [97]. Therefore, the proposed level scheme for ^{70}Br from Ref. [92] will not be compared to the level schemes from Refs. [95] and [97]. The proposed low-spin structures of ^{70}Br as shown in Fig. 5.1 shows the experimental results from de Angelis *et al*., [95] and Jenkins *et al*., [97]. The experiments conducted by de Angelis [95] and Jenkins [97] utilized the same reaction, and the beam energy was nearly identical. However, despite the similarities between these experiments the reported low-spin structures of ^{70}Br are different. De Angelis *et al*., reported the observation of two states above the J$^{\pi}$ = 4^{+} state in the $T = 1$ band, with the identification of a 963-keV γ ray and a very weak 1025-keV γ ray. However, the latter could not be unambiguously assigned [95]. The γ rays with energies of 963 keV and 1025 keV were assigned as γ rays decaying from the 6^{+} and 8^{+} states, respectively, which were assumed to be the $T = 1$ analog states in ^{70}Se. Jenkins *et al*., could not observe these states above the J$^{\pi}$ = 4^{+} state [97]. Figure 7 in Ref. [97] shows a spectrum double-γ gated on
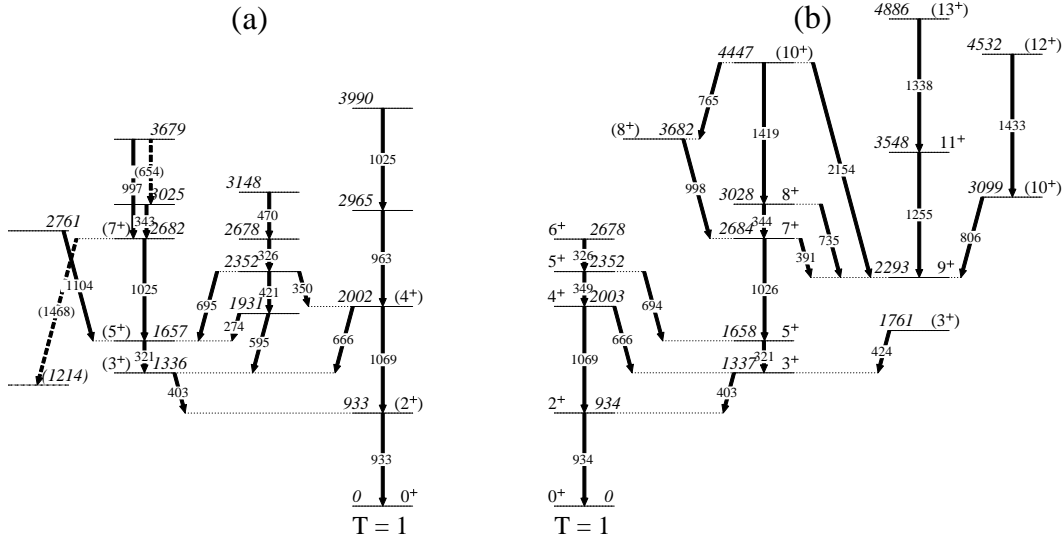
Figure 5.1: Low-spin level scheme for ^{70}Br obtained from the (a) ^{40}Ca(^{32}S,pn) [95] and (b) ^{40}Ca(^{32}S,pn) and ^{40}Ca(^{36}Ar,αpn) reactions [97].

the 934- and 1069-keV γ rays in which the higher-lying $T = 1$ band transitions should be observed, with similar energies as observed in Ref. [95]. Due to the low statistics, only two γ rays with energies of 326 and 349 keV, which were also observed by de Angelis *et al.*, [95] were observed in coincidence with the double-γ gate.

Typically in the odd-odd $N = Z$ nuclei the $T = 1$ band becomes non-yrast at relatively low excitation energy. This implies that the expected population of the high-lying states within the $T = 1$ band in fusion-evaporation reactions is weak (see, e.g., Refs. [8, 98]). This is apparently the case also for ^{70}Br. Therefore, the expected intensities for the transitions above the $J^\pi = 4^+$ state in ^{70}Br are low. Moreover, Jenkins *et al.*, discuss about the "dipole dominance" in odd-odd $N = Z$ nuclei, which in the case of ^{70}Br would for example mean preferred $M1$ decay from the $T = 1$, 6^+ state to a $T = 0$, 5^+ state [97]. The theoretical basis for the expected strong dipole transitions in odd-odd $N = Z$ nuclei has been discussed in Ref. [99]. The underlying idea is based on a quasideuteron picture of valence nucleons occupying $j = l + 1/2$ orbitals or alternatively the $j = l - 1/2$ orbitals. In the case of $j = l + 1/2$ configurations, the dipole dominance is expected, whereas the $j = l - 1/2$ configurations correspondingly reduce the $M1$ transition strength. Experimental evidence for such strong dipole transitions in $A > 60$, $N = Z$ nuclei appears to be fairly scarce [98, 100]. Lastly, in the SM picture the valence nucleons in ^{70}Br occupy the $f_{5/2}$ orbital corresponding to the $j = l - 1/2$ configuration.

5.2 Recoil-β tagging of the $N = Z$ nucleus ^{70}Br

It was found that the tagging strategy where more than one pixel was used, produced improved statistics for ^{70}Br, but at the same time significantly increased the level of background (refer to section 3.7). It is possible to subtract γ-ray peaks originating from long-lived contaminants. However, the background subtraction causes statistical fluctuations in the subtracted spectrum, which makes identification of low-intensity γ rays and weak γ-γ coincidences difficult. Therefore, the single-pixel tagging strategy was used for the search of γ-ray transitions in ^{70}Br.
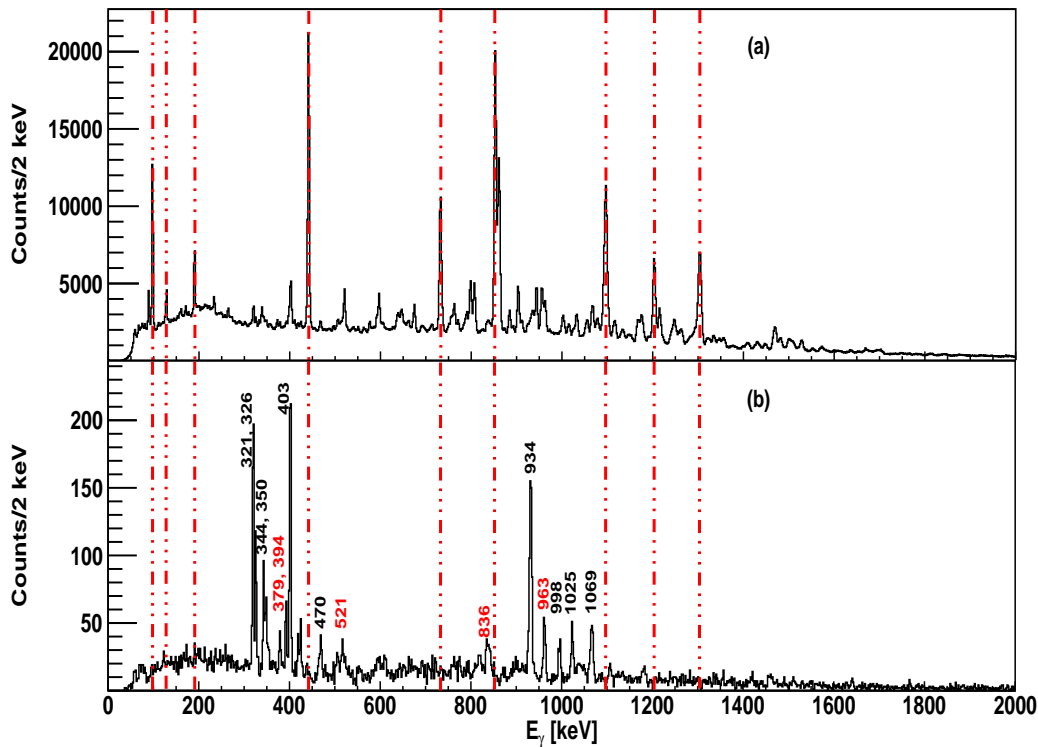
Figure 5.2: Recoil-gated and β-tagged γ-ray transitions (a) with 400-ms search time only (no condition on JYU-Tube, no β-energy gate) and (b) with 240-ms search time with one charged-particle detected in the JYU-Tube and high β-energy gate of 5 - 10 MeV. Peaks assigned to ^{70}Br are labelled in black, contaminant peaks from short-lived ^{66}As are labelled in **red** [8] and peaks from long-lived nuclei are indicated by dashed **red** lines.

The γ-ray transitions observed in ^{70}Br in the present work using the recoil-β tagging method are presented in Fig. 5.2. Figure 5.2 (a) shows recoil-β tagged γ-ray events using a relatively long search time of 400 ms for the recoil-β-decay correlations (no condition on the β-particle energy). The γ rays from ^{70}Br can not be clearly identified in Fig. 5.2 (a), since the long-lived contaminants are dominating the spectrum mostly due to random correlations.

Figure 5.2 (b) shows recoil-β tagged γ-ray events with shorter search time of 240 ms

(approximately three times the half-life of ^{70}Br), with β-energy gate of 5 - 10 MeV and one charged-particle condition. The γ rays labelled in black in Fig. 5.2 (b) are assigned to ^{70}Br [95,97]. In addition, γ rays from αpn channel ^{66}As, which is a short-lived β-decaying nucleus ($t_{1/2}$ = 96 ms) with high β-decay end-point energy, are labelled in **red** in Fig. 5.2 (b). The singles spectrum is remarkably clean. The γ rays from the αpn channel ^{66}As are visible due to the M/Q ambiguity ($M/Q = 70/14 \approx 66/13 \approx 5$), but the spectrum is dominated by the ^{70}Br γ rays. The γ rays with energies of 321, 326, 344, 350, 403, 470, 934, 998, 1025, and 1069 keV, shown in Fig. 5.2 (b), have also been observed in the two previous in-beam studies of ^{70}Br [95, 97]. The γ ray with energy of 470 keV was previously observed by de Angelis *et al.*, decaying from the state at 3148 keV and feeding the state at 2687 keV [95]. However, no spin and parity were assigned to these levels. The 998-keV γ ray, which was observed by de Angelis *et al.*, [95] and Jenkins *et al.*, [97], was also observed in the current work. Both de Angelis *et al.*, [95] and Jenkins *et al.*, [97] observed γ rays with energies of 321, 326, 344, 350, and 403 keV although the low-spin structure presented by these two authors for ^{70}Br contains differences as shown in Fig. 5.1.

In order to construct the level scheme for ^{70}Br in the present work, a recoil-β tagged $\gamma - \gamma$ matrix was required. The γ-γ analysis initially used well-known and intense γ rays originating from ^{70}Br as shown in Fig. 5.2. Figure 5.3 shows the suggested level scheme of ^{70}Br obtained from the recent experiment carried out at JYFL-ACCLAB.

5.2.1   Band 1

The orbitals involved in particle excitations in ^{70}Br are mainly $p_{3/2}$, $f_{5/2}$, $p_{1/2}$, and $g_{9/2}$, as observed in the neighbouring nuclei [95]. A proton-neutron configuration, with a mixture of the subshells mentioned above, is responsible for the $T = 1$, $I^{\pi} = 0^+$ ground state. Band 1 shown in Fig. 5.3 contains the states previously observed by de Angelis *et al.*, [95]. Figure 5.4 (a) shows the gate on the $2^+ \longrightarrow 0^+$, 934-keV γ-ray transition. Several γ rays are observed to be in coincidence with the 934-keV transition, most importantly the 963-keV and 1069-keV lines, which are the candidates for the $T = 1$, $6^+ \longrightarrow 4^+$, and $4^+ \longrightarrow 2^+$ transitions, respectively. In addition, the γ ray with an energy of 1025 keV from the $7^+ \longrightarrow 5^+$ transition is observed. This is because Band 3 is strongly populated in this reaction. The R$_{\text{DCO}}$ value (calculated using Eq. 3.21) for the 963-keV γ ray could not be extracted due to low statistics. However, based on the comparison with the isobaric analog states in ^{70}Se [68], this γ ray is tentatively assigned as an $E2$ transition from the 6^+ state and feeding the 4^+ state in the $T = 1$ band in ^{70}Br. Figure 5.4 (b) shows the 934- and 963-keV γ rays in coincidence with the γ gate set on the 1069-keV γ ray. There also appears to be a coincidence with a 1035-keV γ-ray transition, but since this γ ray was not seen in the other coincidence gates, this transition has not been placed in the ^{70}Br level scheme in the present work.

Figure 5.4 (c) shows the sum of γ gates on the γ rays with energies of 934 keV, 1069 keV, and 963 keV. A second peak is observed next to the known γ ray with energy of 1025 keV, which has an energy of 1027 keV. In addition, a γ-ray with an energy of 1151 keV is
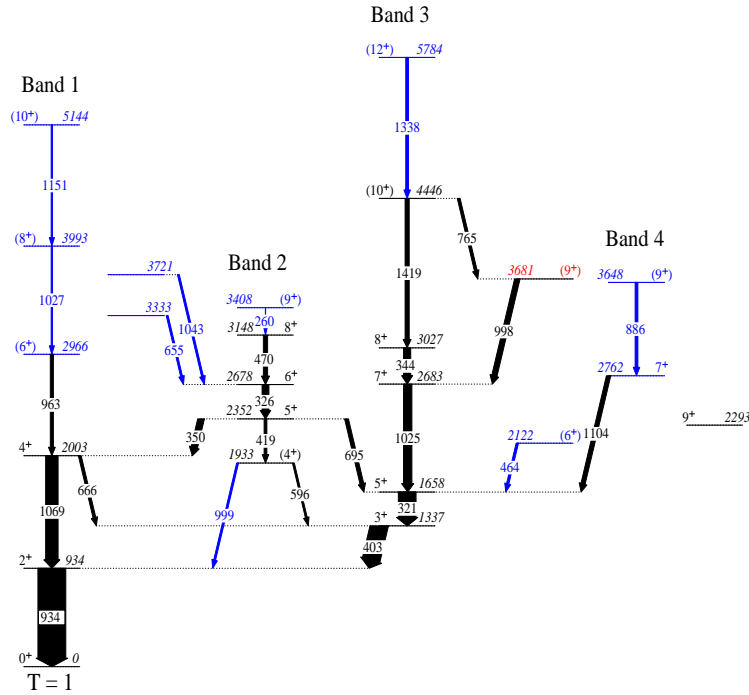
Figure 5.3: Level scheme of ^{70}Br derived in the present work using the fusion-evaporation reaction ^{40}Ca(^{32}S,pn) at beam energies of 92, 96, and 103 MeV. The width of the arrow corresponds to the intensity of the transition. The intensities of the γ-ray transitions are extracted from the recoil-β-tagged γ singles or γ-γ coincidence data. Newly assigned levels and γ-ray transition are labelled in **blue**. Labelled in **red** are previously observed transitions (states) in Ref. [97] but have been reassigned in this work. Previously observed transitions in Refs. [95, 97] and in the current work are labelled in black.

observed in this sum of γ gates. Based on the comparison with the isobaric analog states in ^{70}Se [68], the 1151-keV γ ray is tentatively assigned to de-populate a 5144-keV, (10^+) state and to feed a 3993-keV, (8^+) state, which is suggested to de-excite by the 1027-keV γ ray and feed the 2966-keV, (6^+) state within the $T = 1$ band in ^{70}Br. Two new γ rays with energies of 1182 and 1325 keV were observed in coincidence with the sum of γ gates (934 keV +1069 keV +963 keV) shown in Fig. 5.4 (c). A search of these two γ rays in our primary contaminant, the fast β decaying ^{66}As and the 2p channel ^{70}Se could not locate them. Therefore, these two γ rays might originate from ^{70}Br, but in the present analysis these γ rays could not be placed in the level scheme.

The weak population of the states at 5144, 3993, and 2966 keV prevents a definitive spin-parity assignments since the R$_{\text{DCO}}$ values cannot be extracted. The angular distribution (R$_{\text{DCO}}$) ratio of 1.17(4) and 1.19 (7) deduced for the 933 and 1069-keV γ-ray transitions suggest $E2$ character for these transitions, which further support the $2^+ \longrightarrow 0^+$ and $4^+ \longrightarrow 2^+$ assignments. To summarize, based on the $\gamma - \gamma$ analysis, angular distribution

information (R_{DCO}), and comparison with the isobaric analog states in ^{70}Se [68] Band 1 is proposed to be built on the $T = 1$, 0^+ state including γ-ray transitions of 934 keV ($2^+ \longrightarrow 0^+$), 1069 keV ($4^+ \longrightarrow 2^+$), 963 keV ($6^+ \longrightarrow 4^+$), 1027 keV ($8^+ \longrightarrow 6^+$) and 1151 keV ($10^+ \longrightarrow 8^+$).
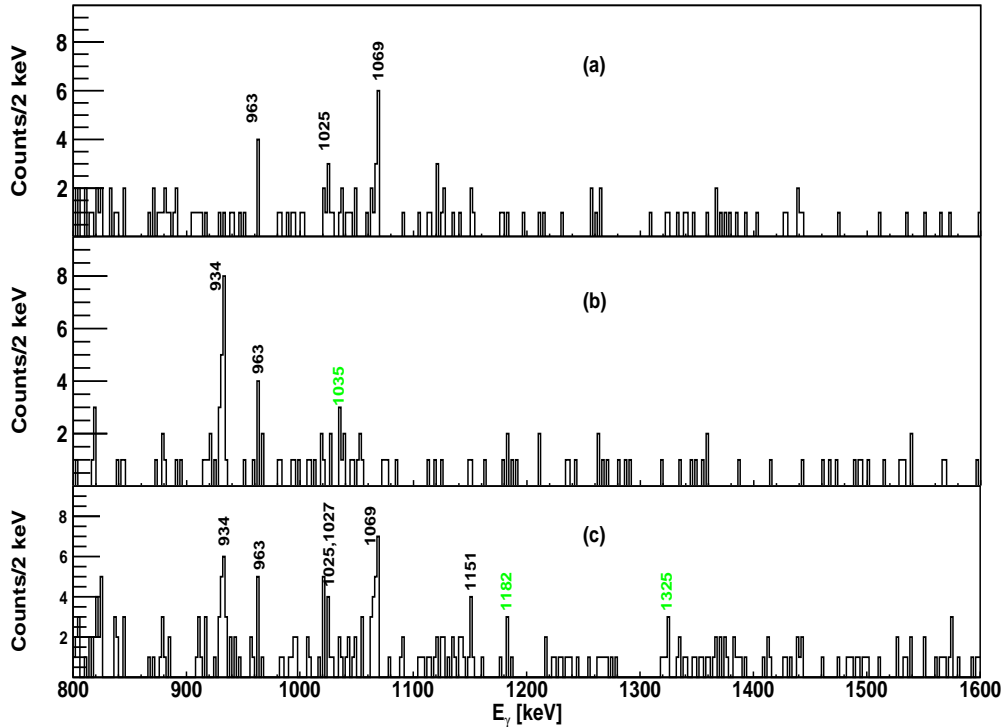
Figure 5.4: Recoil-β tagged and gated $\gamma - \gamma$ coincidence spectra requiring detection of one charged-particle in JYU-Tube and using a correlation search time of 240 ms. (a) the γ gate is set on the 934-keV γ ray with a β-energy gate of 5-10 MeV, (b) the γ gate is set on the 1069-keV γ ray with a β-energy gate of 4-10 MeV, and (c) sum of γ gates set on the γ rays with energies of 934, 1069 and 963 keV with a β-energy gate of 5-10 MeV. The origin of the γ rays labelled in **green** could not be confirmed in the present analysis.

5.2.2   Band 2

The excited states at energies of 2352, 2678, and 3148 keV in Band 2 were previously observed by de Angelis *et al.*, [95]. However, Ref. [95] proposed a bandhead with energy of 1931 keV, but was unable to assign spin-parities of the excited states in this band. Figure 5.5 (a) shows the γ gated spectrum with a gate set on the 350-keV γ ray. Obvious coincidences with the 326-, 470-, 934- and 1069-keV transitions can be observed. In addition, this spectrum shows the 666-keV γ ray very weakly, which was previously observed by both Jenkins *et al.*, [97] and de Angelis *et al.*, [95]. The γ gate set on the 326-keV γ ray (shown in Fig. 5.5 (b)) shows the previously observed relatively strong 321-, 350-, 403-, 419-, 470- and 933-keV γ-ray transitions and two reasonably strong lines at 655 keV and 1043 keV, which appear to be new. These transitions have been placed to feed the (6^+) state at 2678 keV, however, insufficient statistics prevented to extract the

R_{DCO} values and, therefore, spin-parity assignments have not been made for the states at energies of 3333 and 3721 keV. Figure 5.5 (c) shows the γ gate set on the 470-keV γ-ray transition. Both Fig. 5.5 (b) and (c) show a coincidence with a 419-keV γ ray, which has been previously seen only in Ref. [95]. The 419-keV transition is assigned to de-excite the 2352-keV state. Thus, the proposed bandhead of Band 2 is placed at an energy level of 1933 keV with a tentative spin-parity assignment of 4^+. The measured R_{DCO} values for the 326-, 350-, and 470-keV γ rays were 0.82(11), 0.79(7), and 1.23(9), respectively. Due to insufficient statistics, the R_{DCO} values for the γ rays with energies of 260 and 419 keV, could not be measured. However, this band is suggested to be composed of dipole and quadrupole transitions: 419 keV, $5^+ \longrightarrow 4^+$, 326 keV, $6^+ \longrightarrow 5^+$, 470 keV, $8^+ \longrightarrow 6^+$, and 260 keV, $9^+ \longrightarrow 8^+$.

Figure 5.5: Recoil-β tagged and gated $\gamma - \gamma$ coincidence spectra requiring detection of one charged-particle in JYU-Tube and using a correlation search time of 240 ms. (a) γ gate is set on the 350-keV γ ray with a β-energy gate of 4.5-10 MeV, (b) the γ gate is set on the 326-keV γ-ray transition with a β-energy gate of 4-10 MeV, and (c) the γ gate is set on the 470-keV γ ray with a β-energy gate of 4-10 MeV. The origin of the γ rays labelled in **green** could not be confirmed in the present analysis.

5.2.3 Band 3

Figure 5.6 (a) shows the γ rays with energies of 321, 344, 464, 596, 666, 695, 934, 998, 1025, and 1104 keV which are in coincidence with the 403-keV γ-ray transition. Jenkins
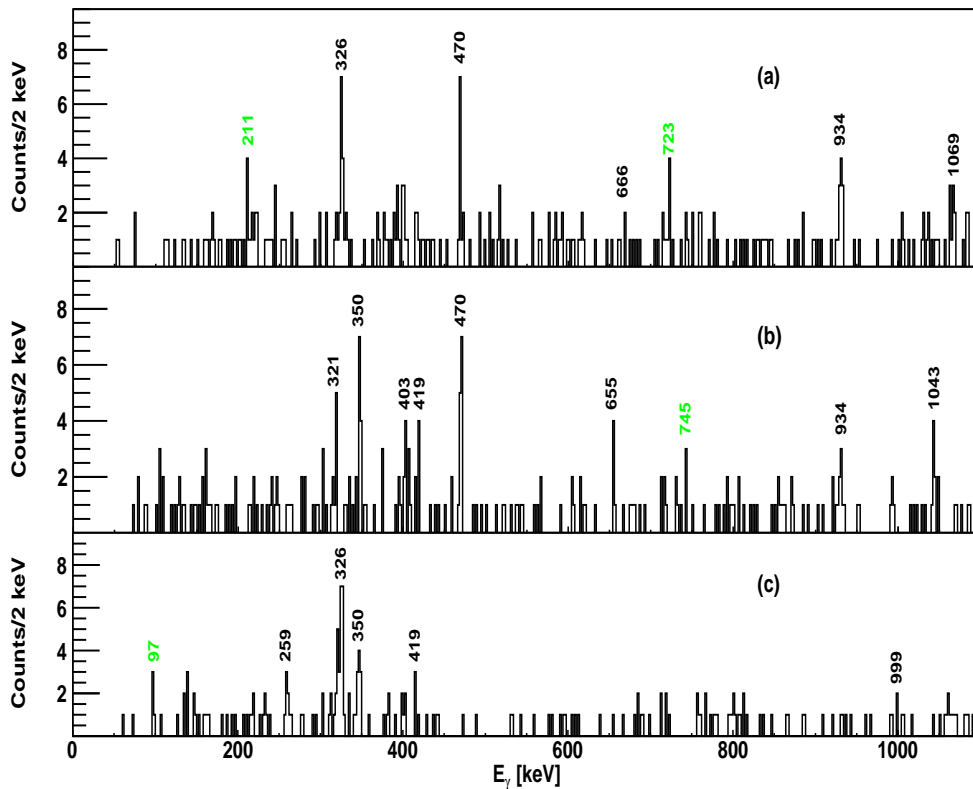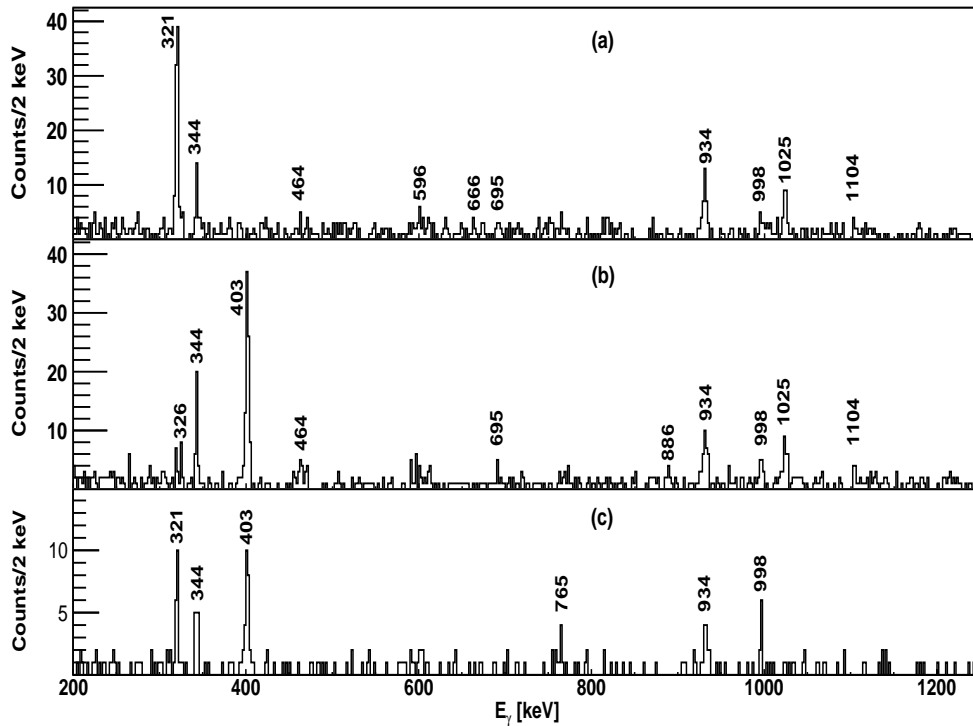
Figure 5.6: Recoil-β tagged and gated $\gamma - \gamma$ coincidence spectra with one charged-particle detected in the JYU-Tube and using a correlation search time of 240 ms. (a) the γ gate is set on the 403-keV γ-ray transition with a β-energy gate of 5-10 MeV, (b) the γ gate is set on the 321-keV γ ray with a β-energy gate of 5-10 MeV, and (c) the γ gate is set on the γ ray with energy of 1025 keV with a β-energy gate of 3-10 MeV.

et al., [97] and de Angelis *et al.,* [95] previously observed these γ rays apart from the 464-keV γ ray. In addition, the γ ray with an energy of 596 keV was not observed by Jenkins *et al.,* [97]. Figure 5.6 (b) shows the γ gate set on the 321-keV γ ray. The γ ray with energy of 464-keV is observed but with a higher intensity in Fig. 5.6 (a). Thus, the 464-keV γ-ray transition is assigned to feed the 5^+ state at 1658 keV from a state at 2122 keV. The spin-parity for the state with an energy of 2122 keV is tentatively assigned as 6^+. The γ gate set on the 1025-keV γ ray is shown in Fig. 5.6 (c), the 464-keV line is not visible in this gate, which supports its assignment. Instead, the 765-keV transition, which was observed in Ref. [97], but not in Ref. [95], is seen in coincidence with the 1025-keV line. Figure 5.7 (a) shows the γ gate on the 344-keV γ ray. The 998-keV γ ray is not observed in this gate since the 344- and 998-keV γ rays are feeding the same 7^+ state at 2683 keV.

The γ ray with an energy of 1419 keV is observed in the 344-keV gate. The 1419-keV γ ray was previously observed by Jenkins *et al.,* [97]. Figure 5.7 (b) shows the γ gate set on the 998-keV γ ray, which appears to be in anticoincidence with the 344- and 1419-keV γ rays. The 998-keV γ gate shows coincidences with the previously observed 765-keV γ ray [97] and a newly observed γ ray with an energy of 1338 keV, which is assigned to feed the state at 4446 keV. The energy sum of the 998 keV + 765 keV cascade equals to the sum of the 1419 keV + 344 keV cascade, which suggests that these cascades have the

same initial and final states. The measured R_{DCO} values for the 765- and 998-keV γ rays are 0.75(2) and 1.23(8), respectively, which supports the assignment of the state at 3681 keV as 9^+. Previously, this state was given an energy of 3682 keV and was assigned to have spin-parity of 8^+ [97]. The proposed 391-keV ($7^+ \longrightarrow 9^+$) γ ray that feeds the 9^+ isomer ($t_{1/2} = 2.2$ s) [97] is not visible here due to the used short search time. However, since states well above the excitation energy of the 9^+ isomer are seen in the present study, it can be expected that the excited states above the isomer are also populated trapping some of the prompt γ-ray intensity. Based on the measured R_{DCO} values shown in Table 5.1, the states with energies of 1337, 1658, and 2683 keV are assigned spin-parities of 3^+, 5^+, and 7^+, respectively. The 424-keV γ-ray transition observed in the recoil-β tagged singles γ-ray spectrum shown in Fig. 5.2 was assigned by Jenkins *et al.*, [97] to feed the 3^+ state at 1337 keV. However, this γ-ray transition was not observed in the γ gate set on the 403-keV γ ray, hence it is not placed in the current analysis.

The excited states with energies of 1337 keV 3^+, 1658 keV 5^+, and 2683 keV 7^+ are based on the $\pi p_{3/2} \nu p_{3/2}$, $\pi f_{5/2} \nu f_{5/2}$ and $\pi g_{9/2} \nu g_{9/2}$, configurations, respectively. The measured R_{DCO} value for the 344-keV transition supports the dipole character. Thus, the state 3027 keV is suggested to be an 8^+ state and can be identified as a non-collective $9/2[404]\pi 7/2[413]\nu \otimes 7/2[413]\pi 9/2[404]\nu$ bandhead according to Ref. [97].
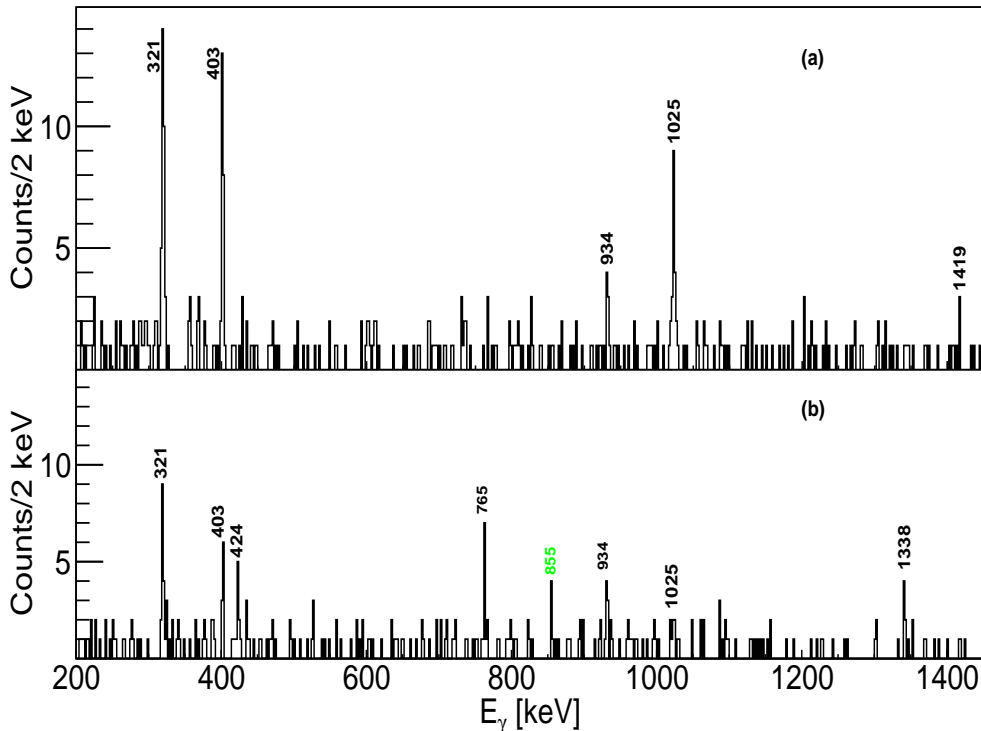

Figure 5.7: Recoil-β tagged and gated $\gamma - \gamma$ coincidence spectra requiring detection of one charged-particle in JYU-Tube and using a correlation search time of 240 ms. (a) the γ gate is set on the 344-keV γ-ray transition with a β-energy gate of 4-10 MeV, and (b) the γ gate is set on the 998-keV γ-ray with a β-energy gate of 4-10 MeV. The origin of the γ rays labelled in **green** could not be confirmed in the present analysis.

5.2.4 Band 4

Figures 5.8 (a) and (b) show γ gates set on the 1025- and 1104-keV γ rays, respectively, and the observed coincident γ rays. Figure 5.8 (b) shows a newly observed γ ray with energy of 886 keV feeding the excited state at 2762 keV. Figure 5.8 (a) supports the placement of the γ rays with energies of 886 and 1104 keV in the level scheme as γ rays feeding the excited 5^+ state at 1658 keV since these are not observed in this γ gate. The measured R_{DCO} value for the 1104-keV γ ray is 1.17(7), which supports the an $E2$ character. However, the R_{DCO} value for the 886-keV γ ray could not be measured due to statistical limitations. The levels at 2762 keV (7^+) and 3748 keV (9^+) are relatively close in energy to the 7^+ and 9^+ states in Band 3.
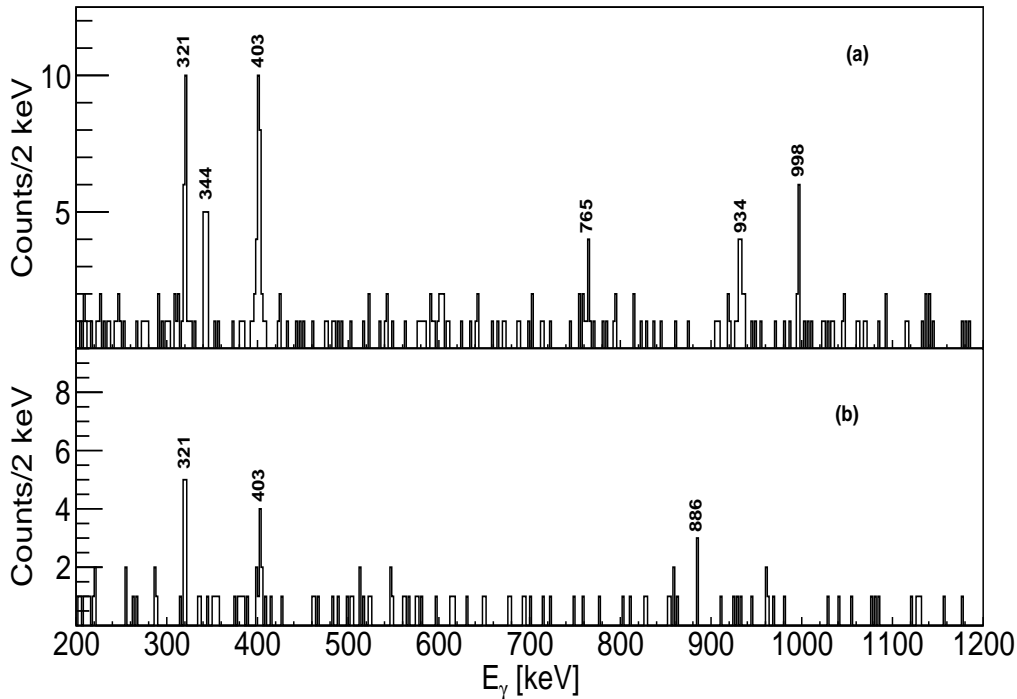
Figure 5.8: Recoil-β tagged and gated $\gamma - \gamma$ coincidence spectra requiring detection of one charged-particle in JYU-Tube and using a correlation search time of 240 ms. (a) the γ gate is set on the 1025-keV γ ray with a β-energy gate of 3-10 MeV, and (b) the γ gate is set on the 1104-keV γ ray with a β-energy gate of 4-10 MeV.

The current work established the level scheme of the odd-odd $N = Z$ nucleus ^{70}Br for the first time using the recoil-β tagging method and most importantly, this work proposes new transitions in the $T = 1$ band above the $J^\pi = 4^+$ state. A number of γ rays could not be placed in the level scheme due to insufficient statistics. In addition, the angular distribution information (R_{DCO}) for all the γ rays placed in the proposed level scheme of ^{70}Br shown in Fig. 5.3 could not be measured due to inadequate statistics. The R_{DCO} results for the measured γ rays are shown in Fig. 5.9. The results from the ^{40}Ca(^{32}S,pn)^{70}Br experiment are summarized in Table 5.1.

Table 5.1: The prompt γ-ray transitions measured for odd-odd ^{70}Br from the fusion-evaporation reaction ^{40}Ca(^{32}S,pn) at beam energies of 92, 96, and 103 MeV. The energy of the γ ray (E$_\gamma$), relative γ-ray intensity normalized to the $2^+ \longrightarrow 0^+$ transition, initial level energy (E$_i$), final level energy (E$_f$), assigned spin and parity of the initial and final levels (I_i^π and I_f^π) and angular distribution information (R$_{DCO}$) are listed.

E$_\gamma$ [keV]	I%	E$_i$ [keV]	E$_f$[keV]	I_i^π	I_f^π	R$_{DCO}$
260(1)	<10.0	3408	3148	(9^+)	8^+	
321(2)	62.5	1658	1337	5^+	3^+	1.15(4)^a
326(1)	24.4	2678	2352	6^+	5^+	0.82(11)^b
344(1)	25.7	3027	2683	8^+	7^+	0.77(4)^a
350(1)	23.2	2352	2003	5^+	4^+	0.79(7)^c
403(2)	63.9	1337	934	3^+	2^+	0.88(4)
419(2)	14.2	2352	1933	5^+	4^+	
464(1)	8.3	2122	1658			
470(1)	15.3	3148	2678	8^+	6^+	1.23(9)^b
595(2)	9.5	1933	1337	(4^+)	3^+	
655(1)	<10	3333	2678	(8^+)	6^+	
666(2)	<10	2003	1337	4^+	3^+	
695(2)	9.6	2352	1658	5^+	5^+	
765(1)	16.6	4446	3681	10^+	9^+	0.75(2)^d
886(2)	13.2	3648	2762			
934(2)	100.0	934	0	2^+	0^+	1.17(4)
963(2)	11.2	2966	2003	6^+	4^+	
998(2)	19.0	3681	2683	9^+	7^+	1.23(8)^d
999(2)	6.3	1933	934	(4^+)	2^+	
1025(3)	18.2	2683	1658	7^+	5^+	1.21(4)^a
1027(3)	11.6	3993	2966	(8^+)	(6^+)	
1043(2)	<10.0	3721	2678	(8^+)	6^+	
1069(3)	44.6	2003	934	4^+	2^+	1.19(7)^c
1104(2)	15.2	2762	1658	7^+	5^+	1.17(7)^a
1151(2)	<10	5144	3993	10^+	8^+	
1338(3)	14.2	5784	4446	12^+	10^+	
1419(3)	14.8	4446	3027	10^+	8^+	

^{a} Gate on 403 keV

^{b} Gate on 350 keV

^{c} Gate on 934 keV

^{d} Gate on 1025 keV
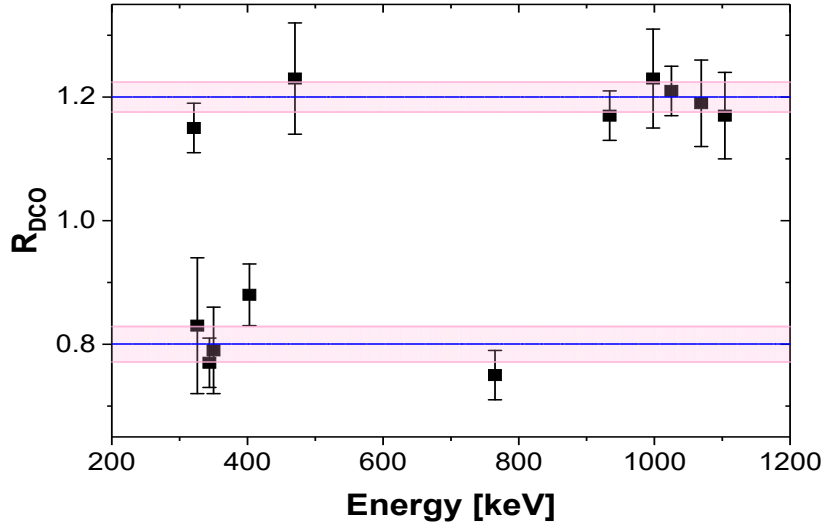
Figure 5.9: Experimentally measured angular distribution (R_{DCO}) values for several transitions from ^{70}Br using Eq. 3.21. The **blue** lines (pink lines are the errors) shows the average R_{DCO} of 1.20(3) and 0.80(2) for quadrupole and dipole transitions.

5.3 Shell-model calculations for $N = Z$ nucleus ^{70}Br

The two-quasi-particle-rotor model (TQRM) [101] was used in the previous study of ^{70}Br, where both the collective even-even core and two quasi-particles were explicitly treated [97]. In the TQRM, the core was modeled as an axially symmetrical or triaxial system, constrained to a single rigid shape, which does not allow for shape-coexistence or softness. The TQRM was able to accurately describe $N = Z + 4$ nuclei without the need for any residual proton-neutron (np) interaction. For odd-odd ^{70}Br, Ref. [97] showed that the inclusion of the proton-neutron residual interaction in TQRM calculations improved the agreement with the experiment. However, it was emphasized in Ref. [101] that the np pairing investigations in ^{70}Br are complicated by the shape coexistence and shape mixing phenomena affecting to the low-spin level scheme. The current experiment yielded much-needed information for the low-spin structure of ^{70}Br. Thus, new SM calculations were performed using ^{56}Ni as the core.

The SM calculations in this study utilized the $f_{5/2}, p_{1/2}, g_{9/2}$ model space for protons and neutrons, with a $^{56}_{28}$Ni$_{28}$ as inert core [102]. The effective Hamiltonian's two-body matrix elements were derived from the charge-dependent Bonn nucleon-nucleon potential (CD-Bonn NN potential) using many-body perturbation theory [107]. The low-momentum potential V^{low-k} approach was used to renormalize the matrix elements [103], along with a Coulomb term for proton-proton interactions. It is important to note that the V^{low-k} approach contains less information than the full NN potential and is energy-independent. Single-neutron and single-proton energies were obtained from experimental energy spectra of ^{57}Ni and ^{57}Cu, respectively, when possible, to account for the implicit effects of three-body forces on single-particle energies. For more information on the SM calculation

procedure, see Refs. [104–107] and references therein.
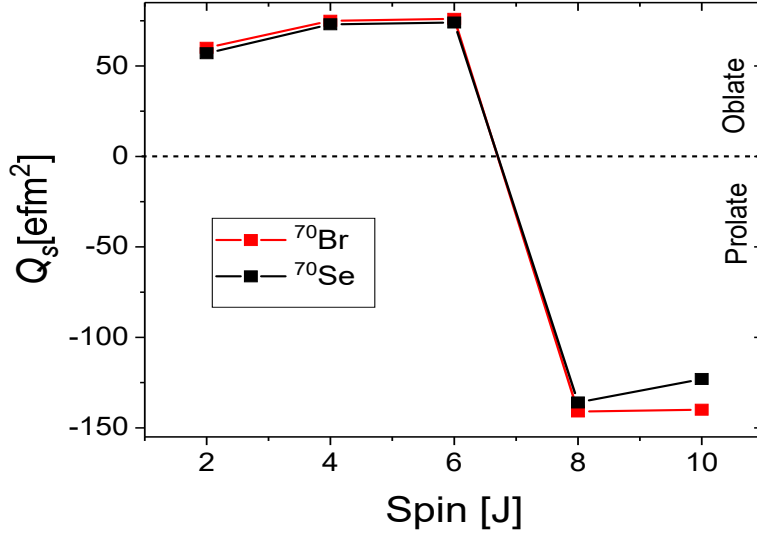
Figure 5.10: Spectroscopic quadrupole moments obtained from SM calculations as a function of spin for the low-lying $T = 1$ states in ^{70}Br and ^{70}Se [102].

Information on quadrupole collectivity and nuclear deformation can be obtained from reduced transition strengths, $B(E2)$ values. Electromagnetic transition strengths for the $2^+ \longrightarrow 0^+$ transition in the ground-state band have been measured for several even–even $N = Z$ nuclei in the region; ^{64}Ge [108], ^{68}Se [109], ^{72}Kr [110], ^{76}Sr [111], and ^{80}Zr [11]. These studies indicate a rapid increase in collectivity for the even-even nuclei between ^{68}Se and ^{72}Kr. Increase in collectivity is closely related to the potential evolution of nuclear deformation. Figure 5.10 shows the SM calculated spectroscopic quadrupole moments (Q_s[emf^2]) as a function of spin for the low-lying states in $N = Z$, ^{70}Br and $N = Z + 2$, ^{70}Se [102]. Despite the challenge of theoretically describing odd-odd $N = Z$ systems, the current SM calculations show relatively good agreement with the available experimental data for the $2^+ \longrightarrow 0^+$ transitions in ^{70}Br and ^{70}Se [6, 112]. It should be noted that, while the earlier reports claimed prolate deformation for the first 2^+_1 state in ^{70}Se [113], recent evidence presented in Refs. [6, 112, 114] suggests that the 2^+_1 state in ^{70}Se is oblate deformed. The newly calculated Q_s values shown in Fig. 5.10 are in agreement with Ref. [112] that the 2^+_1 and 4^+_1 states in ^{70}Se are oblate deformed. However, Ref. [112] suggests a prolate shape for the 6^+_1 state, while the calculated values indicate a sudden shape change from oblate to prolate deformation from the 6^+_1 state to the 8^+_1 state, as illustrated in Fig. 5.10. The measured $B(E2; 2^+ \longrightarrow 0^+)$ values for ^{70}Br and ^{70}Se, reported in Ref. [6], in addition to the lifetime measurements reported in Ref. [13], suggest similar structures for these nuclei at low-spin. This observation is in agreement with the calculated spectroscopic quadrupole moments for the low-spin states in ^{70}Br and ^{70}Se, shown in Fig. 5.10.

Figure 5.10 indicates the presence of an oblate-prolate coexistence in ^{70}Br and ^{70}Se. For the $J^\pi = 2^+, 4^+, 6^+$ states, the quadrupole moments are predicted to be positive, indicating

Table 5.2: Experimental level energies for $T = 1$ band in ^{70}Br and ^{70}Se compared to the large-scale shell-model calculations [102].

J^π	^{70}Br		^{70}Se	
	Energy Level Exp [MeV]	Energy Level Th [MeV]	Energy Level Exp [MeV]	Energy Level Th [MeV]
0^+	0	0	0	0
2^+	0.934	0.827	0.944	0.898
4^+	2.003	1.871	2.038	1.942
6^+	2.966	3.225	3.003	3.282
8^+	3.993	4.008	4.037	4.063
10^+	5.144	4.604	5.205	5.369

oblate deformation. For the higher-spin analog states with $J^\pi > 6^+$, the prolate shapes are predicted to dominate, but the currently available experimental data does not allow to verify this. Comparison of the experimental isobaric analog level energies in ^{70}Br and ^{70}Se show that these are similar, as can be expected based on the mirror symmetry. This indicates that the shape evolution in ^{70}Br and ^{70}Se remains similar. The analysis of the structure of the investigated states in ^{70}Br reveals that the proposed $T = 1$ band is similar to the well-known isobaric analog states in ^{70}Se. Lastly, Table 5.2 shows experimental and theoretically predicted level energies in ^{70}Br and ^{70}Se. The theoretically predicted level energies of the low-lying states are in relatively good agreement with the experimental values apart from the $J^\pi = 10^+$ state in ^{70}Br, where the theory underestimates the state by about 600 keV.

5.4 Coulomb energy differences for $A = 70$

Table 5.2 shows the experimental and theoretical level energies of the $T = 1$ band in ^{70}Br as well as the level energies of the analog states in ^{70}Se. The resulting Coulomb energy differences (CED) between the analog states are shown in Fig. 5.11, without theoretically predicted value for the $J^\pi = 10^+$ state due to the underestimation of the level energy for ^{70}Br. The present work confirms the unique negative behaviour of the CED observed so far only within the $A = 70$ pair [8, 12, 19, 23]. Although, the theoretically predicted CED values are not particularly close to the experimental values, the general trend is similar, i.e., negative.

The CED values between the odd-odd $N = Z$ and even-even $N = Z + 2$ pairs with mass $A = 62, 66, 74$ and 78 all show positive trends as a function of spin. This has been attributed to result from the interplay of Coulomb multipole effects and alignment of valence nucleons when angular momentum is generated. In the alignment process, the overlap of the valence nucleon wave functions reduces, which influences the excitation energies of the states. The effect on the level energies depends on the type of the nucleon pair, which is aligning. The typical argument, which is also supported by some theoretical calculations (see, e.g., Ref. [2]), is that there are more proton-proton pairs in the $N = Z$ + 2 member than in the odd-odd, $N = Z$ member. The proton-proton pairs experience reduction in the Coulomb energy as the wavefunction overlap reduces, which is then

reflected as reduced excitation energies in comparison to the analog states in the $N = Z$ system. Therefore, positive CED trends are expected and also experimentally observed in the most cases.
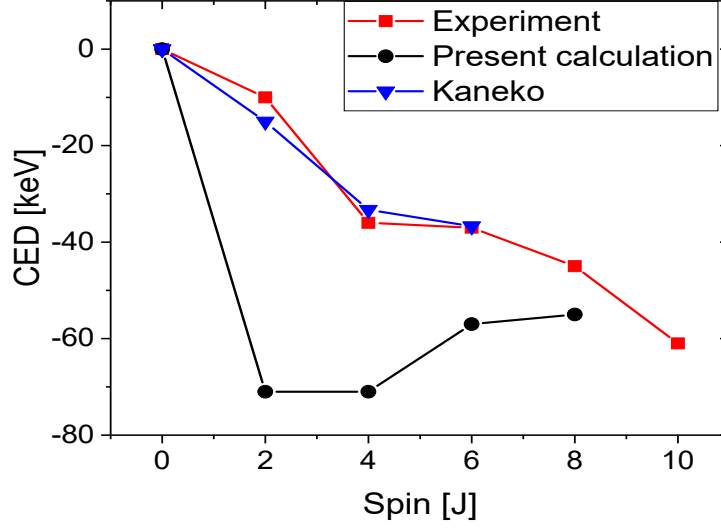
Figure 5.11: Coulomb energy differences ($E_x^{I\pi}(T_z= 0)$ - $E_x^{I\pi}(T_z = 1)$) between isobaric analog states in ^{70}Br and ^{70}Se nuclei as a function of the spin (J). Experimental CED data is shown in **red**, present shell-model calculation in **black** and calculations by Kaneko *et al*., in **blue** (obtained from Ref. [19]).

The emergence of the negative CED trend for the $A = 70$ pair started to attract interest immediately when the first $T = 1$ states in ^{70}Br were identified [95]. One suggestion given in Ref. [95], was based on the argument of extended proton radius for the drip-line nucleus ^{70}Br, which would lead to reduced Coulomb repulsion as the proton wave function would be spatially extended. However, this kind of Thomas-Ehrman shift type of an effect would be expected to be seen also in the other medium-heavy $N = Z$ systems, but such evidence does not exist. Ref. [12] discusses the anomalous negative CED trend for the mass $A = 70$ pair resulting from shape changes between ^{70}Br and ^{70}Se, without providing detailed theoretical support for this claim. However, more detailed theoretical analysis based on the complex excited VAMPIR calculations reported in Ref. [115] reached similar conclusion. In Ref. [115] the anomalous CED trend at $A = 70$ was demonstrated to result from different shape mixing behavior of the ^{70}Br and ^{70}Se excited states. According to the calculation, the oblate shapes were more dominant in ^{70}Se than in ^{70}Br. This, obviously, stands in contrast to the shell model calculations and conclusions presented in the previous section, which suggest nearly identical shapes for ^{70}Br and ^{70}Se at low spin. Third explanation is provided by Kaneko *et al*. in Ref. [19]. Their shell-model calculations using JUN45 interaction correctly produce the negative CED for the mass $A = 70$ pair with nearly static oblate deformation for ^{70}Se (and presumably for ^{70}Br as well) up to $J^\pi = 6^+$. The anomaly was demonstrated to be due to enhanced neutron excitations (and reduced proton excitations) from the fp shell to the $g_{9/2}$ orbital resulting from the electromagnetic spin-orbit interaction, which alters the neutron and proton single-particle orbitals in opposite

directions. As can be observed from Fig. 5.11, the calculation by Kaneko *et al.*, containing contributions from the Coulomb monopole, multipole and spin-orbit terms, reproduces the experimental data well. From the present shell-model calculations such a detailed analysis on the microscopic structure cannot be made, but these calculations also point to the fact the evolving shapes are not the main contributor for the negative CED at $A = 70$.

5.5 Recoil double-β tagging of ^{70}Kr

The level structure of ^{70}Kr has been studied earlier at JYFL-ACCLAB using the RITU gas-filled separator (designed primarily for heavy element studies) [116] and the JUROGAM II Ge-detector array [10]. Based on the comparison to the other members of the $A = 70$ isobaric triplet (^{70}Br and ^{70}Se), in Ref. [10] γ rays with energies of 870(1) keV and 997(1) keV were tentatively assigned to represent the $2^+ \rightarrow 0^+$ and $4^+ \rightarrow 2^+$ transitions in ^{70}Kr, respectively. More recently the excited states in ^{70}Kr have been populated using one- and two-neutron removal and inelastic scattering reactions at RIKEN [4]. Based on this study the γ-ray energies of the $2^+ \rightarrow 0^+$ and $4^+ \rightarrow 2^+$ transitions in ^{70}Kr were reported to be 884(4)(5) keV and 1029(14)(5) keV, respectively. Hence, there is an apparent disagreement between the two recent results presented in Ref. [10] and [4], which can not be explained by the fairly large energy resolution of the DALI 2 scintillator array used in Ref. [4].

Figure 5.12 (a) shows a recoil-gated and β-tagged JUROGAM III γ ray spectrum with a recoil-β correlation time of 260 ms, β-particle energy gate of 5 - 10 MeV, and requiring one detected proton in JYU-Tube. The resulting γ ray spectrum shows known transitions originating from ^{66}As [8] and ^{70}Br, which are all labelled with their γ-ray energies in gray. In Fig. 5.12 (b), the same recoil-β correlation conditions are used as in panel (a), but now requiring detection of zero charged particles in JYU-Tube and correlation time of 90 ms. Since the JYU-Tube veto efficiency for one proton is approximately 70%, the ^{66}As and ^{70}Br γ-ray lines leak through to the charged-particle vetoed spectrum shown in Fig. 5.12 (b). However, owing to the charged-particle veto condition, two γ-ray peaks at energies of 881(1) and 1036(2) keV, marked with the **red** dashed vertical lines, become visible in Fig. 5.12 (b). These γ rays are potentially originating from ^{70}Kr (2n channel). The candidate 881- and 1035-keV γ rays are within the uncertainties of the 1029(14)(5) keV, $4^+ \longrightarrow 2^+$ and 884(4)(5) keV, $2^+ \longrightarrow 0^+$ transitions reported in Ref. [4]. To unambiguously identify the ^{70}Kr γ-ray transitions in the present work, the recoil-double-β tagging (RDBT) method was employed, as described in section 3.7. The 45.19(14)-ms [117], ^{70}Kr $\longrightarrow ^{70}$Br β decay, followed by the 78.42(51)-ms [118], ^{70}Br $\longrightarrow ^{70}$Se β decay provides a clean tag for the identification of γ rays originating from ^{70}Kr. This method has been applied in Fig. 5.12 (c), where, in addition to the charged-particle veto, the correlation times and β-energy thresholds for the first and second β decay are 90 ms, 260 ms, 5 - 10 MeV, and 0.8 - 10 MeV, respectively. As shown in Fig. 5.12 (c), the RDBT method yields two γ-ray lines at the same energies as identified in the panel (b) of Fig. 5.12. In addition, more strict double-β correlation conditions of 70 ms, 190 ms, 5 - 10 MeV and 2 - 10 MeV are applied
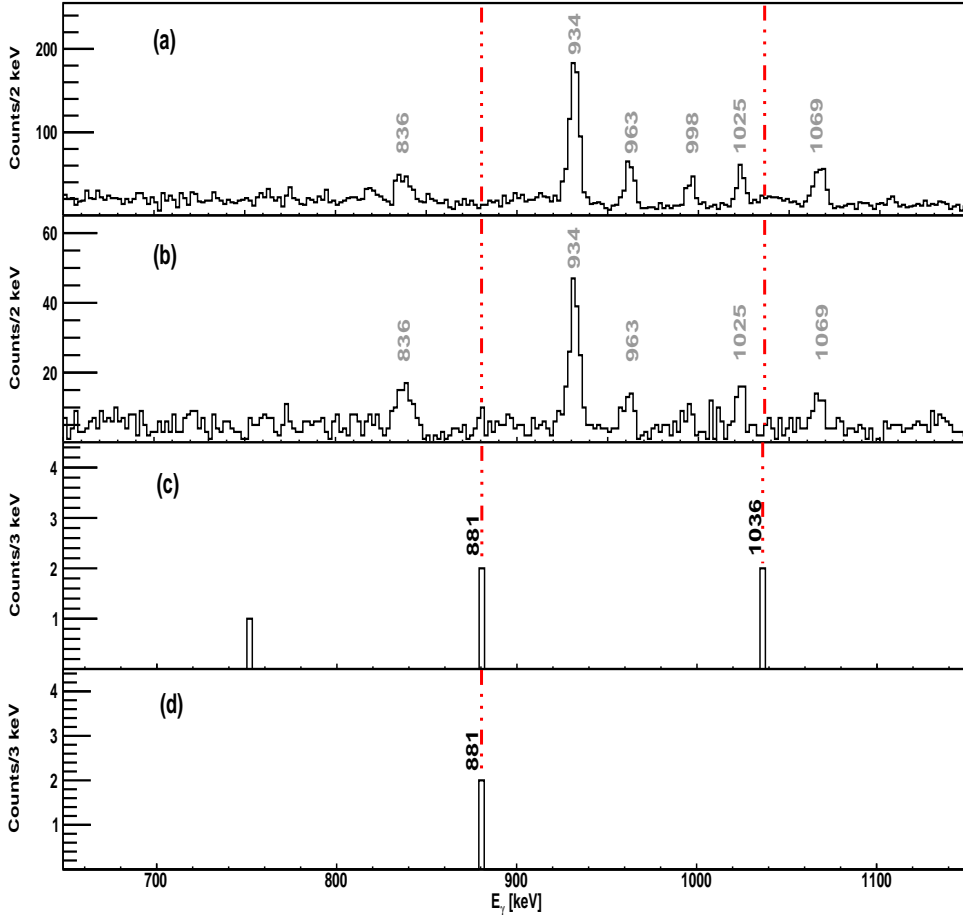
Figure 5.12: (a) Recoil-β tagged γ rays with search time of 260 ms, β-energy gate of 5 - 10 MeV and with one detected proton in JYU-Tube. (b) same as (a), but requiring detection of 0 protons in JYU-Tube and a search time of 90 ms. (c) recoil-$\beta - \beta$ correlated γ rays with charged-particle veto leading to identification of candidate γ rays in ^{70}Kr. The correlation conditions for the first β decay are 90 ms and 5 - 10 MeV, while for the second β decay these are 260 ms and 0.8 - 10 MeV. (d) same as (c), but with stricter correlation conditions of 70 ms, 190 ms, 5 - 10 MeV and 2 - 10 MeV. The gray labelled γ rays in panels (a) and (b) are known transitions from ^{66}As and ^{70}Br. This data is from the fusion-evaporation reaction ^{40}Ca(^{32}S,xαypzn) at beam energies of 92, 96, and 103 MeV. The **red** dashed vertical lines represent position of γ rays that are potentially originating from ^{70}Kr (2n channel).

in Fig. 5.12 (d), only two γ-ray events are observed at an energy of 881(1) keV, which is therefore assigned as the $2^+ \longrightarrow 0^+$ transition in ^{70}Kr. The γ ray with energy of 1036(2) keV observed in Fig. 5.12 (c) is tentatively assigned as the $4^+ \longrightarrow 2^+$ transition. Both the 1036(2)- and 881(1)-keV γ rays agree within uncertainty with the previously measured $4^+ \longrightarrow 2^+$ and $2^+ \longrightarrow 0^+$ transitions in Ref. [4]. However, the γ ray energies measured in the current work provide more accurate excitation energy values for the 2^+ and 4^+ states.

Table 5.3 compares the experimental MED and TED values with the results obtained from SM calculations performed with the JUN45 interaction in the $f_{5/2}, p_{1/2}, g_{9/2}$ model space [119]. The SM calculations include an isospin non-conserving (INC) interaction with an isotensor ($\beta_2^{J=0} = \beta_{pp} + \beta_{nn} - 2\beta_{pn}$) strength of 100 keV, and isovector ($\beta_1^{J=0}$

Table 5.3: Experimental mirror and triplet energy differences for the 2^+ and 4^+ states in the mass $A = 70$ triplet compared to the predictions obtained from the SM calculations with (w) and without (w/o) the INC interaction [10]. The SM calculations were performed with the JUN45 interaction in the $f_{5/2}, p_{1/2}, g_{9/2}$ model space [119].

$I_i^\pi \longrightarrow I_f^\pi$	E_γ	Experimental		Theoretical			
		MED [keV]	TED [keV]	MED [keV]		TED [keV]	
				SM w INC	SM w/o INC	SM w. INC	SM w/o INC
$2^+ \longrightarrow 0^+$	870^a	-74.5	-53.5	-70	-50	-68	-24
	$884(6)^b$	-60.5	-39.5				
	$881(1)^c$	-64.5	-43.5				
$4^+ \longrightarrow 2^+$	997^a	-171.8	-100.2	-132	-90	-116	-48
	$1029(15)^b$	-125	-54.2				
	$1036(2)^c$	-123.8	-52.2				

^{a} from Debenham *et al.*, [10],
^{b} from Wimmer *et al.*, [4],
^{c} Current work

$= \beta_{pp}$ - β_{nn}) strength of 300 keV, along with the multipole term, monopole term, and single-particle energy shifts due to the electromagnetic spin-orbit interaction [119]. Further details on the SM calculations can be found in Refs. [119–121] and references therein. Table 5.3 also compares the derived MED and TED values for the 4^+ and 2^+ states from Debenham *et al.*, [10], Wimmer *et al.*, [4], and the current thesis. The values for the theoretical MED and TED are adopted from Ref. [119]. It is found that the magnitude of the MED for the $2^+ \longrightarrow 0^+$ transition from our work agrees better with the theoretical prediction which includes INC. The difference between the proposed energies of the γ rays for ^{70}Kr reported in Ref. [10] and [4] is naturally reflected in the calculated TED and MED. Considering the level energies for the 2^+ state from Ref. [10], one can see that the MED calculation agrees better with the experimental values when the INC interaction is included. Interestingly, for the mass $A = 74$ mirror pair, the agreement between theory and experiment is better without the INC term, see Fig. 4 in Ref. [10]. In the case of TED, for the both $A = 70$ and $A = 74$ triplets agreement between theory and experiment is improved only for the 4^+ states if the INC correction is not applied [10]. The negative trend of the MED for $A = 70$ is explained by the significant spin-orbit contribution in $A = 70$ [119]. The calculated values shown in Table 5.3 indicate that the multipole, monopole, and spin-orbit terms alone are insufficient to explain the experimental observations. The INC interaction is clearly necessary for reproducing the observed TED, as has been observed in the case of the lighter triplets.

The predicted values for TED are much smaller than the experimental data, although they correctly indicate negative spin-dependent trends, as shown in Table 5.3. The negative trends of the TED indicate that the excitation energy of the odd-odd $T = 1$ states must be larger than the average excitation energy of the $T_z = \pm 1$ analogue states. As outlined in Ref. [2], the consistent negativity of TED values stems from their dependence on the isotensor component of the two-body interaction ($V_{pp} + V_{nn} - 2V_{np}$). The decrease in TED with increasing spin can be attributed to two factors: (i) the number of np pairs in a given analogue state is greater in the odd-odd $N = Z$ nucleus compared to the two even-even nuclei (*nn/pp*), and (ii) the positive Coulomb isotensor interaction becomes

weaker relative to the ground state with increasing in spin (J).

6 RECOIL-β TAGGING OF YTTRIUM 78

This chapter presents the experimental results regarding the study of the $N = Z$, ^{78}Y nucleus performed at JYFL-ACCLAB. Transitions assigned to ^{78}Y have been identified using the recoil-β tagging method (RBT). Excited states in ^{78}Y were populated using the fusion-evaporation reaction ^{40}Ca(^{40}Ca, pn), with a beam energy of 120 MeV provided by the K-130 cyclotron and was incident on a ^{nat}Ca target of 0.6 - 0.8-mg.cm^2 thickness, with an average beam intensity of 5 pnA. The experiment was carried out utilising the JUROGAM III γ-ray spectrometer coupled to the vacuum-mode mass separator MARA. The JYU-Tube detector was used at the target position for the detection of the fusion-evaporation charged particles. Other ancillary detectors installed at the MARA focal plane were used for recoil implantation and the subsequent decay detection. The PACE4 calculated cross-section value for the pn channel for this reaction is shown in Table 3.1. The Fermi superallowed β-decay properties of ^{78}Y ($T_{1/2}$ = 55(12) ms and Q_{EC} = 10.54 MeV [122]) allowed for the utilization of the RBT method to associate prompt γ-ray transitions with the implanted ^{78}Y recoils in the DSSSD at the MARA focal plane. The experimental Coulomb energy differences for the $A = 78$ (^{78}Y/^{78}Sr) pair will be compared to $A = 66$, 70 and 74 pairs. In addition, Coulomb energy differences for $A = 78$ will be compared with shell-model calculations.

6.1 Previous experimental results of $N = Z$ nucleus ^{78}Y

The odd-odd ^{78}Y was previously studied using in-beam γ-ray spectroscopy. This experiment utilized the fusion-evaporation reaction ^{40}Ca(^{40}Ca,pn) at JYFL-ACCLAB with beam energies of 118 and 121 MeV [12]. The ^{nat}Ca target was $\sim$1-mg/cm^2 thick. Prompt γ rays originating from the decay of excited states in ^{78}Y were detected using the Jurogam II Ge-array, while most of the unreacted primary beam was separated from the nuclei of interest using the RITU gas-filled recoil separator [116]. At the RITU focal plane, the GREAT spectrometer [123, 124] consisting of a silicon detector (DSSSD), planar germanium (Ge)

detector, and a gas counter was used to detect the incoming reaction products and correlate them with any subsequent radioactive decays. The combination of the DSSSD and planar Ge detectors acted as a ΔE-E telescope for the detection of high-energy β decay events at the focal plane. The γ rays from the pn channel ^{78}Y were identified using the recoil-β tagging (RBT) method (see section 3.7).

Ref. [12] identified three γ-ray transitions originating from the decay of excited states in ^{78}Y with energies of 281, 506, and 615 keV (see Fig. 1 (a) in Ref. [12]). The 281-keV γ ray was assigned as the $2^+ \longrightarrow 0^+$ transition and the 506-keV γ ray was assigned as the $4^+ \longrightarrow 2^+$ transition in ^{78}Y. The γ ray with an energy of 615 keV was not assigned as the $6^+ \longrightarrow 4^+$ transition in the $T = 1$ band of ^{78}Y because this would have resulted in a relatively large negative CED value at the 6^+ state compared to the small positive CED values for the 2^+ and 4^+ states. Such a dramatic change from positive to negative in the CED value has not yet been observed experimentally for the other known cases or from theoretical predictions (see, e.g., Refs. [8, 12, 95, 125, 126] and references therein). It is possible that the 615-keV γ ray may be a transition from a $T = 0$ state to the $T = 1$ band in ^{78}Y.

Another experiment to investigate the excited states in the odd-odd ^{78}Y nucleus was carried out at the National Superconducting Cyclotron Laboratory (NSCL) of the Michigan State University [11, 127]. This experiment employed a ^{92}Mo primary beam that was accelerated by the K500 and K1200 cyclotrons to an energy of 140 MeV/nucleon, as reported in Refs. [11, 127]. The secondary beam was produced via fragmentation on a 802-mg/cm^2 thick ^{9}Be target and consisted of $\sim$ 0.9% ^{81}Zr, $\sim$8.5% ^{80}Y, $\sim$26.8% ^{79}Sr, $\sim$43.3% ^{78}Rb, and $\sim$18.9% ^{77}Kr. The ^{78}Y nuclei were populated through the ^{80}Y secondary beam via the two-neutron knockout reaction on a 188-mg/cm^2 thick ^{9}Be target. The time-of-flight (ToF) and energy-loss measurements were used to separate ^{78}Y from the other knockout reaction products and the secondary beam, with position and angle dependence corrections based on ion-track information from the S800 spectrometer [128]. The Gamma-Ray Energy Tracking In-beam Nuclear Array (GRETINA) [129] was used to detect γ rays from the reaction products at the secondary target position. Details on the experimental procedure can be found in Refs. [11, 127] and references therein. The obtained γ-ray spectrum for ^{78}Y from the NSCL study is shown in Fig. 6.1.

Llewellyn *et al*., assigned the γ rays with energies of 284 and 506 keV as the $2^+ \longrightarrow 0^+$ and $4^+ \longrightarrow 2^+$ transitions in the $T = 1$ band of ^{78}Y, respectively. The energy values for the 2^+ and 4^+ states in the $T = 1$ band of ^{78}Y reported in [11, 127] agrees with the values reported in Ref. [12] within uncertainty values. In addition, three other γ rays with energies of 217, 252, and 559 keV were observed as shown in Fig. 6.1. Due to the low statistics in this experiment, it was unclear whether these γ rays were feeding the 2^+ or 4^+ states in ^{78}Y [11, 127]. However, the clean reaction product identification achieved in the NSCL experiment suggested that the 217-, 252-, and 559-keV γ-ray peaks are genuine decays of excited states in ^{78}Y.

Lastly, Ref. [130] investigated the decay of odd-odd $N = Z$, ^{78}Y nucleus produced in a fusion-evaporation reaction ^{40}Ca(^{40}Ca,pn) at a beam energy of 125 MeV using the ATLAS
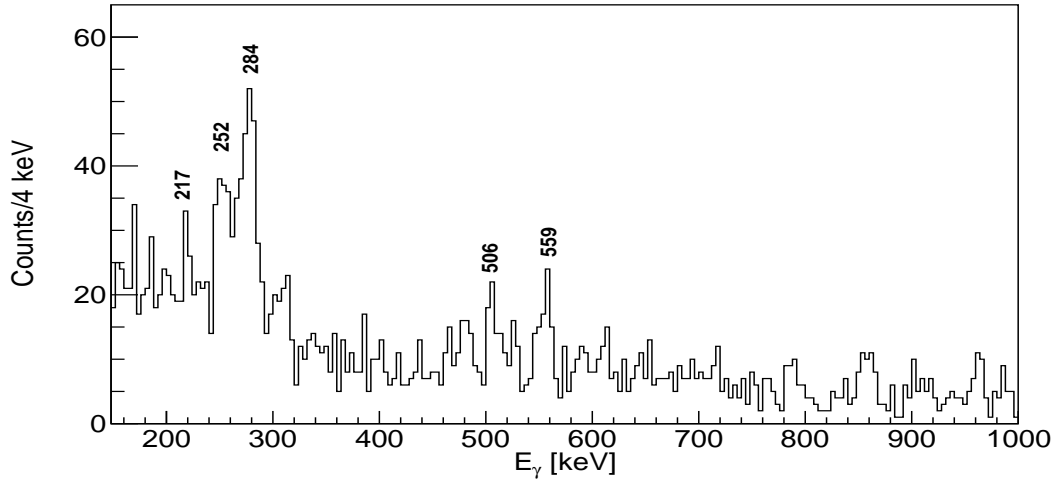
Figure 6.1: The Doppler-corrected γ-ray spectrum for ^{78}Y, corrected with a mid-target recoil velocity of β_{mid} = 0.3 and assuming a mid-target average decay position to enhance any faster decays. The peak at 284 keV is the $2^+ \longrightarrow 0^+$ transition. The 506 keV peak is the $4^+ \longrightarrow 2^+$ transition, while the remaining peaks are unidentified γ rays. This work was carried out at the National Superconducting Cyclotron Laboratory facility at Michigan State University [11, 127].

accelerator at Argonne National Laboratory. Recoiling reaction products were separated by the fragment mass analyzer (FMA) according to their M/Q value before being implanted into the moving tape station. Two large Ge detectors were placed on each side of the tape station for the detection of β-delayed γ rays. The experiment identified a β-decaying isomeric state with a half-life of 5.8(6) s and suggested that this isomeric state is located within 500 keV from the 0^+ ground state of ^{78}Y. Based on the population of the 4^+ and 6^+ levels in the daughter nucleus ^{78}Sr, the isomer was assigned to have spin and parity of 5^+.

6.2 Recoil-β tagging of $N = Z$ nucleus ^{78}Y

In the present work, the search for γ rays originating from ^{78}Y was performed using the recoil-β tagging technique (see details on the RBT method in section 3.7). In addition, $\gamma - \gamma$ coincidence analysis was performed. Figure 6.2 (a) shows recoil-gated and β-decay correlated singles γ-ray spectrum with 500-ms search time, with no conditions on the charged-particle detector, and no β-energy gate. This histogram contains γ rays from the long-lived strong reaction products, which can be removed using more strict β-decay correlation conditions owing to the β-decay properties of ^{78}Y ($T_{1/2}$ = 55(12) ms and Q_{EC} = 10.54 MeV [122]).

Figure 6.2 (b) shows an identical spectrum as panel (a), but with a requirement that one charged-particle is detected in the JYU-Tube detector and with the condition that the β-decay event takes place within 155 ms after the recoil implantation. Figure 6.2 (b) is still dominated by the strong evaporation channels, and there is also substantial contamination from the αpn channel ^{74}Rb, which has a 0^+ ground state that β decays with a half-life
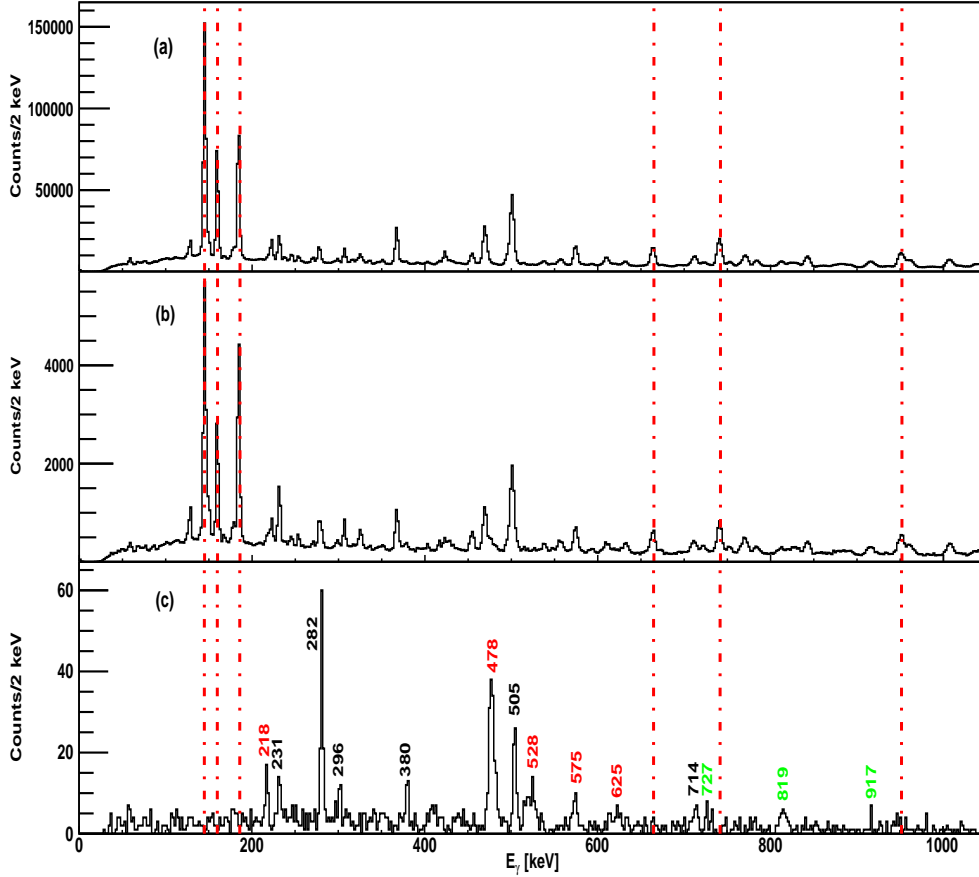
Figure 6.2: Recoil-gated and β-decay correlated γ-ray transitions with (a) 500-ms search time, no conditions on the charged-particle detector, and no β-energy gate. (b) same as (a) but with one charged-particle detected in JYU-Tube and 155-ms search time. (c) same as (b) but with β-energy gate of 5 - 10 MeV. Peaks assigned to ^{78}Y are labelled in black, the source for peaks labelled in **green** is not identified, while the peaks from short lived ^{74}Rb are labelled in **red**. The positions of the peaks originating from the long-lived contaminant nuclei are indicated by dashed **red** lines.

of 65 ms and Q_{EC} of 10 MeV [131, 132]. Figure 6.2 (c) shows the same spectrum as in panel (b), but the β-decay event must have an energy greater than 5 MeV detected in the position-sensitive plastic scintillator behind the DSSSD. The ratio of the 478 keV peak from ^{74}Rb and 282 keV peak from ^{78}Y changes from $\sim$1.75 to $\sim$1.30 from Fig. 6.2 (b) to (c). In addition, the γ rays from the long-live charged-particle channels are basically eliminated. The γ-ray lines from the αpn channel are still present owing to the similar β-decay characteristics of ^{78}Y and ^{74}Rb, and M/Q ambiguity.

In Fig. 6.2 (c), the γ rays with energies of 282, 296, 380, 505, and 714 keV have been assigned to the decays of excited states in ^{78}Y. It is worth noting that the 282- and 505-keV γ rays were previously assigned to the $2^+ \longrightarrow 0^+$ and $4^+ \longrightarrow 2^+$ transitions, respectively [11, 12]. On the other hand, the γ rays with energies of 218, 443, 478, 519, 575, and 625 keV are attributed to the odd-odd ^{74}Rb nucleus, which is visible due to the M/Q overlap and Fermi superallowed β-decay nature [133]. Interestingly, Llewellyn *et al.*, assigned a γ ray with an energy of 217(20) keV to ^{78}Y without providing the state from which this γ ray is decaying [127]. In the present analysis, by placing a γ gate on the
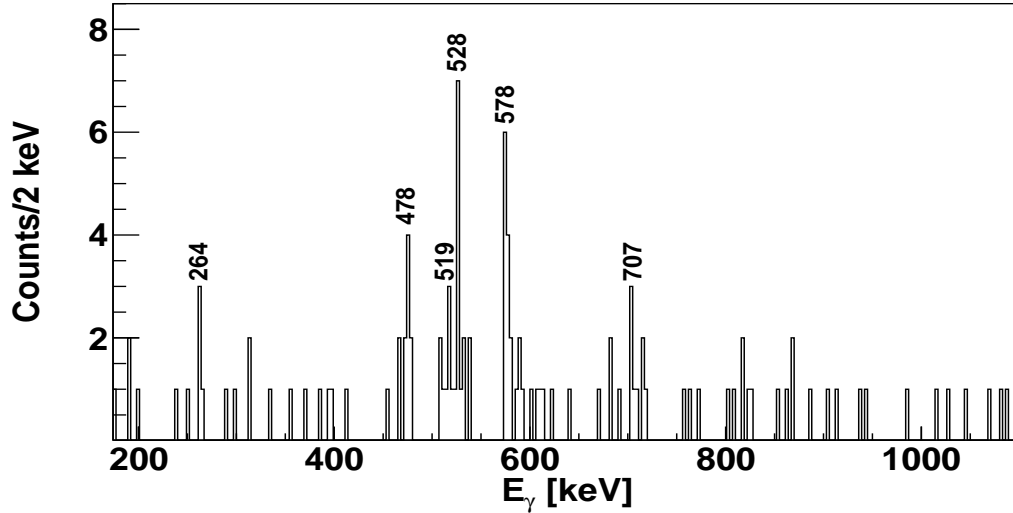
Figure 6.3: Recoil-β tagged and gated $\gamma - \gamma$ coincidence spectrum requiring detection of one charged-particle in JYU-Tube with a γ gate set on 218 keV, with a β-energy gate of 3-10 MeV and using a correlation search time of 155 ms.

218-keV γ-ray transition, coincident transitions from the ^{74}Rb nucleus were observed, as shown in Fig. 6.3. Therefore, the γ ray with an energy of 218 keV in this thesis is assigned as the $4^+ \longrightarrow 3^+$ (between states at 1223 and 1005 keV) transition in ^{74}Rb. Figure 6.4 shows the proposed level scheme for ^{78}Y obtained in the current work.

Figure 6.5 (a) shows a γ gate set on the 282-keV γ ray, confirming coincidence with the previously observed 505-keV γ ray , which is assigned as the $4^+ \longrightarrow 2^+$ transition in the $T = 1$ band in ^{78}Y. The measured R_{DCO} values for the 282- and 505-keV γ rays were 1.34(11) and 1.37(10), respectively, supporting the assignment that these are quadrupole transitions. A γ ray with an energy of 260 keV was also observed in coincidence with the 282-keV γ ray. A 560-keV γ ray was also observed in coincidence with the 282-keV γ ray. This energy is very close to the previously observed 558.6(16)-keV γ ray reported in Ref. [127], suggesting that they may be same γ ray. The level from which the 560-keV γ ray decays is tentatively assigned a spin-parity of 4^+ based on the obtained R_{DCO} value.

In addition, γ rays with energies of 380 and 811 keV are observed in coincidence with the 282-keV γ ray, as shown in Fig. 6.5 (a). The measured R_{DCO} value for the 380-keV γ ray is 1.20(13), which supports an $E2$ character. Therefore, the excited state at 662 keV is tentatively assigned a spin-parity of 4^+. However, due to insufficient statistics, the R_{DCO} value for the 811-keV transition could not be measured.

Figure 6.5 (b) shows four new γ rays that are observed in coincidence with the 505-keV γ-ray transition. These γ rays have energies of 347, 483, 714, and 917 keV. The 483-keV γ ray is suggested to feed the 4^+ state at 787 keV from a tentatively assigned 5^+ state with an energy of 1270 keV, based on the measured R_{DCO} value of 0.69(5). The measured R_{DCO} value for the 714-keV γ ray is 1.19(1) which supports the assignment of the state at 1501 keV as 6^+. The 714-keV γ ray is very close to the energy of the analog $6^+ \longrightarrow$

Figure 6.4: The level scheme of ^{78}Y was derived from the fusion-evaporation reaction ^{40}Ca(^{40}Ca, pn), with a beam energy of 120 MeV. The width of the arrow corresponds to the intensity of the transition. Newly observed levels and γ-ray transition are labelled in **red**. The intensities of the γ-ray transitions observed in the JUROGAM III Ge-array are extracted from recoil-β-tagged γ singles data or γ-γ data with 1-10 MeV β-energy gate (see Table 6.1).

4^+ transition in ^{78}Sr, which supports the $T = 1$, $6^+ \longrightarrow 4^+$ assignment in ^{78}Y for this transition. The 347- and 917-keV γ rays are not seen in the γ gate set on the 282-keV γ ray, therefore they have not been placed placed in the level scheme.

Furthermore, γ rays observed in coincidence with the γ gate set on the 714-keV γ ray provide additional support for its $T = 1$, $6^+ \longrightarrow 4^+$ assignment in ^{78}Y as shown in Fig. 6.5 (c). Specifically, the γ gate set on the 714-keV γ ray shows coincidences with the 505 keV, $4^+ \longrightarrow 2^+$ and 282 keV, $2^+ \longrightarrow 0^+$ transitions, as illustrated in Fig. 6.5 (c). In addition, two new γ rays with energies of 377 and 815 keV are observed in coincidence with the 714-keV γ-ray transition, as shown in in Fig. 6.5 (c). The 377-keV transition was also observed in coincidence with the 505-keV transition, therefore, the 377-keV transition is suggested to feed the tentative 6^+ state at 1501 keV. The observed strong coincidence between the 282- and 380-keV transitions, in addition to the observed shift in energy, imply that the 377- and 380-keV transitions depopulate two different levels in ^{78}Y. Due to limited statistics, the R_{DCO} values for the 377- and 815-keV γ rays could not be measured. Figure 6.5 (d) shows the sum of gates on 282 keV, 505 keV, and 714 keV, the same γ-ray peaks observed in Fig. 6.5 (a), (b), and (c) are seen again. The γ ray with an energy of

Figure 6.5: Recoil-β tagged and gated $\gamma - \gamma$ coincidence spectra requiring detection of one charged-particle in JYU-Tube and 155-ms search time. (a) Gate is set on the 282-keV, $2^+ \longrightarrow 0^+$ γ ray with a β-energy gate of 5 - 10 MeV. (b) Gate is set on the 505-keV, $4^+ \longrightarrow 2^+$ γ ray with a β-energy gate of 4 - 10 MeV. (c) Gate is set on the 714-keV γ ray with a β-energy gate of 3 - 10 MeV. (d) Sum of gates on the 282-, 505-, and 714-keV transitions with a β-energy gate of 5 - 10 MeV. The origin of the γ rays labelled in **green** could not be confirmed in the present analysis.

231 keV is placed as a transition depopulating the 1501 keV, 6^+ state and feeding the 5^+ state at 1270 keV. The relatively weak 231-keV line is seen in the sum-of-gates spectrum of Fig. 6.5 (d), where stronger transition at 483 keV is also seen. The sum of the 231- and 483-keV transitions match the energy difference of the 6^+ and 4^+ states at 1501 and 787 keV, respectively, which supports the current placement of these transitions.

Figure 6.6 (a) shows γ rays in coincidence with the 380-keV γ ray. The observed high intensity of the 282-keV γ ray in Fig. 6.6 (a) suggests that this 380-keV γ-ray transition is feeding the 2^+ state at 282 keV. However, the 505- and 714-keV γ-ray peaks are also observed to be in coincidence with the 380-keV γ ray, as shown in Fig. 6.6 (a). Additionally, by examining the γ gates set on the 505- and 714-keV γ rays, presented in Fig. 6.5 (b) and (c), shows coincidence with a 377-keV γ-ray peak. Therefore, this suggests that the γ gate shown in Fig. 6.6 (a) corresponds to a doublet of the 377- and 380-keV γ rays. Furthermore, γ rays with energies of 231, and 296 keV are observed

Figure 6.6: Recoil-β tagged and gated $\gamma - \gamma$ coincidence spectra requiring detection of one charged-particle in JYU-Tube and using a correlation search time of 155 ms (a) Gate is set on the 380-keV γ ray and the β-energy gate is 3-10 MeV. (b) Gate is set on 296-keV γ ray, with a β-energy gate of 4-10 MeV.

in coincidence with the 377-380-keV gate. Figure 6.6 (b) shows the γ gate set on the γ ray with an energy of 296 keV. The 296-keV γ ray is in coincidence with the 380-keV γ ray and a γ ray with an energy 894 keV. The measured R_{DCO} value of the 380-keV γ ray supports the spin-parity assignment of the state with energy of 662 keV as 4^+. The R_{DCO} values for the 296 and 894 keV could not be determined due to statistical limitations.
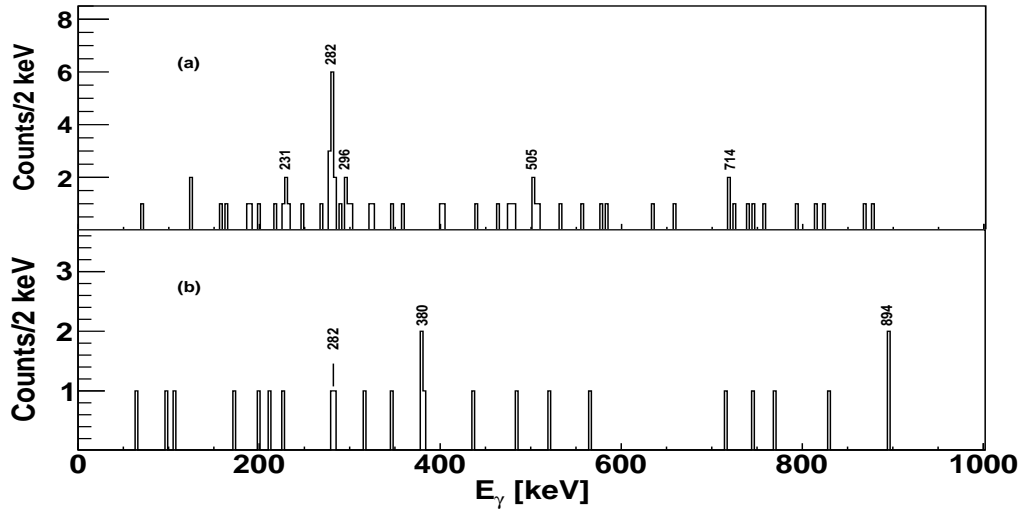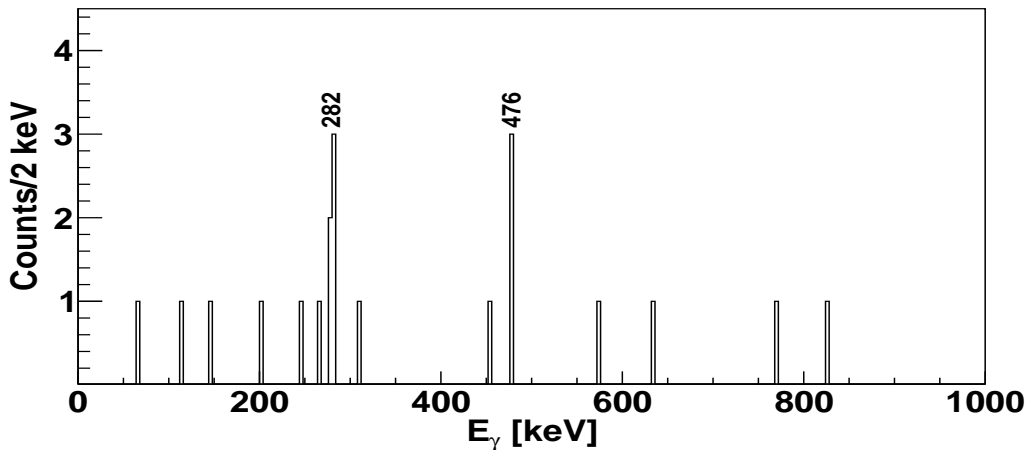

Figure 6.7: Recoil-β tagged and gated $\gamma - \gamma$ coincidence spectrum requiring detection of one charged-particle in JYU-Tube and using a correlation search time of 155 ms. The γ gate is set on the 560-keV γ-ray transition with a β-energy gate of 4-10 MeV.

Figure 6.7 shows γ rays in coincidence with a γ gate set on the 560-keV γ-ray transition. The $2^+ \longrightarrow 0^+$, 282-keV γ-ray transition is observed to be in coincidence with the 560-keV γ ray. In addition, a 476-keV γ ray is also observed in coincidence with the 560-keV γ ray. The measured R_{DCO} value of the 560-keV γ-ray transition is 1.12(13), which

suggests a tentative spin-parity assignment of 4^+ for the state at 842 keV. However, the R_{DCO} value for the 476-keV γ ray could not be measured due to limited statistics. The 476-keV γ-ray transition is proposed to feed the state at 842 keV, which subsequently depopulates to the 2^+ state at 282 keV through the 560-keV γ ray. It is worth noting that there is quite a strong 574-keV γ ray from ^{74}Rb (shown in Fig. 6.4), which is above the 560-keV peak. Therefore, the coincidence between the 560 keV γ ray and the 476-keV γ ray may arise from the Compton background of the 574-keV transition.
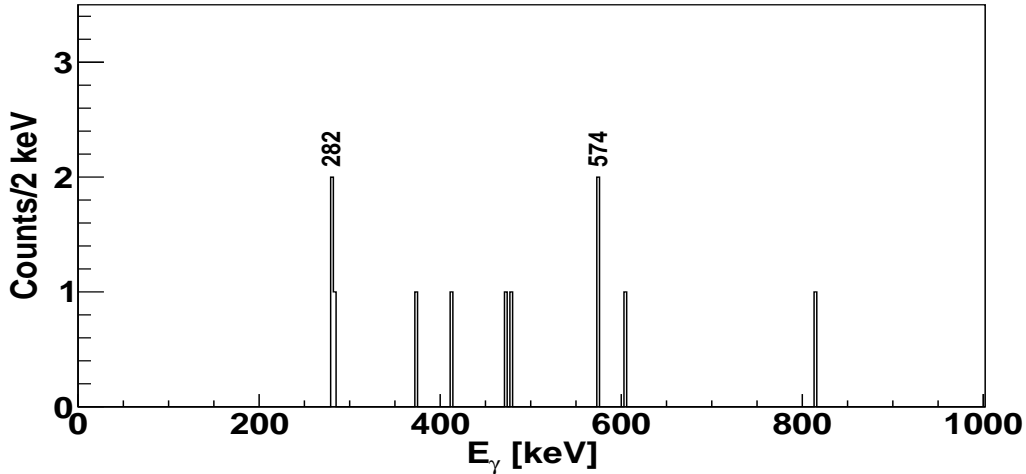
Figure 6.8: Recoil-β tagged and gated $\gamma - \gamma$ coincidence spectrum requiring detection of one charged-particle in JYU-Tube and using a correlation search time of 155 ms. The γ gate is set on the 260-keV γ ray with a β-energy gate of 4-10 MeV.

Figure 6.8 shows the γ rays observed in coincidence with the γ gate set on the 260-keV γ ray. The 282-keV, $2^+ \longrightarrow 0^+$ transition in ^{78}Y and a newly observed 574-keV γ ray are seen to be in coincidence with the 260-keV γ ray. The R_{DCO} values for the newly observed 260- and 574-keV γ-ray transitions could not be measured due to due to statistical limitations, therefore, no spin-parity assignment could be made for the states with energies of 1116 and 542 keV.

The γ ray with energy of 615 keV, reported in Ref. [12] is not observed in the RBT-γ-γ analysis, and the region where this γ ray is expected to be contains some contamination from ^{74}Rb. Table 6.1 presents a comprehensive list of all the observed γ rays associated with ^{78}Y, including their energy levels, spin-parity of the initial and final levels, relative intensity normalized to the $2^+ \longrightarrow 0^+$ transition, and angular distribution ratios, where possible. Based on the $\gamma - \gamma$ analysis a new 6^+ state in the $T = 1$ band in ^{78}Y with an energy of 1501 keV is proposed. Therefore, the $T = 1$ band in ^{78}Y is proposed to have the following transitions 714 keV, $6^+ \longrightarrow 4^+$, 505 keV, $4^+ \longrightarrow 2^+$, and 282 keV, $2^+ \longrightarrow 0^+$. The previously identified 5^+ isomeric state in the odd-odd ^{78}Y nucleus is expected to have an effect on the collected statistics in the present work. It is anticipated that the isomeric state is likely below the 4^+, 787 keV [130], which means that some fraction of the prompt γ-ray intensity (which could not be quantified in the present analysis) has been trapped to the long-lived isomeric 5^+ state. If the isomer β-decays with high Q_{EC} value, then, in

principle, it would be possible to correlate the ^{78}Y recoils with high-energy β particles, but with long correlation search time. This would allow to see the band structure above the isomer. However, in order to do this the DSSSD counting rate should be very low to minimize random correlations. The R_{DCO} results for the measured γ rays are shown in Fig. 6.9.
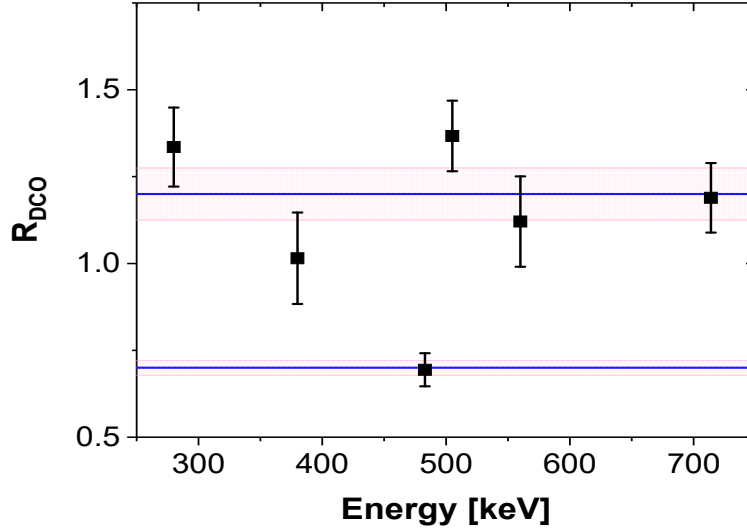
Figure 6.9: Measured R_{DCO} values for selected transitions from ^{78}Y. The **blue** lines (pink lines are the errors) shows the average R_{DCO} of 1.2(1) and 0.70(2) for quadrupole and dipole transitions, respectively, measured from the 2p and 3p channel ^{78}Sr and ^{77}Rb, respectively.

6.3   Coulomb energy differences for $A = 78$

Figure 6.10 shows the Coulomb energy differences (CED) for mass number 66 [8], 70 (present study, chapter 5), 74 [134], and 78 (current chapter). In the recent years, CED across the sd and fp shells have been extensively studied − this data has been analyzed through the use of large-scale SM calculations [2, 98, 135–137]. The newly obtained CEDs for $A = 78$ provide further testing grounds for the effective nuclear interactions in SM calculations. These calculations comprise of Coulomb force (V_{CM}), electromagnetic spin-orbit term (ϵ_{ls}), single-particle correction (ϵ_{ll}) term, and radial term (V_{Cr}). However, in SM calculations, it has been suggested that the V_{Cr} term is not required for a good description of the lower part of the fp shell, and it only becomes important for high angular momentum states [138, 139]. The CED exhibits a smooth rise to the highest observed state for $A = 66$, whereas for $A = 74$ and 78, there is a significant positive trend and almost near zero trend, respectively. Interestingly, the CED for mass $A = 70$ is uniquely negative, and this effect is not fully understood. Possible explanations for this phenomenon were discussed in section 5.4.

The SM calculations performed in $p_{3/2}, f_{5/2}, g_{9/2}$ model space for the odd-odd $N = Z$,

Table 6.1: The prompt γ-ray transitions measured for ^{78}Y in the present work. The energy of the γ ray (E$_\gamma$), relative γ-ray intensity (I) normalized to the $2^+ \longrightarrow 0^+$ transition, initial level energy (E$_i$), final level energy (E$_f$), assigned spin and parity of the initial and final levels (I_i^π and I_f^π) and angular distribution information (R$_{DCO}$) are listed.

E [keV]	I [%]	E$_i$ [keV]	E$_f$ [keV]	I_i^π	I_f^π	R$_{DCO}$
232(1)	1.3	1501	1270	(6^+)	(5^+)	
260(1)	2.9	542	282		2^+	
282(1)	100	282	0	2^+	0^+	$1.34(11)^a$
290(1)	7.6	958	662			
377(1.2)	<10	1878	1501		(6^+)	
380(1.2)	35.5	662	282	(4^+)	2^+	$1.02(13)^b$
476(1)	<10	1318	842			
483(1.2)	7.4	1270	787	(5^+)	4^+	$0.69(5)^a$
505(1)	89.7	787	282	4^+	2^+	$1.37(10)^a$
560(1)	5.0	842	282	(6^+)	2^+	$1.12(13)^b$
574(1)	4.4	1116	542			
714(1)	4.4	1501	787	(6^+)	4^+	$1.19(1)^a$
811(2)	5.3	1093	282		2^+	
815(2)	3.7	2316	1501		(6^+)	
894(2)	6.3	1852	958			

^{a} Sum gate on 282 and 505 keV. ^{b} Gate on 282

^{78}Y [19] can reproduce the experimentally observed CED trend, shown in Fig. 6.10 (b). The spin-orbit interaction (ϵ_{ls}) term in the SM calculations [19] is negative for the $A = 66$, 70 and 74 pairs [19]. The $A = 78$ pair has the least negative ϵ_{ls} values in this mass region [19]. The ϵ_{ls} term can have opposite signs in certain situations, depending on how the proton or neutron orbits are oriented. In addition, the spin-orbit coupling influences signs ($\pm$), for example, $< \vec{l} \cdot \vec{s} >= l/2$ when $j = l + s$ and $< \vec{l} \cdot \vec{s} >= -(l+1)/2$ when $j = l - s$ in Eq. 2.7. These factors strongly influence the results shown in Fig. 3 of Ref. [19] and Fig. 6.10 (b). The Coulomb multipole (V_{CM}) term is always positive. The positive trend is due to the effect of the overlap of the proton-proton pairs' wavefunctions. The calculated CED that includes the combined $V_{CM+ls+ll}$ term by Kaneko *et al.*, correctly predicts the CED value for the $J^\pi = 2^+$ state in $A = 78$, as shown in Fig. 6.10 (b). The agreement between theory and experiment worsens for the 4^+ and 6^+ states, which might warrant further theoretical investigations to interpret this difference. It should be noted that the calculations presented in Ref. [19] do not use the schematic INC interaction. It was later adopted in Ref. [119], but the CED prediction for the $A = 78$ pair worsens further in comparison to the experimental values (see Fig. 3 in Ref. [119]).

The V_{CM} term plays a vital role in shell-model CED calculations as, in the hypothesis of
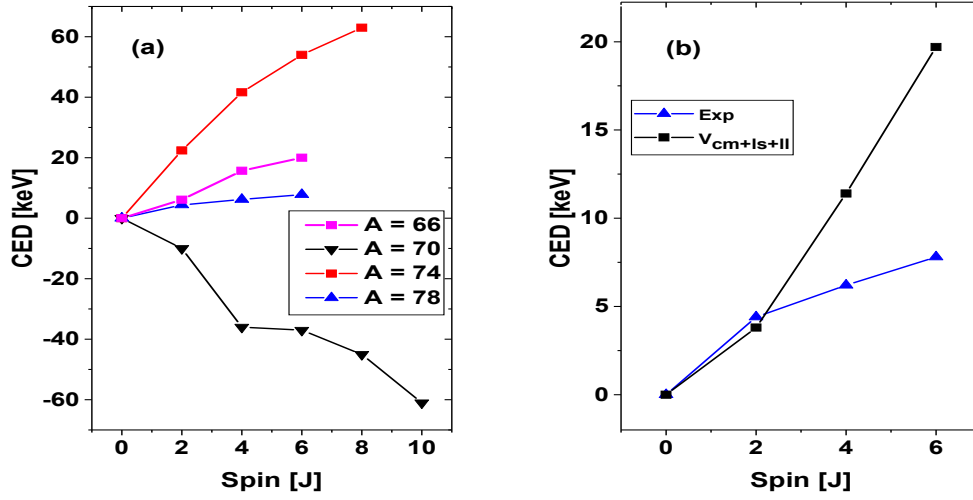
Figure 6.10: (a) Coulomb energy differences (CED) between $T_z = (0, 1)$ pairs as a function of spin (J) for the cases $A = 66, 70, 74$, and 78. Data for $A = 74$ was taken from Ref. [133]. Furthermore, data for $A = 70$ and 78 are from the current work. (b) CED for $A = 78$ (current work) compared to SM calculated CED values without the INC term calculated by Kaneko *et al.*, [19].

isospin, differences in excitation energy between analogue states in nuclei should be purely electromagnetic. However, it produces inaccurate results without the additional terms, as most notably observed in the case of the $A = 70$ pair (see Fig. 3 in Ref. [19]). Nevertheless, interpreting the CED and MED in the $A = 70$ mass region and above poses challenges for the shell model as the size of the valence space increases, in addition to the potential effects caused by the rapid shape evolution. The SM calculations for the $A = 78$ pair are particularly difficult due to the size of the valence space involved and the need to include $pfgd$ orbitals. A possible explanation for the observed modest CED trend for the $A = 78$ pair has been speculated to result from a deformed shell gap at $N = Z = 38$ [12, 140]. Stable prolate-deformed nuclei are located in the vicinity of $A \simeq 80$ (see Fig. 4.11). The shapes of these nuclei are stabilized due to the presence of a gap in the single-particle energy sequence at $N = Z = 38$, which is large enough to inhibit any scattering across the Fermi surface. As a result, for example odd-A nuclei in this region exhibit near rigid-rotor behavior with stable shapes and reduced pairing effects [141]. As discussed earlier, the shape evolution was suggested to be the origin for the negative CED for the $A = 70$ pair. However, the recent experimental and theoretical works suggested similar stable shapes for the low-spin states in ^{70}Br and ^{70}Se. Therefore, the stable shape arguments suggested for the nearly flat CED behavior for the mass $A = 78$ pair do not seem sufficient. Moreover, when considering the CED trends for the $A = 74$ (large positive) and $A = 66$ (moderately positive) pairs, it is clear that more theoretical work is required to reach comprehensive understanding on the CED evolution for these nuclei.

7 SUMMARY, AND FUTURE PROSPECTS

This thesis presented results from three experiments conducted using the MARA vacuum-mode recoil separator coupled to the Jurogram III Ge-array and other ancillary instruments. These experiments were performed at JYFL-ACCLAB and the aim was to study nuclei at or close to the $N = Z$ region between mass number 70 and 84. The results presented in this thesis provide experimental insight into the much debated proton-neutron pairing correlations and isospin symmetry-breaking mechanisms in this region.

7.1 Molybdenum 84

The γ-ray spectroscopy experiment on ^{84}Mo presented in this thesis confirmed the γ-ray transitions up to the $J^{\pi} = 6^+$ state. The data from the experiment may have contained γ-ray transitions above the $J^{\pi} = 6^+$ state from ^{84}Mo. However, the inability to separate ^{81}Y, ^{83}Y, and ^{84}Zr from ^{84}Mo made it challenging to confirm transitions above the $J^{\pi} = 6^+$ state. The ability for Z identification using, e.g., ionization chamber at the MARA focal plane would improve the experimental sensitivity. The same inverse kinematics reaction i.e. ^{58}Ni + ^{28}Si used in the current work should be employed to populate ^{84}Mo via the 2n channel. The Z identification method in conjugation with a recoil separator was previously used in the study of $N = Z$ ^{80}Zr. Figure 1 in Ref. [85] shows the distribution of ^{80}Sr, ^{80}Y, and ^{80}Zr ions, the ^{80}Zr/^{80}Y intensity ratio was found to increase by a factor of 3 in regions dominated by ^{80}Zr in the ionization chamber. However, Ref. [85] is over three decades old. With improved modern technology and with the use of JYU-Tube (see section 3.2.3.1), it should be possible to reach sufficient Z sensitivity for ^{84}Mo. Currently, an ionization chamber for the MARA focal plane is being designed in collaboration with the UK institutes.

Section 4.3 presented the systematics of the excited states in $N = Z$ nuclei between ^{60}Zn and ^{88}Ru. The energies for the (8^+) and (10^+) states in ^{84}Mo were tentatively assigned

by Ref. [76]. The systematics indicate an increase in collectivity towards the strongly deformed nuclei at $N = Z = 38$ and moderate decrease in collectivity towards the heavier $N = Z$ nucleus ^{88}Ru. The predictions by Möller *et al.*, [82] suggest that the ^{84}Mo nucleus is well deformed. However, the calculated $E(4)^+/E(2^+)$ ratio for ^{84}Mo is 2.52 which is less than the expected value for a good rotor. This suggests the presence of (shape) mixing in $N = Z$, ^{84}Mo.

The nuclear force is expected to be stronger for the isoscalar neutron-proton pairs than for the isovector neutron-proton pairs. The existence of the deuteron with ground state spin $I = 1$ and the unbound nature of two-proton and two-neutron systems reveal that the $T = 0$, $I = 1$ correlation is more robust than $T = 1$, $I = 0$ correlation. However, Ref. [34] suggests that the spin-orbit term reduces the probability of the isoscalar pairing forming such a condensate with increasing mass. Despite this, the spectroscopy of $N = Z$ nuclei provides an exciting opportunity to search for the experimental signatures of the isoscalar neutron-proton pairing. For example, the observed smooth rotational response seen in $N = Z$ nuclei compared to the $N = Z + 2$ and $N = Z + 4$ nuclei has been debated to result from enhanced isoscalar neutron-proton correlations. According to Ref [29], the delayed or absent backbending behavior observed in $N = Z$ nuclei can be attributed to the presence of $T = 0$ isoscalar pairing. While $N = Z$ nuclei exhibit smoother behavior compared to their heavier even-even isotopes, backbending has been observed in the case of ^{76}Sr. This finding raises the question of whether isoscalar $T = 0$ pairing influences the observed moments of inertia for the other $N = Z$ nuclei in this mass region. Ref [34] suggests that including the isoscalar $T = 0$ pairing is not needed to reproduce the rotational response of $N = Z$ nuclei. Nonetheless, experimental observations of higher spins in the yrast bands are needed to reach a definitive conclusion on the absence or delay of backbending in the even-even $N = Z$, $A > 76$ nuclei.

As an alternative approach, the current thesis explored the role of deformation as a potential source for the observed delayed backbendings in the $N = Z$ nuclei. Figure 4.13 (a) suggests that ^{76}Sr has a nearly similar level of deformation compared to ^{78}Sr and ^{80}Sr, while Figs. 4.13 (b)-(d) suggests that $N = Z$ nuclei are more deformed than their $N = Z + 2$ and $N = Z + 4$ neighbors. Figures 4.13 and 4.12 suggest that deformation influences the point at which the critical crossing frequency between aligned and ground state bands occurs. However, this does not rule out the role of isoscalar $T = 0$ pairing in the observed rotational response of $N = Z$ nuclei.

Lastly, the current work confirms the delayed backbending previously observed in $N = Z$, ^{84}Mo nucleus compared to $N = Z + 2$ and $N = Z + 4$ nuclei. The moment of inertia of the yrast band in the even-even $N = Z$, ^{84}Mo shows a gradual change in its behavior until it reaches the experimentally observed rotational frequency limit of 0.6 MeV. In addition, the critical rotational frequency for backbending was observed to reduce with reduced deformation in $N = Z + 2$ and $N = Z + 4$ nuclei. This delay in the backbending compared to the $N > Z$ isotopes indicates a need for further critical investigation of the role of the isoscalar proton-neutron correlations in $N = Z$ nuclei such as ^{80}Zr, ^{84}Mo, and ^{88}Ru. Experimental observations of the states at higher spin in the yrast bands are required to make a definitive conclusion.

7.2 Mass 70 nuclei

The current work has implemented the recoil-β tagging (RBT) and recoil-double-β tagging techniques (RDBT) for the first time to study the Fermi superallowed β decaying nuclei ^{70}Br and ^{70}Kr, respectively. The correlation of high-energy β decay events to recoils, associated with a specific number of evaporated particles, and within a short correlation search time in this experiment allowed for the identification and assignment of γ rays originating from the decay of excited states in ^{70}Br and ^{70}Kr.

In this thesis, the observations of multiple γ-ray transitions was made using the RBT-$\gamma - \gamma$ coincidence data obtained from the fusion-evaporation reaction ^{40}Ca(^{32}S,pn)^{70}Br. The assigned parities and spins of the observed excited states were based, when possible, on the measured R_{DCO} values of γ rays originating from ^{70}Br. A new bandhead was proposed with a tentative spin-parity of 4^+ and an excitation energy of 1933 keV. The γ ray feeding the state at 1933 keV was previously observed in Ref. [95]. Additionally, three new γ rays were observed in this band, feeding the states with energies of 2678 keV, 6^+ and 3148 keV, (8^+). The 4^+ state with the energy of 1933 keV decays to the 3^+ state and 2^+ state in the $T = 1$ band. The band built on the $J^\pi = 3^+$, 1337-keV state was reported in prior studies (see Refs. [95, 97]). In the current thesis, the spin-parity of the state at 3681 keV was reassigned to 9^+ based on the measured R_{DCO} of the 998-keV γ-ray transition. The excitation energy of the state decaying to the 10^+ state at 4446 keV was revised to be 5784 keV, but the tentative spin-parity of 12^+ remains unchanged.

The low-spin structure of the $T = 1$ band below $J^\pi = 4^+$ for ^{70}Br described in this thesis is almost identical to that proposed by de Angelis *et al*., and Jenkins *et al*.,. In the current work, a γ-ray with an energy of 963 keV was observed to be feeding the 4^+ state at 2003 keV in the $T = 1$ band. The 963-keV γ ray was previously observed by de Angelis *et al*., [95]. In addition, two more γ rays were observed in coincidence with the 963-keV γ-ray with energies of 1027 and 1151 keV. The R_{DCO} values for the γ rays with energies of 963, 1027, and 1151 keV could not be extracted due to insufficient statistics. Therefore, these transitions have been tentatively assigned to the $T = 1$ band in ^{70}Br. Therefore, a band built on the $T = 1$, 0^+ ground state containing the following γ-ray transitions, 934 keV ($2^+ \longrightarrow 0^+$), 1069 keV ($4^+ \longrightarrow 2^+$), 963keV ($6^+ \longrightarrow 4^+$), 1027 keV ($8^+ \longrightarrow 6^+$), and 1151 keV ($10^+ \longrightarrow 8^+$) is proposed to form a cascade in the $T = 1$ band in ^{70}Br.

The shell-model calculations performed in this thesis accurately depict the excitation energies of the low-lying states in ^{70}Br and ^{70}Se. However, the calculations fail to reproduce the energy of the 10^+ state at 5144 keV in ^{70}Br, highlighting limitations in the effective interactions utilized. The comparison between SM calculations and experimental data suggests that the $f_{5/2}, p_{1/2}, g_{9/2}$ model space is enough to characterize the low-energy structure of ^{70}Br and ^{70}Se. The calculated spectroscopic quadrupole moments for ^{70}Br and ^{70}Se indicate that the proposed $T = 1$ band in ^{70}Br is similar to the well-known $T = 1$ band in ^{70}Se. In addition, the predicted spectroscopic quadrupole moments show a shift from oblate to prolate deformation in the $T = 1$ band at $I^\pi = 8^+$ in ^{70}Br and ^{70}Se.

The SM calculations performed in this study reproduce similar negative CED trend as observed experimentally, but the magnitude of the calculated CED is significantly overestimated. However, the predictions by Kaneko *et al* reproduce reasonably well the CED for $A = 70$. As said, the CEDs between isobaric analogue states in ^{70}Br and ^{70}Se are negative. Several suggestions have been proposed to explain this. It was suggested that the negative CED trend is due to the increased proton radii of dripline nuclei, which lead to the reduction of Coulomb repulsion due to the spatial extension of the proton wave functions. However, this explanation fails to account for the positive CED observed in the other systems in this mass region. Ref. [19] concludes that the unique negative trend of the CED is due to the large spin-orbit component for $A = 70$ and shape variation do not play an important part. Further theoretical studies are encouraged to be performed to identify the source responsible for the magnitude of the CED in this mass region and to refine our understanding of the nuclear structure and dynamics in this regime.

Based on the RDBT method, the γ-ray with an energy of 881 keV was assigned as the $2^+ \longrightarrow 0^+$ transition in ^{70}Kr. The 1036-keV γ ray has tentatively been assigned as the $4^+ \longrightarrow 2^+$ transition in ^{70}Kr. Previous experiments to study the excited states in ^{70}Kr were carried out at RIKEN [4] and at JYFL-ACCLAB [10]. The $2^+ \longrightarrow 0^+$ transition in ^{70}Kr identified in the RIKEN study agrees well with the current observation. In addition, the $4^+ \longrightarrow 2^+$, 1036 keV candidate transition observed in the present work agrees with the value obtained at RIKEN. Furthermore, the comparison to the mirror nucleus ^{70}Se provides supporting evidence for the assigned spin and parity values of the 2^+ state with an energy of 881 keV, and for the tentative 4^+ state with an energy of 1917 keV.

The obtained excitation energies of the 4^+ and 2^+ states in ^{70}Kr were used to calculate the MED and TED for the $A = 70$ triplet. The magnitudes of the newly calculated MED for the $2^+ \longrightarrow 0^+$ and $4^+ \longrightarrow 2^+$ transitions align well with theoretical predictions that include the INC interaction. However, the magnitudes of the suggested $2^+ \longrightarrow 0^+$ transition from Ref. [10] and the $4^+ \longrightarrow 2^+$ transition from Ref. [4] have better agreement with the theoretical MED predictions that include INC interaction. The spin alignment is expected to affect the magnitude of the MED, as it increases the spatial separation of protons in the $g_{9/2}$ orbit, leading to a smaller Coulomb energy. As a result, the alignment effect for protons lowers the excitation energy at high angular momentum especially in the proton-rich member of the triplet. The V_{CM}, ϵ_{ls}, and ϵ_{ll} are the primary factors contributing to the MED. The V_{cr} term is anticipated to play a significant role in the MED at high spin due to the increased presence of the $g_{9/2}$ orbit. However, the contribution from the ϵ_{ls} term to the MED is significantly negative at high spin. At low spin, the V_{CM}, ϵ_{ls}, ϵ_{ll} terms determine the magnitude of the MED, while the V_{cr} contribution is low. Lastly, an inclusion of a schematic INC interaction in the shell model calculations is required to match the experimental MED and TED systematics. The requirement for an additional INC interaction has also been established in the context of triplets in the $f_{7/2}$ shell [7]. Further theoretical studies are required to uncover the source of the missing TED magnitude in this mass region.

7.3 Yttrium 78

The ^{78}Y nucleus holds significant importance in nuclear structure physics as it provides a unique opportunity to investigate the breaking of isospin symmetry in the $A = 78$ nuclei. The current work studied the excited states in the odd-odd ^{78}Y using the fusion-evaporation reaction ^{40}Ca(^{40}Ca, pn), with a beam energy of 120 MeV. The experiment utilized the RBT method and led to the observation of several new γ-ray transitions from the decay of excited states in ^{78}Y. A new $J^{\pi} = 6^+$ excited state is proposed with an energy of 1501 keV in the $T = 1$ band in ^{78}Y, that decays to the $J^{\pi} = 4^+$ state with an energy of 714 keV.

Several new transitions and excited states have been observed, and where possible, their spin-parity was determined. Among these transitions, a previously unobserved excited state with an energy of 1270 keV was observed and tentatively assigned a spin-parity of 5^+. The 5^+ state is populated through a dipole transition from the 6^+ state in the $T = 1$ band, and it subsequently decays to the 4^+ state in the same $T = 1$ band. Additionally, two new excited states were observed that feed the 2^+ state in the $T = 1$ band of ^{78}Y. These states were tentatively assigned a spin-parity of 4^+. The first 4^+ state has an excitation energy of 662 keV, and it is fed by a cascade of two γ rays with energies of 296 keV and 894 keV. The second 4^+ state has an excitation energy of 842 keV, and only one γ ray with an energy of 476 keV was observed feeding this state.

The SM calculation that includes V_{CM}, ϵ_{ls}, ϵ_{ll} terms satisfactorily reproduce the experimental CED as shown in Fig. 6.10. In particular, the CED for the $J^{\pi} = 2^+$ state in ^{78}Y is correctly predicted. The $J^{\pi} = 4^+$ and $J^{\pi} = 6^+$ states are also reproduced relatively well compared to experimental data with differences of 5.2 and 12 keV, respectively. A possible explanation for the observed CED trends in ^{78}Y- ^{78}Sr may be due to the increased collectivity in the region [11, 12]. The low excitation energy of the $T = 1$, 2^+ states in ^{78}Y- ^{78}Sr suggests that these nuclei are strongly deformed. Thus it is expected that these nuclei will have stable shapes, and will appear as near rigid rotors. Therefore all paring effects are reduced in this pair and results in near zero trends of the CED. In SM calculations for nuclei beyond the $N = Z$, ^{72}Kr, it is essential to include the $d_{5/2}$ orbital to predict CED trends accurately. However, due to the increased size of the valence space, calculations become computationally demanding and time consuming. Perhaps, a way forward to investigate CED in this mass region is to pursue towards calculations using density functional theory, as performed in Ref. [11].

REFERENCES

[1] B. Cederwall, F. G. Moradi, T. Bäck, A. Johnson, J. Blomqvist, E. Clément, G. de France, R. Wadsworth, K. Andgren, K. Lagergren, A. Dijon, G. Jaworski, R. Liotta, C. Qi, B. M. Nyakó, J. Nyberg, M. Palacz, H. Al-Azri, A. Algora, G. de Angelis and S. Williams. *Nature*, **469**, 68 (2011). . URL https://doi.org/10.1038/nature09644.

[2] M. Bentley and S. Lenzi. *Progress in Particle and Nuclear Physics*, **59**, 497 (2007). ISSN 0146-6410. . URL https://www.sciencedirect.com/science/article/pii/S0146641006000743.

[3] H. Iwasaki, A. Lemasson, C. Morse, A. Dewald, T. Braunroth, V. M. Bader, T. Baugher, D. Bazin, J. S. Berryman, C. M. Campbell, A. Gade, C. Langer, I. Y. Lee, C. Loelius, E. Lunderberg, F. Recchia, D. Smalley, S. R. Stroberg, R. Wadsworth, C. Walz, D. Weisshaar, A. Westerberg, K. Whitmore and K. Wimmer. *Phys. Rev. Lett.*, **112**, 142502 (2014). . URL https://link.aps.org/doi/10.1103/PhysRevLett.112.142502.

[4] K. Wimmer, W. Korten, T. Arici, P. Doornenbal, P. Aguilera, A. Algora, T. Ando, H. Baba, B. Blank, A. Boso, S. Chen, A. Corsi, P. Davies, G. de Angelis, G. de France, D. Doherty, J. Gerl, R. Gernhäuser, D. Jenkins, S. Koyama, T. Motobayashi, S. Nagamine, M. Niikura, A. Obertelli, D. Lubos, B. Rubio, E. Sahin, T. Saito, H. Sakurai, L. Sinclair, D. Steppenbeck, R. Taniuchi, R. Wadsworth and M. Zielinska. *Physics Letters B*, **785**, 441 (2018). ISSN 0370-2693. . URL https://www.sciencedirect.com/science/article/pii/S0370269318306427.

[5] K. Wimmer, T. Arici, W. Korten, P. Doornenbal, J.-P. Delaroche, M. Girod, J. Libert, T. R. Rodríguez, P. Aguilera, A. Algora, T. Ando, H. Baba, B. Blank, A. Boso, S. Chen, A. Corsi, P. Davies, G. de Angelis, G. de France, D. T. Doherty, J. Gerl, R. Gernhäuser, T. Goigoux, D. Jenkins, G. Kiss, S. Koyama, T. Motobayashi, S. Nagamine, M. Niikura, S. Nishimura, A. Obertelli, D. Lubos, V. H. Phong, B. Rubio, E. Sahin, T. Y. Saito, H. Sakurai, L. Sinclair, D. Steppenbeck, R. Taniuchi, V. Vaquero, R. Wadsworth, J. Wu and M. Zielinska. *Eur. Phys. J. A.*, **56**, 159 (2020). . URL https://doi.org/10.1140/epja/s10050-020-00171-3.

[6] K. Wimmer, W. Korten, P. Doornenbal, T. Arici, P. Aguilera, A. Algora, T. Ando, H. Baba, B. Blank, A. Boso, S. Chen, A. Corsi, P. Davies, G. de Angelis, G. de France, J.-P. Delaroche, D. T. Doherty, J. Gerl, R. Gernhäuser, M. Girod, D. Jenkins, S. Koyama, T. Motobayashi, S. Nagamine, M. Niikura, A. Obertelli, J. Libert, D. Lubos, T. R. Rodríguez, B. Rubio, E. Sahin, T. Y. Saito, H. Sakurai, L. Sinclair, D. Steppenbeck, R. Taniuchi, R. Wadsworth and M. Zielinska. *Phys. Rev. Lett.*, **126**, 072501 (2021). . URL https://link.aps.org/doi/10.1103/PhysRevLett.126.072501.

[7] P. Ruotsalainen, D. G. Jenkins, M. A. Bentley, R. Wadsworth, C. Scholey, K. Auranen, P. J. Davies, T. Grahn, P. T. Greenlees, J. Henderson, A. Herzáň, U. Jakobsson, P. Joshi, R. Julin, S. Juutinen, J. Konki, M. Leino, G. Lotay, A. J. Nichols, A. Obertelli, J. Pakarinen, J. Partanen, P. Peura, P. Rahkila, M. Sandzelius, J. Sarén, J. Sorri, S. Stolze and J. Uusitalo. *Phys. Rev. C*, **88**, 041308 (2013). . URL https://link.aps.org/doi/10.1103/PhysRevC.88.041308.

[8] P. Ruotsalainen, C. Scholey, R. Julin, K. Hauschild, K. Kaneko, B. S. Nara Singh, R. Wadsworth, D. G. Jenkins, T. S. Brock, P. T. Greenlees, J. Henderson, U. Jakobsson, P. Jones, S. Juutinen, S. Ketelhut, M. Leino, N. M. Lumley, P. J. R. Mason, P. Nieminen, M. Nyman, I. Paterson, P. Peura, M. G. Procter, P. Rahkila, J. Sarén, J. Sorri and J. Uusitalo. *Phys. Rev. C*, **88**, 024320 (2013). . URL https://link.aps.org/doi/10.1103/PhysRevC.88.024320.

[9] J. Henderson, D. G. Jenkins, K. Kaneko, P. Ruotsalainen, P. Sarriguren, K. Auranen, M. A. Bentley, P. J. Davies, A. Görgen, T. Grahn, P. T. Greenlees, A. Hay, T. W. Henry, A. Herzáň, U. Jakobsson, R. Julin, S. Juutinen, J. Konki, M. Leino, C. Mc-Peake, S. Milne, A. J. Nichols, J. Pakarinen, P. Papadakis, J. Partanen, P. Peura, P. Rahkila, E. Sahin, M. Sandzelius, J. Sarén, C. Scholey, M. Siciliano, L. Sinclair, J. Sorri, S. Stolze, J. Uusitalo, R. Wadsworth and M. Zielińska. *Phys. Rev. C*, **90**, 051303 (2014). . URL https://link.aps.org/doi/10.1103/PhysRevC.90.051303.

[10] D. M. Debenham, M. A. Bentley, P. J. Davies, T. Haylett, D. G. Jenkins, P. Joshi, L. F. Sinclair, R. Wadsworth, P. Ruotsalainen, J. Henderson, K. Kaneko, K. Auranen, H. Badran, T. Grahn, P. Greenlees, A. Herzaáň, U. Jakobsson, J. Konki, R. Julin, S. Juutinen, M. Leino, J. Sorri, J. Pakarinen, P. Papadakis, P. Peura, J. Partanen, P. Rahkila, M. Sandzelius, J. Sarén, C. Scholey, S. Stolze, J. Uusitalo, H. M. David, G. de Angelis, W. Korten, G. Lotay, M. Mallaburn and E. Sahin. *Phys. Rev. C*, **94**, 054311 (2016). . URL https://link.aps.org/doi/10.1103/PhysRevC.94.054311.

[11] R. D. O. Llewellyn, M. A. Bentley, R. Wadsworth, H. Iwasaki, J. Dobaczewski, G. de Angelis, J. Ash, D. Bazin, P. C. Bender, B. Cederwall, B. P. Crider, M. Doncel, R. Elder, B. Elman, A. Gade, M. Grinder, T. Haylett, D. G. Jenkins, I. Y. Lee, B. Longfellow, E. Lunderberg, T. Mijatović, S. A. Milne, D. Muir, A. Pastore, D. Rhodes and D. Weisshaar. *Phys. Rev. Lett.*, **124**, 152501 (2020). . URL https://link.aps.org/doi/10.1103/PhysRevLett.124.152501.

[12] B. S. Nara Singh, A. N. Steer, D. G. Jenkins, R. Wadsworth, M. A. Bentley, P. J. Davies, R. Glover, N. S. Pattabiraman, C. J. Lister, T. Grahn, P. T. Greenlees, P. Jones, R. Julin, S. Juutinen, M. Leino, M. Nyman, J. Pakarinen, P. Rahkila, J. Sarén, C. Scholey, J. Sorri, J. Uusitalo, P. A. Butler, M. Dimmock, D. T. Joss, J. Thomson, B. Cederwall, B. Hadinia and M. Sandzelius. *Phys. Rev. C*, **75**, 061301 (2007). . URL https://link.aps.org/doi/10.1103/PhysRevC.75.061301.

[13] A. Nichols, R. Wadsworth, H. Iwasaki, K. Kaneko, A. Lemasson, G. de Angelis, V. Bader, T. Baugher, D. Bazin, M. Bentley, J. Berryman, T. Braunroth, P. Davies, A. Dewald, C. Fransen, A. Gade, M. Hackstein, J. Henderson, D. Jenkins, D. Miller,

C. Morse, I. Paterson, E. Simpson, S. Stroberg, D. Weisshaar, K. Whitmore and K. Wimmer. *Physics Letters B*, **733**, 52 (2014). ISSN 0370-2693. . URL https://www.sciencedirect.com/science/article/pii/S0370269314002482.

[14] A. Boso, S. Milne, M. Bentley, F. Recchia, S. Lenzi, D. Rudolph, M. Labiche, X. Pereira-Lopez, S. Afara, F. Ameil, T. Arici, S. Aydin, M. Axiotis, D. Barrientos, G. Benzoni, B. Birkenbach, A. Boston, H. Boston, P. Boutachkov, A. Bracco, A. Bruce, B. Bruyneel, B. Cederwall, E. Clement, M. Cortes, D. Cullen, P. Désesquelles, Z. Dombràdi, C. Domingo-Pardo, J. Eberth, C. Fahlander, M. Gelain, V. González, P. John, J. Gerl, P. Golubev, M. Górska, A. Gottardo, T. Grahn, L. Grassi, T. Habermann, L. Harkness-Brennan, T. Henry, H. Hess, I. Kojouharov, W. Korten, N. Lalović, M. Lettmann, C. Lizarazo, C. Louchart-Henning, R. Menegazzo, D. Mengoni, E. Merchan, C. Michelagnoli, B. Million, V. Modamio, T. Moeller, D. Napoli, J. Nyberg, B. Nara Singh, H. Pai, N. Pietralla, S. Pietri, Z. Podolyak, R. Perez Vidal, A. Pullia, D. Ralet, G. Rainovski, M. Reese, P. Reiter, M. Salsac, E. Sanchis, L. Sarmiento, H. Schaffner, L. Scruton, P. Singh, C. Stahl, S. Uthayakumaar, J. Valiente-Dobón and O. Wieland. *Physics Letters B*, **797**, 134835 (2019). ISSN 0370-2693. . URL https://www.sciencedirect.com/science/article/pii/S0370269319305490.

[15] C. Morse, H. Iwasaki, A. Lemasson, A. Dewald, T. Braunroth, V. Bader, T. Baugher, D. Bazin, J. Berryman, C. Campbell, A. Gade, C. Langer, I. Lee, C. Loelius, E. Lunderberg, F. Recchia, D. Smalley, S. Stroberg, R. Wadsworth, C. Walz, D. Weisshaar, A. Westerberg, K. Whitmore and K. Wimmer. *Physics Letters B*, **787**, 198 (2018). ISSN 0370-2693. . URL https://www.sciencedirect.com/science/article/pii/S037026931830844X.

[16] J. C. Hardy and I. S. Towner. *Phys. Rev. C*, **71**, 055501 (2005). . URL https://link.aps.org/doi/10.1103/PhysRevC.71.055501.

[17] H. Schatz, A. Aprahamian, J. Görres, M. Wiescher, T. Rauscher, J. Rembges, F.-K. Thielemann, B. Pfeiffer, P. Möller, K.-L. Kratz, H. Herndl, B. Brown and H. Rebel. *Physics Reports*, **294**, 167 (1998). ISSN 0370-1573. . URL https://www.sciencedirect.com/science/article/pii/S0370157397000483.

[18] J. B. Stoker, P. F. Mantica, D. Bazin, A. Becerril, J. S. Berryman, H. L. Crawford, A. Estrade, C. J. Guess, G. W. Hitt, G. Lorusso, M. Matos, K. Minamisono, F. Montes, J. Pereira, G. Perdikakis, H. Schatz, K. Smith and R. G. T. Zegers. *Phys. Rev. C*, **79**, 015803 (2009). . URL https://link.aps.org/doi/10.1103/PhysRevC.79.015803.

[19] K. Kaneko, T. Mizusaki, Y. Sun, S. Tazaki and G. de Angelis. *Phys. Rev. Lett.*, **109**, 092504 (2012). . URL https://link.aps.org/doi/10.1103/PhysRevLett.109.092504.

[20] W. Heisenberg. *Zeitschrift fur Physik*, **77**, 1 (1932). . URL https://doi.org/10.1007/BF01342433.

[21] E. Wigner. *Phys. Rev.*, **51**, 106 (1937). . URL https://link.aps.org/doi/10.1103/PhysRev.51.106.

[22] P. E. Garrett, W. E. Ormand, D. Appelbe, R. W. Bauer, J. A. Becker, L. A. Bernstein, J. A. Cameron, M. P. Carpenter, R. V. F. Janssens, C. J. Lister, D. Seweryniak, E. Tavukcu and D. D. Warner. *Phys. Rev. Lett.*, **87**, 132502 (2001). . URL https://link.aps.org/doi/10.1103/PhysRevLett.87.132502.

[23] S. M. Lenzi, N. Mărginean, D. R. Napoli, C. A. Ur, A. P. Zuker, G. de Angelis, A. Algora, M. Axiotis, D. Bazzacco, N. Belcari, M. A. Bentley, P. G. Bizzeti, A. Bizzeti-Sona, F. Brandolini, P. von Brentano, D. Bucurescu, J. A. Cameron, C. Chandler, M. De Poli, A. Dewald, H. Eberth, E. Farnea, A. Gadea, J. Garces-Narro, W. Gelletly, H. Grawe, R. Isocrate, D. T. Joss, C. A. Kalfas, T. Klug, T. Lampman, S. Lunardi, T. Martínez, G. Martínez-Pinedo, R. Menegazzo, J. Nyberg, Z. Podolyak, A. Poves, R. V. Ribas, C. Rossi Alvarez, B. Rubio, J. Sánchez-Solano, P. Spolaore, T. Steinhardt, O. Thelen, D. Tonev, A. Vitturi, W. von Oertzen and M. Weiszflog. *Phys. Rev. Lett.*, **87**, 122501 (2001). . URL https://link.aps.org/doi/10.1103/PhysRevLett.87.122501.

[24] D. E. González Trotter, F. Salinas, Q. Chen, A. S. Crowell, W. Glöckle, C. R. Howell, C. D. Roper, D. Schmidt, I. Šlaus, H. Tang, W. Tornow, R. L. Walter, H. Witała and Z. Zhou. *Phys. Rev. Lett.*, **83**, 3788 (1999). . URL https://link.aps.org/doi/10.1103/PhysRevLett.83.3788.

[25] C. Howell, Q. Chen, T. Carman, A. Hussein, W. Gibbs, B. Gibson, G. Mertens, C. Moore, C. Morris, A. Obst, E. Pasyuk, C. Roper, F. Salinas, I. Slaus, S. Sterbenz, W. Tornow, R. Walter, C. Whiteley and M. Whitton. *Physics Letters B*, **444**, 252 (1998). ISSN 0370-2693. . URL https://www.sciencedirect.com/science/article/pii/S0370269398013860.

[26] R. Machleidt and H. Müther. *Phys. Rev. C*, **63**, 034005 (2001). . URL https://link.aps.org/doi/10.1103/PhysRevC.63.034005.

[27] M. A. Bentley, S. M. Lenzi, S. A. Simpson and C. A. Diget. *Phys. Rev. C*, **92**, 024310 (2015). . URL https://link.aps.org/doi/10.1103/PhysRevC.92.024310.

[28] S. M. Lenzi, M. A. Bentley, R. Lau and C. A. Diget. *Phys. Rev. C*, **98**, 054322 (2018). . URL https://link.aps.org/doi/10.1103/PhysRevC.98.054322.

[29] K. Kaneko, Y. Sun and G. de Angelis. *Nucl. Phys. A*, **957**, 144 (2017). . URL https://www.sciencedirect.com/science/article/pii/S0375947416302147.

[30] J. A. Sheikh and R. Wyss. *Phys. Rev. C*, **62**, 051302 (2000). . URL https://link.aps.org/doi/10.1103/PhysRevC.62.051302.

[31] P. J. Davies, A. V. Afanasjev, R. Wadsworth, C. Andreoiu, R. A. E. Austin, M. P. Carpenter, D. Dashdorj, S. J. Freeman, P. E. Garrett, A. Görgen, J. Greene, D. G. Jenkins, F. L. Johnston-Theasby, P. Joshi, A. O. Macchiavelli, F. Moore, G. Mukherjee, W. Reviol, D. Sarantites, D. Seweryniak, M. B. Smith, C. E. Svensson, J. J. Valiente-Dobon and D. Ward. *Phys. Rev. C*, **75**, 011302 (2007). . URL https://link.aps.org/doi/10.1103/PhysRevC.75.011302.

[32] A. V. Afanasjev and S. Frauendorf. *Phys. Rev. C*, **71**, 064318 (2005). . URL https://link.aps.org/doi/10.1103/PhysRevC.71.064318.

[33] S. Frauendorf and A. Macchiavelli. *Progress in Particle and Nuclear Physics*, **78**, 24 (2014). ISSN 0146-6410. . URL https://www.sciencedirect.com/science/article/pii/S0146641014000465.

[34] A. O. Macchiavelli, P. Fallon, R. M. Clark, M. Cromaz, M. A. Deleplanque, R. M. Diamond, G. J. Lane, I. Y. Lee, F. S. Stephens, C. E. Svensson, K. Vetter and D. Ward. *Phys. Rev. C*, **61**, 041303 (2000). . URL https://link.aps.org/doi/10.1103/PhysRevC.61.041303.

[35] O. Haxel, J. H. D. Jensen and H. E. Suess. *Phys. Rev.*, **75**, 1766 (1949). . URL https://link.aps.org/doi/10.1103/PhysRev.75.1766.2.

[36] M. G. Mayer. *Phys. Rev.*, **78**, 16 (1950). . URL https://link.aps.org/doi/10.1103/PhysRev.78.16.

[37] J. Duflo and A. P. Zuker. *Phys. Rev. C*, **66**, 051304 (2002). . URL https://link.aps.org/doi/10.1103/PhysRevC.66.051304.

[38] O. B. Tarasov and D. Bazin. *Nuclear Instruments and Methods in Physics Research Section B: Beam Interactions with Materials and Atoms*, **204**, 174 (2003). ISSN 0168-583X. . URL https://www.sciencedirect.com/science/article/pii/S0168583X02019171. 14th International Conference on Electromagnetic Isotope Separators and Techniques Related to their Applications.

[39] J. Pakarinen, J. Ojala and P. R. *et al*. *Eur. Phys. J. A,*, **56**, 149 (2010). URL https://doi.org/10.1140/epja/s10050-020-00144-6.

[40] J. Eberth and J. Simpson. *Progress in Particle and Nuclear Physics*, **60**, 283 (2008). ISSN 0146-6410. . URL https://www.sciencedirect.com/science/article/pii/S0146641007000828.

[41] C. Beausang, S. Forbes, P. Fallon, P. Nolan, P. Twin, J. Mo, J. Lisle, M. Bentley, J. Simpson, F. Beck, D. Curien, G. deFrance, G. Duchêne and D. Popescu. *Nuclear Instruments and Methods in Physics Research Section A: Accelerators, Spectrometers, Detectors and Associated Equipment*, **313**, 37 (1992). ISSN 0168-9002. . URL https://www.sciencedirect.com/science/article/pii/016890029290084H.

[42] G. Duchêne, F. Beck, P. Twin, G. de France, D. Curien, L. Han, C. Beausang, M. Bentley, P. Nolan and J. Simpson. *Nuclear Instruments and Methods in Physics Research Section A: Accelerators, Spectrometers, Detectors and Associated Equipment*, **432**, 90 (1999). ISSN 0168-9002. . URL https://www.sciencedirect.com/science/article/pii/S0168900299002776.

[43] J. Sarén. *The ion-optical design of the MARA recoilseparator and absolute transmission measurements of the RITU gas-lled recoil separator*. Ph.D. thesis, Department of Physics, University of Jyväskylä (2011).

[44] L. Sottili. *Test of JYU-Tube as a veto detector for background suppression in nuclear spectroscopy beyond the proton drip line*. Master's thesis, Department of Physics, University of Jyväskylä (2018).

[45] J. Kemmer. *Nuclear Instruments and Methods*, **169**, 499 (1980). ISSN 0029-554X. . URL https://www.sciencedirect.com/science/article/pii/0029554X80909489.

[46] J. Kemmer. *Nuclear Instruments and Methods in Physics Research Section A: Accelerators, Spectrometers, Detectors and Associated Equipment*, **226**, 89 (1984). ISSN 0168-9002. . URL https://www.sciencedirect.com/science/article/pii/0168900284901736.

[47] http://www.micronsemiconductor.co.uk/product/bb20/.

[48] H. Joukainen, J. Sarén and P. Ruotsalainen. *Nuclear Instruments and Methods in Physics Research Section A: Accelerators, Spectrometers, Detectors and Associated Equipment*, **1027**, 166253 (2022). ISSN 0168-9002. . URL https://www.sciencedirect.com/science/article/pii/S0168900221010895.

[49] https://eljentechnology.com/products/plastic-scintillators/ej-244-ej-248-ej-244m-ej-248m.

[50] D. Barrientos, A. Boston, H. Boston, B. Quintana, I. Sagrado, C. Unsworth, S. Moon and J. Cresswell. *Nuclear Instruments and Methods in Physics Research Section A: Accelerators, Spectrometers, Detectors and Associated Equipment*, **648**, S228 (2011). ISSN 0168-9002. . URL https://www.sciencedirect.com/science/article/pii/S0168900210026768.

[51] https://mirion.s3.amazonaws.com/cms4_mirion/files/pdf/spec-sheets/ops-1424_bege_spec_sheet.pdf?1579456901.

[52] I. Lazarus, E. Appelbe, P. Butler, P. Coleman-Smith, J. Cresswell, S. Freeman, R. Herzberg, I. Hibbert, D. Joss, S. Letts, R. Page, V. Pucknell, P. Regan, J. Sampson, J. Simpson, J. Thornhill and R. Wadsworth. *IEEE Transactions on Nuclear Science*, **48**, 567 (2001). .

[53] A. Georgiev and W. Gast. *IEEE Transactions on Nuclear Science*, **40**, 770 (1993). .

[54] M. Lauer. *Digital Signal Processing for segmented HPGe Detectors Preprocessing Algorithms and Pulse Shape Analysis*. Ph.D. thesis, Natural Sciences and for Mathematics of the Ruperto-Carola University of Heidelberg (2004).

[55] P. Rahkila. *Nuclear Instruments and Methods in Physics Research Section A: Accelerators, Spectrometers, Detectors and Associated Equipment*, **595**, 637 (2008). ISSN 0168-9002. . URL https://www.sciencedirect.com/science/article/pii/S0168900208011698.

[56] *Aida project*. URL http://aida.freehep.org/.

[57] *Jaida project*. URL http://java.freehep.org/jaida.

[58] R. Brun and F. Rademakers. *Nuclear Instruments and Methods in Physics Research Section A*, **389**, 81 (1997). URL https://www.sciencedirect.com/science/article/pii/S016890029700048X?via%3Dihub.

[59] K. Krane, R. Steffen and R. Wheeler. *Atomic Data and Nuclear Data Tables*, **11**, 351 (1973). ISSN 0092-640X. . URL https://www.sciencedirect.com/science/article/pii/S0092640X73800166.

[60] T. Yamazaki. *Nuclear Data Sheets. Section A*, **3**, 1 (1967). ISSN 0550-306X. . URL https://www.sciencedirect.com/science/article/pii/S0550306X67800028.

[61] J. S. Lilley. *Nuclear Physics Principles and Applications*. John Wiley and Sons (1999).

[62] B. Hadinia, B. Cederwall, J. Blomqvist, E. Ganioğlu, P. T. Greenlees, K. Andgren, I. G. Darby, S. Eeckhaudt, E. Ideguchi, P. M. Jones, D. T. Joss, R. Julin, S. Juutinen, S. Ketelhut, K. Lagergren, A.-P. Leppänen, M. Leino, M. Nyman, J. Pakarinen, E. S. Paul, M. Petri, P. Rahkila, M. Sandzelius, J. Sarén, C. Scholey, J. Uusitalo, R. Wadsworth and R. Wyss. *Phys. Rev. C*, **72**, 041303 (2005). . URL https://link.aps.org/doi/10.1103/PhysRevC.72.041303.

[63] D. G. Jenkins, M. Muikku, P. T. Greenlees, K. Hauschild, K. Helariutta, P. M. Jones, R. Julin, S. Juutinen, H. Kankaanpää, N. S. Kelsall, H. Kettunen, P. Kuusiniemi, M. Leino, C. J. Moore, P. Nieminen, C. D. O'Leary, R. D. Page, P. Rakhila, W. Reviol, M. J. Taylor, J. Uusitalo and R. Wadsworth. *Phys. Rev. C*, **62**, 021302 (2000). . URL https://link.aps.org/doi/10.1103/PhysRevC.62.021302.

[64] P. M. Raddon, D. G. Jenkins, C. D. O'Leary, A. J. Simons, R. Wadsworth, A. N. Andreyev, R. D. Page, M. P. Carpenter, F. G. Kondev, T. Enqvist, P. T. Greenlees, P. M. Jones, R. Julin, S. Juutinen, H. Kettunen, M. Leino, A.-P. Leppänen, P. Nieminen, J. Pakarinen, P. Rahkila, J. Uusitalo and D. T. Joss. *Phys. Rev. C*, **70**, 064308 (2004). . URL https://link.aps.org/doi/10.1103/PhysRevC.70.064308.

[65] D. Wilkinson. *Nuclear Instruments and Methods in Physics Research Section A: Accelerators, Spectrometers, Detectors and Associated Equipment*, **543**, 497 (2005). ISSN 0168-9002. . URL https://www.sciencedirect.com/science/article/pii/S0168900204024295.

[66] A. Steer, D. Jenkins, R. Glover, B. Nara Singh, N. Pattabiraman, R. Wadsworth, S. Eeckhaudt, T. Grahn, P. Greenlees, P. Jones, R. Julin, S. Juutinen, M. Leino, M. Nyman, J. Pakarinen, P. Rahkila, J. Sarén, C. Scholey, J. Sorri, J. Uusitalo, P. Butler, I. Darby, R.-D. Herzberg, D. Joss, R. Page, J. Thomson, R. Lemmon, J. Simpson and B. Blank. *Nuclear Instruments and Methods in Physics Research Section A: Accelerators, Spectrometers, Detectors and Associated Equipment*, **565**, 630 (2006). ISSN 0168-9002. . URL https://www.sciencedirect.com/science/article/pii/S0168900206011442.

[67] K. Wimmer, P. Ruotsalainen, S. M. Lenzi, A. Povesh, T. Hüyük, F. Browne, P. Doornenbal, T. Koiwai, T. Arici, K. Auranen, M. Bentley, M. L. Cortés, C. Delafosse,

T. Eronen, Z. Ge, T. Grahn, P. T. Greenlees, A. Illana, N. Imai, H. Joukainen, R. Julin, A. Jungclaus, H. Jutila, A. Kankainen, N. Kitamura, M. Leino, B. Longfellow, J. Louko, R. Lozeva, M. Luoma, B. Mauss, D. Napoli, M. Niikura, J. Ojala, J. Pakarinen, X. Pereira-Lopez, P. Rahkila, F. Recchia, M. Sandzelius, J. Sarén, R. Taniuchi, H. Tann, S. Uthayakumaar, J. Uusitalo, V. Vaquero, R. Wadsworth, G. Zimba and R. Yajzey. *Isopsin symmetry in the T=1, A=62 triplet* (2022). Unpublished.

[68] *Evaluated Nuclear Structure Data File* (accessed: 18.12.2022). URL https://www.nndc.bnl.gov/ensdf/.

[69] F. Pühlhofer. *Nuclear Physics A*, **280**, 267 (1977). ISSN 0375-9474. . URL https://www.sciencedirect.com/science/article/pii/0375947477903086.

[70] W. Reisdorf. *Zeitschrift für Physik A Atoms and Nuclei*, **300**, 227 (1981). ISSN 0939-7922. . URL https://doi.org/10.1007/BF01412298.

[71] J.-J. Gaimard and K.-H. Schmidt. *Nuclear Physics A*, **531**, 709 (1991). ISSN 0375-9474. . URL https://www.sciencedirect.com/science/article/pii/037594749190748U.

[72] K. Hagino, N. Rowley and A. Kruppa. *Computer Physics Communications*, **123**, 143 (1999). ISSN 0010-4655. . URL https://www.sciencedirect.com/science/article/pii/S001046559900243X.

[73] B. Blank, G. Canchel, F. Seis and P. Delahaye. *Nuclear Instruments and Methods in Physics Research Section B: Beam Interactions with Materials and Atoms*, **416**, 41 (2018). ISSN 0168-583X. . URL https://www.sciencedirect.com/science/article/pii/S0168583X17310054.

[74] W. Gelletly, M. Bentley, H. Price, J. Simpson, C. Gross, J. Durell, B. Varley, O. Skeppstedt and S. Rastikerdar. *Physics Letters B*, **253**, 287 (1991). ISSN 0370-2693. . URL https://www.sciencedirect.com/science/article/pii/037026939191720G.

[75] D. Bucurescu, C. Rossi Alvarez, C. A. Ur, N. Mărginean, P. Spolaore, D. Bazzacco, S. Lunardi, D. R. Napoli, M. Ionescu-Bujor, A. Iordăchescu, C. M. Petrache, G. de Angelis, A. Gadea, D. Foltescu, F. Brandolini, G. Falconi, E. Farnea, S. M. Lenzi, N. H. Medina, Z. Podolyak, M. De Poli, M. N. Rao and R. Venturelli. *Phys. Rev. C*, **56**, 2497 (1997). . URL https://link.aps.org/doi/10.1103/PhysRevC.56.2497.

[76] N. Mărginean, D. Bucurescu, C. Rossi Alvarez, C. A. Ur, Y. Sun, D. Bazzacco, S. Lunardi, G. de Angelis, M. Axiotis, E. Farnea, A. Gadea, M. Ionescu-Bujor, A. Iordăchescu, W. Krolas, T. Kröll, S. M. Lenzi, T. Martinez, R. Menegazzo, D. R. Napoli, P. Pavan, Z. Podolyak, M. De Poli, B. Quintana and P. Spolaore. *Phys. Rev. C*, **65**, 051303 (2002). . URL https://link.aps.org/doi/10.1103/PhysRevC.65.051303.

[77] J. Sarén. private communication (07-12-2022).

[78] H. Morinaga. *Phys. Rev.*, **101**, 254 (1956). . URL https://link.aps.org/doi/10.1103/PhysRev.101.254.

[79] R. F. Casten, D. D. Warner, D. S. Brenner and R. L. Gill. *Phys. Rev. Lett.*, **47**, 1433 (1981). . URL https://link.aps.org/doi/10.1103/PhysRevLett.47.1433.

[80] L. Grodzins. *Physics Letters*, **2**, 88 (1962). ISSN 0031-9163. . URL https://www.sciencedirect.com/science/article/pii/0031916362901622.

[81] F. S. Stephens, R. M. Diamond, J. R. Leigh, T. Kammuri and K. Nakai. *Phys. Rev. Lett.*, **29**, 438 (1972). . URL https://link.aps.org/doi/10.1103/PhysRevLett.29.438.

[82] P. Möller, A. Sierk, T. Ichikawa and H. Sagawa. *Atomic Data and Nuclear Data Tables*, **109-110**, 1 (2016). ISSN 0092-640X. . URL https://www.sciencedirect.com/science/article/pii/S0092640X1600005X.

[83] A. Petrovici, K. Schmid and A. Faessler. *Nuclear Physics A*, **605**, 290 (1996). ISSN 0375-9474. . URL https://www.sciencedirect.com/science/article/pii/0375947496002242.

[84] C. J. Lister, P. J. Ennis, A. A. Chishti, B. J. Varley, W. Gelletly, H. G. Price and A. N. James. *Phys. Rev. C*, **42**, R1191 (1990). . URL https://link.aps.org/doi/10.1103/PhysRevC.42.R1191.

[85] C. J. Lister, M. Campbell, A. A. Chishti, W. Gelletly, L. Goettig, R. Moscrop, B. J. Varley, A. N. James, T. Morrison, H. G. Price, J. Simpson, K. Connel and O. Skeppstedt. *Phys. Rev. Lett.*, **59**, 1270 (1987). . URL https://link.aps.org/doi/10.1103/PhysRevLett.59.1270.

[86] G. J. Fu and C. W. Johnson. *Phys. Rev. C*, **104**, 024312 (2021). . URL https://link.aps.org/doi/10.1103/PhysRevC.104.024312.

[87] S. Thakur, P. Kumar, V. Thakur, V. Kumar and S. K. Dhiman. *Nuclear Physics A*, **1014**, 122254 (2021). ISSN 0375-9474. . URL https://www.sciencedirect.com/science/article/pii/S0375947421001196.

[88] F. Stephens and R. Simon. *Nuclear Physics A*, **183**, 257 (1972). ISSN 0375-9474. . URL https://www.sciencedirect.com/science/article/pii/0375947472906586.

[89] K. Kaneko and J.-y. Zhang. *Phys. Rev. C*, **57**, 1732 (1998). . URL https://link.aps.org/doi/10.1103/PhysRevC.57.1732.

[90] S. M. Fischer, C. J. Lister, D. P. Balamuth, R. Bauer, J. A. Becker, L. A. Bernstein, M. P. Carpenter, J. Durell, N. Fotiades, S. J. Freeman, P. E. Garrett, P. A. Hausladen, R. V. F. Janssens, D. Jenkins, M. Leddy, J. Ressler, J. Schwartz, D. Svelnys, D. G. Sarantites, D. Seweryniak, B. J. Varley and R. Wyss. *Phys. Rev. Lett.*, **87**, 132501 (2001). . URL https://link.aps.org/doi/10.1103/PhysRevLett.87.132501.

[91] S. Frauendorf and J. A. Sheikh. *Phys. Rev. C*, **59**, 1400 (1999). . URL https://link.aps.org/doi/10.1103/PhysRevC.59.1400.

[92] C. Borcan, H. Schnare, R. Schwengner, L. Käubler, H. G. Ortlepp, F. Dönau, H. Grawe, M. Górska, S. Skoda, J. Eberth, T. Härtlein, F. Köck, D. Pansegrau, M. Moszyński, D. Wolski, M. Weiszflog, A. Axelsson, D. R. Napoli, A. Gadea, R. Wadsworth, A. Wilson and W. Andrejtscheff. *Eur. Phys. J. A.*, **5**, 243 (1999). . URL https://link.springer.com/article/10.1007/s100500050281.

[93] G. Pausch, W. Bohne, D. Hilscher, H.-G. Ortlepp and D. Polster. *Nuclear Instruments and Methods in Physics Research Section A: Accelerators, Spectrometers, Detectors and Associated Equipment*, **349**, 281 (1994). ISSN 0168-9002. . URL https://www.sciencedirect.com/science/article/pii/0168900294906343.

[94] Skeppstedt, H. Roth, L. Lindström, R. Wadsworth, I. Hibbert, N. Kelsall, D. Jenkins, H. Grawe, M. Górska, M. Moszyński, Z. Sujkowski, D. Wolski, M. Kapusta, M. Hellström, S. Kalogeropoulos, D. Oner, A. Johnson, J. Cederkäll, W. Klamra, J. Nyberg, M. Weiszflog, J. Kay, R. Griffiths, J. Garces Narro, C. Pearson and J. Eberth. *Nuclear Instruments and Methods in Physics Research Section A: Accelerators, Spectrometers, Detectors and Associated Equipment*, **421**, 531 (1999). ISSN 0168-9002. . URL https://www.sciencedirect.com/science/article/pii/S016890029801208X.

[95] G. de Angelis, T. Martinez, A. Gadea, N. Marginean, E. Farnea, E. Maglione, S. Lenzi, W. Gelletly, C. A. Ur, D. R. Napoli, T. Kroell, S. Lunardi, B. Rubio, M. Axiotis, D. Bazzacco, A. M. B. Sona, P. G. Bizzeti, P. Bednarczyk, A. Bracco, F. Brandolini, F. Camera, D. Curien, M. D. Poli, O. Dorvaux, J. Eberth, H. Grawe, R. Menegazzo, G. Nardelli, J. Nyberg, P. Pavan, B. Quintana, C. R. Alvarez, P. Spolaore, T. Steinhart, I. Stefanescu, O. Thelen and R. Venturelli. *Eur. Phys. J. A.*, **12**, 51 (2001). . URL https://doi.org/10.1007/s100500170038.

[96] A. Gadea, E. Farnea, G. de Angelis, R. I. crate, A. Buscemi, P. Pavan, A. Algora, N. Marginean, T. Martinez, D. N. oli, M. D. Poli, P. S. olaore, D. Bazzacco, F. Brandolini, S. Lenzi, S. Lunardi, R. Menegazzo, C. R. Alvarez, P. Bizzeti, A. Bizzeti-Sona and the EUROBALL IV collaboration. *LNL Annual Report, 151-152*. https://www1.lnl.infn.it/~annrep/read_ar/1999/index_1999.html (1999).

[97] D. G. Jenkins, N. S. Kelsall, C. J. Lister, D. P. Balamuth, M. P. Carpenter, T. A. Sienko, S. M. Fischer, R. M. Clark, P. Fallon, A. Görgen, A. O. Macchiavelli, C. E. Svensson, R. Wadsworth, W. Reviol, D. G. Sarantites, G. C. Ball, J. Rikovska Stone, O. Juillet, P. Van Isacker, A. V. Afanasjev and S. Frauendorf. *Phys. Rev. C*, **65**, 064307 (2002). . URL https://link.aps.org/doi/10.1103/PhysRevC.65.064307.

[98] S. M. Lenzi, D. R. Napoli, C. A. Ur, D. Bazzacco, F. Brandolini, J. A. Cameron, E. Caurier, G. de Angelis, M. De Poli, E. Farnea, A. Gadea, S. Hankonen, S. Lunardi, G. Martínez-Pinedo, Z. Podolyak, A. Poves, C. Rossi Alvarez, J. Sánchez-Solano and H. Somacal. *Phys. Rev. C*, **60**, 021303 (1999). . URL https://link.aps.org/doi/10.1103/PhysRevC.60.021303.

[99] A. F. Lisetskiy, C. Frießer, A. Schmidt, I. Schneider, N. Pietralla, P. von Brentano, R. V. Jolos, T. Otsuka, T. Sebe and Y. Utsuno. *Physics of Atomic Nuclei*, **64**, 1206 (2001). . URL https://doi.org/10.1134/1.1389543.

[100] R. E. Mihai, A. S. Mare, N. Mărginean, A. Petrovici, O. Andrei, M. Boromiza, D. Bucurescu, G. C ăta Danil, C. Clisu, C. Costache, I. Dinescu, D. Filipescu, N. Florea, I. Gheorghe, A. Ionescu, R. Lică, R. Mărginean, C. Mihai, A. Mitu, A. Negret, C. R. Niță, A. Olăcel, A. Oprea, S. Pascu, A. Şerban, C. Sotty, L. Stan, R. Şuvăilă, S. Toma, A. Turturică, S. Ujeniuc and C. A. Ur. *Phys. Rev. C*, **106**, 024332 (2022). . URL https://link.aps.org/doi/10.1103/PhysRevC.106.024332.

[101] I. Ragnarsson and P. B. Semmes. *Hyperfine Interactions*, **43**, 423 (1988). . URL https://doi.org/10.1007/BF02398323.

[102] D. Giovanni. private communication (19-12-2022).

[103] S. Bonger, T. Kuo and L. Coraggio. *Nuclear Physics A*, **684**, 432 (2001). ISSN 0375-9474. . URL https://www.sciencedirect.com/science/article/pii/ S0375947401004493. Few-Body Problems in Physics.

[104] M. Rocchini, K. Hadyńska-Klęk, A. Nannini, A. Goasduff, M. Zielińska, D. Testov, T. R. Rodríguez, A. Gargano, F. Nowacki, G. De Gregorio, H. Naïdja, P. Sona, J. J. Valiente-Dobón, D. Mengoni, P. R. John, D. Bazzacco, G. Benzoni, A. Boso, P. Cocconi, M. Chiari, D. T. Doherty, F. Galtarossa, G. Jaworski, M. Komorowska, N. Marchini, M. Matejska-Minda, B. Melon, R. Menegazzo, P. J. Napiorkowski, D. Napoli, M. Ottanelli, A. Perego, L. Ramina, M. Rampazzo, F. Recchia, S. Riccetto, D. Rosso and M. Siciliano. *Phys. Rev. C*, **103**, 014311 (2021). . URL https://link.aps.org/doi/10.1103/PhysRevC.103.014311.

[105] L. Coraggio, L. De Angelis, T. Fukui, A. Gargano, N. Itaco and F. Nowacki. *Phys. Rev. C*, **100**, 014316 (2019). . URL https://link.aps.org/doi/10.1103/PhysRevC.100. 014316.

[106] K. Suzuki and R. Okamoto. *Progress of Theoretical Physics*, **93**, 905 (1995). ISSN 0033-068X. . URL https://doi.org/10.1143/ptp/93.5.905.

[107] L. Coraggio, A. Covello, A. Gargano, N. Itaco and T. Kuo. *Annals of Physics*, **327**, 2125 (2012). ISSN 0003-4916. . URL https://www.sciencedirect.com/science/ article/pii/S0003491612000681.

[108] K. Starosta, A. Dewald, A. Dunomes, P. Adrich, A. M. Amthor, T. Baumann, D. Bazin, M. Bowen, B. A. Brown, A. Chester, A. Gade, D. Galaviz, T. Glasmacher, T. Ginter, M. Hausmann, M. Horoi, J. Jolie, B. Melon, D. Miller, V. Moeller, R. P. Norris, T. Pissulla, M. Portillo, W. Rother, Y. Shimbara, A. Stolz, C. Vaman, P. Voss, D. Weisshaar and V. Zelevinsky. *Phys. Rev. Lett.*, **99**, 042503 (2007). . URL https://link.aps.org/doi/10.1103/PhysRevLett.99.042503.

[109] A. Obertelli, T. Baugher, D. Bazin, J. P. Delaroche, F. Flavigny, A. Gade, M. Girod, T. Glasmacher, A. Goergen, G. F. Grinyer, W. Korten, J. Ljungvall, S. McDaniel, A. Ratkiewicz, B. Sulignano and D. Weisshaar. *Phys. Rev. C*, **80**, 031304 (2009). . URL https://link.aps.org/doi/10.1103/PhysRevC.80.031304.

[110] A. Gade, D. Bazin, A. Becerril, C. M. Campbell, J. M. Cook, D. J. Dean, D.-C. Dinca, T. Glasmacher, G. W. Hitt, M. E. Howard, W. F. Mueller, H. Olliver, J. R. Terry and K. Yoneda. *Phys. Rev. Lett.*, **95**, 022502 (2005). . URL https://link.aps.org/doi/10.1103/PhysRevLett.95.022502.

[111] A. Lemasson, H. Iwasaki, C. Morse, D. Bazin, T. Baugher, J. S. Berryman, A. Dewald, C. Fransen, A. Gade, S. McDaniel, A. Nichols, A. Ratkiewicz, S. Stroberg, P. Voss, R. Wadsworth, D. Weisshaar, K. Wimmer and R. Winkler. *Phys. Rev. C*, **85**, 041303 (2012). . URL https://link.aps.org/doi/10.1103/PhysRevC.85.041303.

[112] J. Ljungvall, A. Görgen, M. Girod, J.-P. Delaroche, A. Dewald, C. Dossat, E. Farnea, W. Korten, B. Melon, R. Menegazzo, A. Obertelli, R. Orlandi, P. Petkov, T. Pissulla, S. Siem, R. P. Singh, J. Srebrny, C. Theisen, C. A. Ur, J. J. Valiente-Dobón, K. O. Zell and M. Zielińska. *Phys. Rev. Lett.*, **100**, 102502 (2008). . URL https://link.aps.org/doi/10.1103/PhysRevLett.100.102502.

[113] A. M. Hurst, P. A. Butler, D. G. Jenkins, P. Delahaye, F. Wenander, F. Ames, C. J. Barton, T. Behrens, A. Bürger, J. Cederkäll, E. Clément, T. Czosnyka, T. Davinson, G. de Angelis, J. Eberth, A. Ekström, S. Franchoo, G. Georgiev, A. Görgen, R.-D. Herzberg, M. Huyse, O. Ivanov, J. Iwanicki, G. D. Jones, P. Kent, U. Köster, T. Kröll, R. Krücken, A. C. Larsen, M. Nespolo, M. Pantea, E. S. Paul, M. Petri, H. Scheit, T. Sieber, S. Siem, J. F. Smith, A. Steer, I. Stefanescu, N. U. H. Syed, J. Van de Walle, P. Van Duppen, R. Wadsworth, N. Warr, D. Weisshaar and M. Zielińska. *Phys. Rev. Lett.*, **98**, 072501 (2007). . URL https://link.aps.org/doi/10.1103/PhysRevLett.98.072501.

[114] J. Heese, K. P. Lieb, L. Lühmann, F. Raether, B. Wörmann, D. Alber, H. Grawe, J. Eberth and T. Mylaeus. *Z Phys A*, **325**, 45 (1986). . URL https://doi.org/10.1007/BF01294241.

[115] A. Petrovici. *Phys. Rev. C*, **91**, 014302 (2015). . URL https://link.aps.org/doi/10.1103/PhysRevC.91.014302.

[116] M. Leino, J. Äystö, T. Enqvist, P. Heikkinen, A. Jokinen, M. Nurmia, A. Ostrowski, W. Trzaska, J. Uusitalo, K. Eskola, P. Armbruster and V. Ninov. *Nuclear Instruments and Methods in Physics Research Section B: Beam Interactions with Materials and Atoms*, **99**, 653 (1995). ISSN 0168-583X. . URL https://www.sciencedirect.com/science/article/pii/0168583X94005737. Application of Accelerators in Research and Industry '94.

[117] A. Vitéz-Sveiczer, A. Algora, A. Morales, B. Rubio, G. Kiss, P. Sarriguren, P. Van Isacker, G. de Angelis, F. Recchia, S. Nishimura, J. Agramunt, V. Guadilla, A. Montaner-Pizá, S. Orrigo, A. Horváth, D. Napoli, S. Lenzi, A. Boso, V. Phong, J. Wu, P.-A. Söderström, T. Sumikama, H. Suzuki, H. Takeda, D. Ahn, H. Baba, P. Doornebal, N. Fukuda, N. Inabe, T. Isobe, T. Kubo, S. Kubono, H. Sakurai, Y. Shimizu, C. Sidong, B. Blank, P. Ascher, M. Gerbaux, T. Goigoux, J. Giovinazzo, S. Grévy, T. Kurtukián Nieto, C. Magron, W. Gelletly, Z. Dombrádi, Y. Fujita,

M. Tanaka, P. Aguilera, F. Molina, J. Eberth, F. Diel, D. Lubos, C. Borcea, E. Ganioglu, D. Nishimura, H. Oikawa, Y. Takei, S. Yagi, W. Korten, G. de France, P. Davies, J. Liu, J. Lee, T. Lokotko, I. Kojouharov, N. Kurz, H. Shaffner and A. Petrovici. *Physics Letters B*, **830**, 137123 (2022). ISSN 0370-2693. . URL https://www.sciencedirect.com/science/article/pii/S037026932200257X.

[118] A. I. Morales, A. Algora, B. Rubio, K. Kaneko, S. Nishimura, P. Aguilera, S. E. A. Orrigo, F. Molina, G. de Angelis, F. Recchia, G. Kiss, V. H. Phong, J. Wu, D. Nishimura, H. Oikawa, T. Goigoux, J. Giovinazzo, P. Ascher, J. Agramunt, D. S. Ahn, H. Baba, B. Blank, C. Borcea, A. Boso, P. Davies, F. Diel, Z. Dombrádi, P. Doornenbal, J. Eberth, G. de France, Y. Fujita, N. Fukuda, E. Ganioglu, W. Gelletly, M. Gerbaux, S. Grévy, V. Guadilla, N. Inabe, T. Isobe, I. Kojouharov, W. Korten, T. Kubo, S. Kubono, T. Kurtukián Nieto, N. Kurz, J. Lee, S. Lenzi, J. Liu, T. Lokotko, D. Lubos, C. Magron, A. Montaner-Pizá, D. R. Napoli, H. Sakurai, H. Schaffner, Y. Shimizu, C. Sidong, P.-A. Söderström, T. Sumikama, H. Suzuki, H. Takeda, Y. Takei, M. Tanaka and S. Yagi. *Phys. Rev. C*, **95**, 064327 (2017). . URL https://link.aps.org/doi/10.1103/PhysRevC.95.064327.

[119] K. Kaneko, Y. Sun, T. Mizusaki and S. Tazaki. *Phys. Rev. C*, **89**, 031302 (2014). . URL https://link.aps.org/doi/10.1103/PhysRevC.89.031302.

[120] T. Mizusaki, K. Kaneko, M. Honma and T. Sakurai. *Phys. Rev. C*, **82**, 024310 (2010). . URL https://link.aps.org/doi/10.1103/PhysRevC.82.024310.

[121] M. Honma, T. Otsuka, T. Mizusaki and M. Hjorth-Jensen. *Phys. Rev. C*, **80**, 064323 (2009). . URL https://link.aps.org/doi/10.1103/PhysRevC.80.064323.

[122] C. Longour, J. Garcés Narro, B. Blank, M. Lewitowicz, C. Miehé, P. H. Regan, D. Applebe, L. Axelsson, A. M. Bruce, W. N. Catford, C. Chandler, R. M. Clark, D. M. Cullen, S. Czajkowski, J. M. Daugas, P. Dessagne, A. Fleury, L. Frankland, W. Gelletly, J. Giovinazzo, B. Greenhalgh, R. Grzywacz, M. Harder, K. L. Jones, N. Kelsall, T. Kszczot, R. D. Page, C. J. Pearson, A. T. Reed, O. Sorlin and R. Wadsworth. *Phys. Rev. Lett.*, **81**, 3337 (1998). . URL https://link.aps.org/doi/10.1103/PhysRevLett.81.3337.

[123] R. Page, A. Andreyev, D. Appelbe, P. Butler, S. Freeman, P. Greenlees, R.-D. Herzberg, D. Jenkins, G. Jones, P. Jones, D. Joss, R. Julin, H. Kettunen, M. Leino, P. Rahkila, P. Regan, J. Simpson, J. Uusitalo, S. Vincent and R. Wadsworth. *Nuclear Instruments and Methods in Physics Research Section B: Beam Interactions with Materials and Atoms*, **204**, 634 (2003). ISSN 0168-583X. . URL https://www.sciencedirect.com/science/article/pii/S0168583X02021432. 14th International Conference on Electromagnetic Isotope Separators and Techniques Related to their Applications.

[124] A. Andreyev, P. Butler, R. Page, D. Appelbe, G. Jones, D. Joss, R.-D. Herzberg, P. Regan, J. Simpson and R. Wadsworth. *Nuclear Instruments and Methods in Physics Research Section A: Accelerators, Spectrometers, Detectors and Associated*

Equipment, **533**, 422 (2004). ISSN 0168-9002. . URL https://www.sciencedirect.com/science/article/pii/S0168900204017462.

[125] K. Kaneko, Y. Sun, T. Mizusaki and S. Tazaki. *Phys. Rev. Lett.*, **110**, 172505 (2013). . URL https://link.aps.org/doi/10.1103/PhysRevLett.110.172505.

[126] G. de Angelis, K. T. Wiedemann, T. Martinez, R. Orlandi, A. Petrovici, E. Sahin, J. J. Valiente-Dobón, D. Tonev, S. Lunardi, B. S. Nara Singh, R. Wadsworth, A. Gadea, K. Kaneko, P. G. Bizzeti, A. M. Bizzeti-Sona, B. Blank, A. Bracco, M. P. Carpenter, C. J. Chiara, E. Farnea, A. Gottardo, J. P. Greene, S. M. Lenzi, S. Leoni, C. J. Lister, D. Mengoni, D. R. Napoli, O. L. Pechenaya, F. Recchia, W. Reviol, D. G. Sarantites, D. Seweryniak, C. A. Ur and S. Zhu. *Phys. Rev. C*, **85**, 034320 (2012). . URL https://link.aps.org/doi/10.1103/PhysRevC.85.034320.

[127] R. D. O. Llewellyn. *Structure and Collectivity of Highly Deformed Nuclei Along the N=Z Line*. Ph.D. thesis, Department of Physics, University of York (2020).

[128] D. Bazin, J. Caggiano, B. Sherrill, J. Yurkon and A. Zeller. *Nuclear Instruments and Methods in Physics Research Section B: Beam Interactions with Materials and Atoms*, **204**, 629 (2003). ISSN 0168-583X. . URL https://www.sciencedirect.com/science/article/pii/S0168583X02021420. 14th International Conference on Electromagnetic Isotope Separators and Techniques Related to their Applications.

[129] D. Weisshaar, D. Bazin, P. Bender, C. Campbell, F. Recchia, V. Bader, T. Baugher, J. Belarge, M. Carpenter, H. Crawford, M. Cromaz, B. Elman, P. Fallon, A. Forney, A. Gade, J. Harker, N. Kobayashi, C. Langer, T. Lauritsen, I. Lee, A. Lemasson, B. Longfellow, E. Lunderberg, A. Macchiavelli, K. Miki, S. Momiyama, S. Noji, D. Radford, M. Scott, J. Sethi, S. Stroberg, C. Sullivan, R. Titus, A. Wiens, S. Williams, K. Wimmer and S. Zhu. *Nuclear Instruments and Methods in Physics Research Section A: Accelerators, Spectrometers, Detectors and Associated Equipment*, **847**, 187 (2017). ISSN 0168-9002. . URL https://www.sciencedirect.com/science/article/pii/S0168900216312402.

[130] J. Uusitalo, D. Seweryniak, P. F. Mantica, J. Rikovska, D. S. Brenner, M. Huhta, J. Greene, J. J. Ressler, B. Tomlin, C. N. Davids, C. J. Lister and W. B. Walters. *Phys. Rev. C*, **57**, 2259 (1998). . URL https://link.aps.org/doi/10.1103/PhysRevC.57.2259.

[131] G. C. Ball, S. Bishop, J. A. Behr, G. C. Boisvert, P. Bricault, J. Cerny, J. M. D'Auria, M. Dombsky, J. C. Hardy, V. Iacob, J. R. Leslie, T. Lindner, J. A. Macdonald, H.-B. Mak, D. M. Moltz, J. Powell, G. Savard and I. S. Towner. *Phys. Rev. Lett.*, **86**, 1454 (2001). . URL https://link.aps.org/doi/10.1103/PhysRevLett.86.1454.

[132] A. Piechaczek, E. F. Zganjar, G. C. Ball, P. Bricault, J. M. D'Auria, J. C. Hardy, D. F. Hodgson, V. Iacob, P. Klages, W. D. Kulp, J. R. Leslie, M. Lipoglavsek, J. A. Macdonald, H.-B. Mak, D. M. Moltz, G. Savard, J. von Schwarzenberg, C. E. Svensson, I. S. Towner and J. L. Wood. *Phys. Rev. C*, **67**, 051305 (2003). . URL https://link.aps.org/doi/10.1103/PhysRevC.67.051305.

116

[133] S. M. Fischer, C. J. Lister, N. J. Hammond, R. V. F. Janssens, T. L. Khoo, T. Laurit-sen, E. F. Moore, D. Seweryniak, S. Sinha, D. P. Balamuth, P. A. Hausladen, D. G. Sarantites, W. Reviol, P. Chowdhury, S. D. Paul, C. Baktash and C.-H. Yu. *Phys. Rev. C*, **74**, 054304 (2006). . URL https://link.aps.org/doi/10.1103/PhysRevC.74.054304.

[134] F. Johnston-Theasby, A. V. Afanasjev, C. Andreoiu, R. A. E. Austin, M. P. Carpenter, D. Dashdorj, S. J. Freeman, P. E. Garrett, J. Greene, A. Görgen, D. G. Jenkins, P. Joshi, A. O. Macchiavelli, F. Moore, G. Mukherjee, W. Reviol, D. Sarantites, D. Seweryniak, M. B. Smith, C. E. Svensson, J. J. Valiente-Dobón, R. Wadsworth and D. Ward. *Phys. Rev. C*, **78**, 034312 (2008). . URL https://link.aps.org/doi/10.1103/PhysRevC.78.034312.

[135] C. O'Leary, M. Bentley, S. Lenzi, G. Martınez-Pinedo, D. Warner, A. Bruce, J. Cameron, M. Carpenter, C. Davids, P. Fallon, L. Frankland, W. Gelletly, R. Janssens, D. Joss, C. Lister, P. Regan, P. Reiter, B. Rubio, D. Seweryniak, C. Svensson, S. Vincent and S. Williams. *Physics Letters B*, **525**, 49 (2002). ISSN 0370-2693. . URL https://www.sciencedirect.com/science/article/pii/S0370269301014265.

[136] P. E. Garrett, S. M. Lenzi, E. Algin, D. Appelbe, R. W. Bauer, J. A. Becker, L. A. Bernstein, J. A. Cameron, M. P. Carpenter, R. V. F. Janssens, C. J. Lister, D. Seweryniak and D. D. Warner. *Phys. Rev. C*, **75**, 014307 (2007). . URL https://link.aps.org/doi/10.1103/PhysRevC.75.014307.

[137] A. Gadea, S. M. Lenzi, S. Lunardi, N. Mărginean, A. P. Zuker, G. de Angelis, M. Axiotis, T. Martínez, D. R. Napoli, E. Farnea, R. Menegazzo, P. Pavan, C. A. Ur, D. Bazzacco, R. Venturelli, P. Kleinheinz, P. Bednarczyk, D. Curien, O. Dorvaux, J. Nyberg, H. Grawe, M. Górska, M. Palacz, K. Lagergren, L. Milechina, J. Ek-man, D. Rudolph, C. Andreoiu, M. A. Bentley, W. Gelletly, B. Rubio, A. Algora, E. Nacher, L. Caballero, M. Trotta and M. Moszyński. *Phys. Rev. Lett.*, **97**, 152501 (2006). . URL https://link.aps.org/doi/10.1103/PhysRevLett.97.152501.

[138] J. Ekman, C. Fahlander and D. Rudolph. *Modern Physics Letters A*, **20**, 2977 (2005). . URL https://doi.org/10.1142/S0217732305019018.

[139] K. Kaneko, S. Tazaki, T. Mizusaki, Y. Sun, M. Hasegawa and G. de Angelis. *Phys. Rev. C*, **82**, 061301 (2010). . URL https://link.aps.org/doi/10.1103/PhysRevC.82.061301.

[140] D. Rudolph, C. Baktash, C. J. Gross, W. Satula, R. Wyss, I. Birriel, M. Devlin, H.-Q. Jin, D. R. LaFosse, F. Lerma, J. X. Saladin, D. G. Sarantites, G. N. Sylvan, S. L. Tabor, D. F. Winchell, V. Q. Wood and C. H. Yu. *Phys. Rev. C*, **56**, 98 (1997). . URL https://link.aps.org/doi/10.1103/PhysRevC.56.98.

[141] A. Harder, A. Jungclaus, M. K. Kabadiyski, D. Kast, K. P. Lieb, D. Rudolph, M. Weiszflog, T. D. Johnson, G. Winter, C. J. Gross, R. A. Cunningham, W. Gelletly, J. Simpson, D. D. Warner, I. G. Bearden, T. Shizuma, G. Sletten, D. Foltescu, H. A. Roth, O. Skeppstedt and B. J. Varley. *Phys. Rev. C*, **55**, 1680 (1997). . URL https://link.aps.org/doi/10.1103/PhysRevC.55.1680.